

Limit state of a concrete sliding hinge connection
A large scale test project

Master Thesis



Limit state of a concrete sliding hinge connection

A large scale test project

by

Bas Boon

in partial fulfilment of the requirements for the degree of

Master of Science

in Civil Engineering

at the Delft University of Technology,

to be defended publicly on 18th December 2020, at 15:30

Copyright: Reproduction of this publication in whole or in part must include the customary bibliographic citation, including author attribution, report title, etc.

Cover photo: Bas Boon, 2020

Published by: Technische Universiteit Delft, Concrete structures, Delft, Building 23,
2628 CN, Stevinweg 1 The Netherlands
[www.tudelft.nl/en/ceg/about-faculty/departments/engineering-structures/
sections-labs/concrete-structures/](http://www.tudelft.nl/en/ceg/about-faculty/departments/engineering-structures/sections-labs/concrete-structures/)

Preface

This thesis has been prepared at the Section for Concrete Structures, Department of Civil Engineering, at the Delft University of Technology, in partial fulfilment for the degree Master of Science in Engineering, MSc Eng. It is assumed that the reader has a basic knowledge in the areas of mechanics and concrete structures.

I did not have any prior experience with concrete hinges. Therefore, when Willem Nobel introduced me to this topic, it caught my interest right away. The implementation of this connection in sub-surface construction requires a thorough research. A full scale test project was already setup between Witteveen + Bos and the Stevin laboratory before I joined the project. I value my time in the lab where I spend a lot of my time. I want to say thanks to the lab technicians Albert Bosman and Jakub Pawlovicz for their support and their tremendous effort in completing the tests.

The support of all members of the committee is greatly appreciated. Yuguang Yang helped shape the research by pointing out areas of interest where his guidance was very helpful. The extensive contact with Willem Nobel was of great importance to keep the test project running as smooth as possible. The expertise of Max Hendriks and Kumar Anupam was very useful when problems or questions about specialised topics arose. Additionally, I want to thank my parents and friends for their continuous support and their efforts.

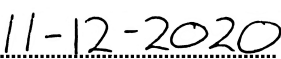
Bas Boon

Barneveld, December 2020

Supervisor:	Dr. ir. Y. Yang	TU Delft
Thesis committee:	Ir. W.L. Nobel	Witteveen + Bos
	Dr. K. Anupam	TU Delft
	Dr. ir. M.A.N. Hendriks	TU Delft

Bas Boon - 4745752


Signature


Date

Abstract

The suitability of a concrete sliding hinge connection in modern reinforced concrete structures has not been investigated yet. Cylindrical concrete sliding hinges were used most recently in the 19th century in arched structures. This type of connection is known for its large normal force capacity and a rotation limit only based on the geometry of the connection. For the case of underground constructions, large normal forces are often present at the wall-to-floor connections. Considering the risk of uneven settlements, such connections may also demand sufficient rotation capacity. Several challenges need to be addressed and solved before successfully implementing a concrete sliding hinge connection. Firstly, it is not clear how to design this type of hinge properly. Secondly, an appropriate sliding interface material needs to be identified. Furthermore, the influence of imperfections and friction at the interface needs to be clarified. Therefore, this research is initiated to solve these challenges. The outcome would aid in identifying what determines the limit state of a concrete sliding hinge connection. A test program is carried out to support the research, where full scale experiments are performed at the Stevin II laboratory of the Delft University of Technology. The goal is to prove the functioning of this type of hinged connection in a system before it is implemented in practice.

The contact mechanics of a cylindrical sliding connection is the basis of understanding the mechanism behind the internal contact behaviour. Different analytical contact models are investigated and implemented aiding in quantifying the performance of the connection. A finite element model is used to verify the analytical models and to obtain the stress distribution in the connection. This can only be achieved when an appropriate contact interface is modelled, displaying accurate contact behaviour. Two different bearing types are investigated in its ability to aid the sliding in the connection: a bituminous and a PTFE-stainless steel interface. Full scale concrete hinges are constructed to test the performance of the interface types. A floor element with a width of 500 mm is connected at each end to a cylindrical concrete hinge with a radius of 400 mm, constructed for testing according to an existing design. 6 sets of these test specimens are available where 4 of them are applied with a bituminous interface and 2 with a PTFE-stainless steel interface. The friction coefficients of the considered interface types are derived from the test results with the use of the analytical model. This research is aimed at deriving the limit state of the connection and the surrounding concrete structure. The governing failure modes are identified by the experiments and are supported by a finite element analysis. Critical connection details are derived based on the performance of the connection during testing and the underlying contact mechanics.

Available research about concrete sliding hinges is evaluated and analysed. Several tests have been performed on this type of concrete hinge in the early 20th century. The interface material of choice in those days was lead. Advancements in mainly material science made more suitable and favourable materials available. General interface requirements are investigated to achieve an optimal sliding interface. The contact stresses for two cylindrical bodies can be described by the Hertzian theory in a convenient manner. However, correct stresses cannot be achieved for conforming contact, meaning no interface clearance. The more extended Persson contact stress expression is able to cope with conforming contact as well as interface clearance. A more convenient analytical expression for the stresses can be achieved by calculating the contact area of the contact problem according to the Persson theory and implementing this in the Hertzian formulation. A discrete interface, behaving according to a Coulomb friction model, has shown to be capable of displaying the sliding hinge behaviour. Implementing this into a finite element model attributes to achieving a model showing realistic contact behaviour with the possibility to

quantify the effects of changes in the design and interface properties. A finite element analysis is performed on models increasing in complexity. Simplified models are used to obtain contact stress distributions supporting a mechanical model. The full test setup is modelled to help explain the test results and further load the connection to failure.

From the testing project it is found that the capacity of the cylindrical hinge for the given reinforcement design is significant when loaded in the normal direction. The concave concrete element can fail in a splitting failure mode when loaded to the normal force limit. The bituminous interface shows the ability to spread contact stresses and allow for reduced cracking under large normal force loads. Large loads in shear, in combination with low levels of normal force is a point of attention to prevent shear cracks, irrespective of the type of bearing. It is found that the hinge functions fine with favourable frictional behaviour for large shear forces indicating the ability to cope with these forces when a sufficient reinforcement design is implemented. Both the PTFE-stainless steel and the bituminous interface are found to have good properties to allow for sliding with low rotational resistance. The bearing materials showed friction coefficients below 0.1. The bending moment present in the connection, loaded with a certain contact force and substantial rotation, is derived based on the analytical model. The bending moment is found to depend on the contact force, the friction coefficient and the hinge radius. Significant low bending moments are obtained during testing compared to a conventional monolithic connection. The concave connection part determines the bending moment capacity due to the limited construction height, equal to the diameter of the cylindrical connection.

Contents

Preface	ii
Abstract	iii
1 Introduction	1
1.1 Scope	2
1.2 Research questions	2
1.3 Research approach and strategy	2
2 Literature review	5
2.1 Concrete hinges	5
2.2 Sliding interface materials	10
2.3 Contact mechanics	15
2.4 Discrete non-linear interfaces in finite element models	25
2.5 Summary of literature	29
3 Mechanical models	31
3.1 Mechanism	32
3.2 Hinged connection	34
4 Testing procedure	39
4.1 Specimens	39
4.2 Test plan	41
5 Finite element analysis	45
5.1 Cylindrical connection models	45
5.2 Test setup models	53
6 Analysis of results	67
6.1 Connection stiffness	68
6.2 Friction	72
6.3 Limit state test	72
7 Connection specifications and design	83
7.1 Contact mechanics	83
7.2 Connection performance	86
7.3 Critical dimensions and details	90
8 Conclusion	95
9 Recommendations	97
Bibliography	99
A Interface test data	101
B Crack analysis	106

1 Introduction

Connections in concrete civil engineering structures come in many shapes and forms. A typical floor to wall connection can be cast together as a monolithic joint or kept free to rotate as a hinge. Geotechnical uncertainties in the magnitude of settlements can induce large deformations on sub-surface structures like cut-and-cover tunnels. This case is investigated by the engineering company Witteveen + Bos, named the client in this report. To allow for a relative free rotation between the wall and the floor, a connection is proposed named the cylindrical concrete sliding hinge. Hinged connections in concrete structures have existed since 1880. They have been implemented in civil engineering structures for their high-loadbearing and significant rotational capacity [1]. The client has designed a sliding hinge connection and set up a testing project in cooperation with the Stevin lab at the Delft University of Technology. The sliding hinge connection design with the intended application is shown in fig. 1.1.

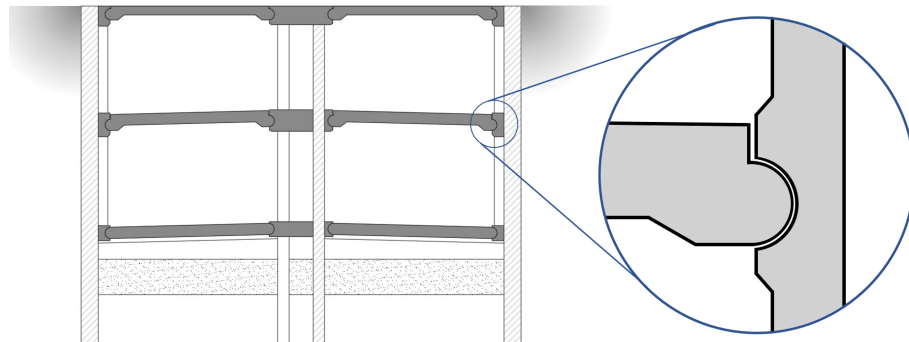


Figure 1.1: Proposed tunnel floor to wall connection

The research project focuses on sliding hinges with a bearing. Positive results, obtained from this research, can have large implications on industrial level. The mechanics of the hinge in the global sense and locally at the bearing is investigated. Material tests are performed by the client to investigate the frictional properties of a range of materials. Two interface materials are chosen and tested in the full scale connection: a elastic PTFE-stainless steel interface and a elasto-plastic bituminous materials are proposed as bearing materials with each vastly different material properties ever changing under load conditions. The engineering practice can benefit from an optimised bearing design for hinged concrete structures in terms of performance and costs. This research is set out to identify the critical variables in the considered design.

1.1 Scope

A plan of action of the test project is provided by the client containing background information, design of the concrete hinge test specimen and the possible test setup [2]. These boundaries will limit the possible research range. The research questions and objectives need to be achievable within the set boundaries:

- Tests are performed on the specimens provided by the client in a pre-established test setup.
- The bearing material choice is limited to PTFE-stainless steel and a bituminous Eshastick material.
- This report will not include research in long-life material or connection behaviour because the normative load is applied in the early stage of the service life.
- The frictional behaviour is based on the Mohr-Coulomb model and is limited to purely dry friction.

1.2 Research questions

The aim of this report is to obtain knowledge about the critical parts of the connection and obtain the limit state of the concrete sliding hinge. This is achieved by answering the research questions.

Main question:

What determines the limit state of a concrete sliding hinge connection?

Sub questions:

- What are the constitutive properties in the loaded sliding connection from the theory of contact mechanics?
- How does a Eshastick bitumen-based interface material behave as an interface material?
- How does a PTFE-stainless steel-based interface material behave as an interface material?
- How does the connection behave under dominant normal force?
- How does the connection behave under dominant shear force?
- How can a non-linear discrete interface be modelled in finite element software to achieve realistic interface behaviour?
- What are critical connection and structure dimensions of a concrete sliding hinge connection?

1.3 Research approach and strategy

A review is made about available literature concerning multiple subjects supporting the research. Firstly, the applications and current technology of concrete hinges is investigated. Secondly, research material about contact mechanics of the sliding connection is studied. Thirdly, more information about the interface materials, namely PTFE and bituminous materials, is examined with the focus on their behaviour under different static and dynamic stress states. Finally, literature about non-linear discrete interfaces applied in finite element software is reviewed.

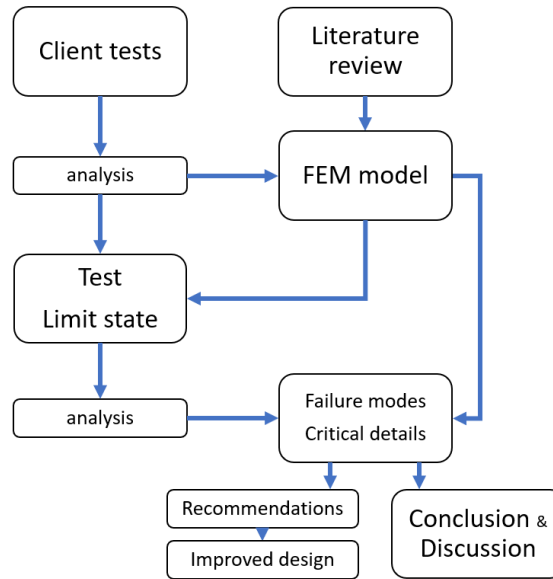


Figure 1.2: Research flow chart

Laboratory research is carried out in the form of multiple experiments, varying in bearing material and in load combinations. In order to obtain the behaviour of the hinge during testing global and local behaviour is measured with the use of displacement sensors and by means of the Digital Image Correlation (DIC) strain measurement technique. The test results are compared and analysed to quantify the connection stiffness and bearing behaviour. Damage patterns of the different experiments are evaluated to identify critical locations for different load combinations. An analytical mechanical model of the connection would help the understanding of the concrete hinge and to explain the obtained results. This process must comply to the prevailing theory. Large deviations from expected analytical calculations must be investigated further to identify discrepancies. The intention is to test the specimens further under significant loads to obtain all the relevant data to answer the research questions (denoted as Test Limit state in the flow chart in fig. 1.2). When initial load conditions do not deliver substantial damage criteria, the load can increase to a set limit. This set limit is based on the capacity of the test setup and general safety in case of specimen failure.

With the use of data from the first set of experiments a finite element model (FEM) is created to improve understanding of the structure. This model is set up to fully incorporate non-linear behaviour, both physical and geometrical. This model can be used to predict the behaviour of the specimens in the test where the load is increased further to obtain more extreme failure modes. This part of the research is based on deductive reasoning in order to seek confirmation of the observed measurement in relation to the FEM results.

With accurate knowledge of the behaviour and actual capacity of sliding hinges in concrete structures a more efficient design can be achieved. With an increase in experience these connections can be applied in more structures sensitive to large rotations. This can potentially result in more economical designs of concrete structures.

2 Literature review

A review is made about available literature concerning multiple subjects supporting the research. Firstly, the applications and current technology of concrete hinges is researched. Secondly, more information about the interface materials, namely PTFE and bituminous materials, is examined with the focus on their behaviour under different static and dynamic stress states. Thirdly, research about contact mechanics of the cylindrical sliding connection is studied. Finally, literature about non-linear discrete interfaces applied in finite element software is reviewed.

2.1 Concrete hinges

The use of concrete hinges found its origin in masonry arches. 19th century arches were made out of stone blocks with varying sizes bounded by mortar [3]. With the introduction of high strength mortar unprecedented spans are feasible. Cracking of this integral structure remained a problem because of settlements of the abutments, temperature induced deformation and asymmetric loading. Integration of hinges can resolve these imposed deformations by turning the arch into an isostatic structure. Jules Dupuit (1804-1866) is the first to introduce the concept of hinges in masonry structures. The uncertainty of the position and shape of the line of trust were mayor drawbacks of classical masonry arches. Dupuit proposes the use of temporary hinges at the springing (bottom supports) and apex (top) of the arch to control the point of rupture. The early concrete sliding hinges are composed out of superior strength stone, cast iron plates and sheets of plumb. These hinges should be mortared after striking the keystone [4]. This technique was not well received in France and therefore not applied at that time. Germany however welcomed the idea and further developed the idea by Emil Winkler (1835-1888) and Claus Koepcke (1831-1911). Further advances in reinforced concrete structures resulted in the design of more complex concrete hinges in the 20th century.

2.1.1 Types of concrete hinges

The different types of permanent concrete hinges developed over the past 150 years are shown in fig. 2.1. These designs and the internal components are explained briefly below.

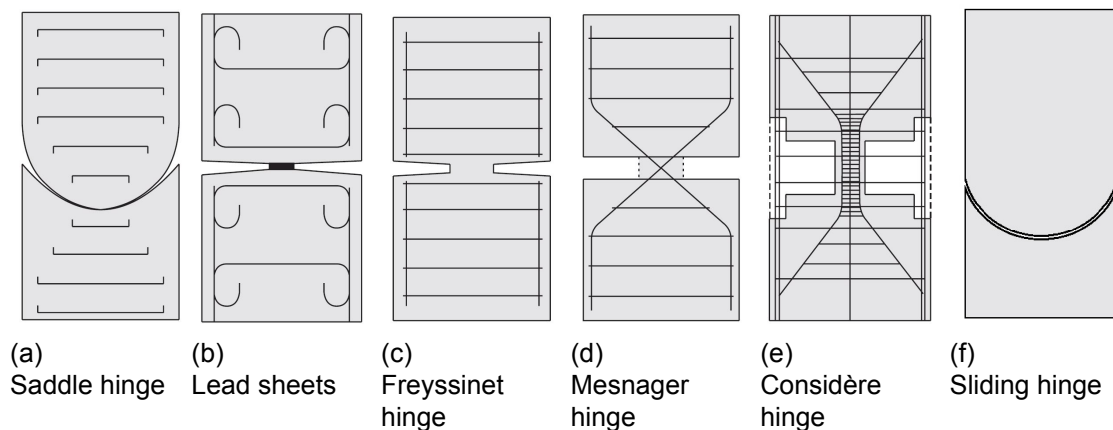


Figure 2.1: Classification of concrete hinges [5][1]

Saddle hinge

The first masonry arch bridge with a hinge was constructed at Langenhennersdorf (Germany) by Claus Koepcke (1831-1911). The revolutionary design consists of concave to convex surfaces of natural stone (fig. 2.2). The intention is to enable rotation without introducing unfavorable stress distribution. The saddle hinge is originally made from granite. With the introduction of concrete as the main building material a higher accuracy in geometry and quality can be achieved. The curved concrete surfaces typically failed by tensile cracking. To prevent this transversal iron bars are implemented in the design often being the only reinforced part of the bridge. [3]

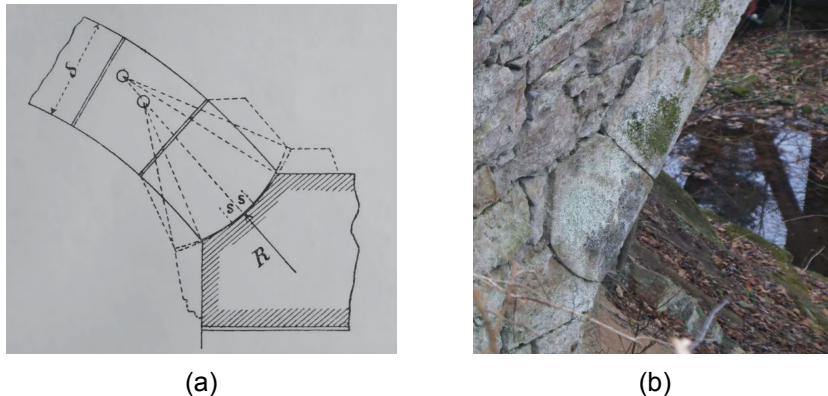


Figure 2.2: (a) Sketch of Koepcke's hinge showing the idealised contact line; (b) Hinge at the base of the bridge at Langenhennersdorf, Germany [3]

Lead sheets

A contemporary of Koepcke, Karl von Leibbrand (1832-1898), independently designed hinged structures. In his designs no special bearing blocks were used. Only a mortar layer between two blocks was replaced by a narrow strip of lead (fig. 2.1b). He expected that the plasticity of the bearing material would redistribute the pressure to be clearly defined [3].

Freyssinet hinge

The French engineer Eugene Freyssinet (1879-1962) suggested a design of a hinge transmitting forces over a restricted area (fig. 2.1c). This geometry would ensure that no dirt would collect in the interface restricting rotation. The hinge throat consists out of unreinforced concrete. Freyssinet expected cracking of the throat resulting in more rotational freedom. However, experiments show no cracking when the stresses are limited to a quarter of the concrete strength and rotations are limited to ensure full compression. The surrounding concrete elements should be carefully reinforced to prevent tensile splitting failure. Empirical design rules are developed based on these experiments for the design of this type of concrete hinge implemented in several built bridges. [1]

Mesnager hinge

Augustin Mesnager (1862-1933) based his design on confined concrete and developed a spring hinge (fig. 2.1d). The reinforcing bars passing through the throat only contribute to the transfer of forces. The concrete surrounding these bars is merely present to prevent buckling and protect the bars from the environment. The bars intersect at the throat and therefore allow a certain rotation. [1]

Considère hinge

Another spring hinge was developed by Armand Considère (1884-1914). He invented a hinge where the concrete of the throat is confined by reinforcement steel in a spiral

configuration (fig. 2.1e). Due to the substantial confinement of the concrete a higher concrete compression strength is achieved. This let Considère to abandon all additional reinforcement in the throat and rely solely on the concrete to provide the load bearing function. [6]

Sliding hinge

The first application of sliding hinges can be traced back to three-hinged arch constructions in the beginning of the 20th century. A convex cylindrical shaped member fits in a member with the same radius (fig. 2.1f). The members are often separated by a thin lead sheets to reduce the strict geometrical accuracy requirements. Additionally, the lead would reduce the friction between the two members. [7]

2.1.2 Sliding concrete hinge

The sliding hinge can be seen as a combination of a saddle hinge and a lead sheet hinge. Not much is known about the applications and the behaviour of sliding hinges compared to the other hinge types. The University of Illinois performed test on the various types of concrete hinges [7]. Among these is the sliding hinge connection with lead plates. Three types of test were performed. Vertical load trough the axis of the hinge, oblique or diagonal load tests and rotational load tests are performed. The sliding hinge specimens for each of these tests had a specific shape and is shown in fig. 2.3.

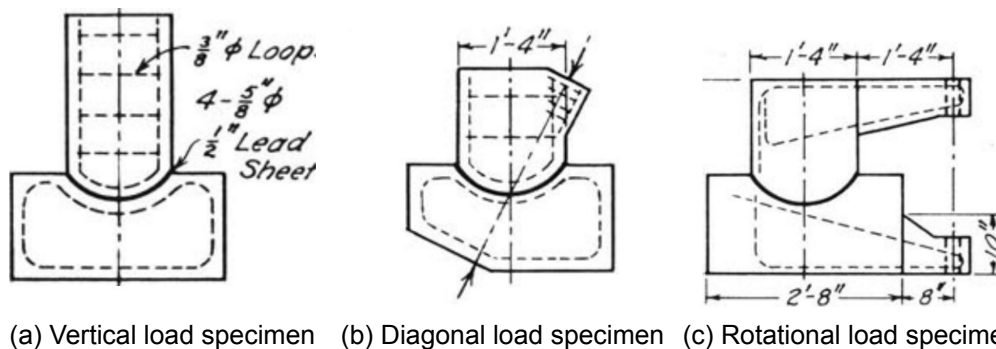


Figure 2.3: load specimens University of Illinois [7]

According to Kluge (1940), “A properly designed hinge, besides being sufficiently flexible to permit a given angular rotation, should be capable of withstanding compressive forces as well as shearing forces, be economical to construct, and require a minimum of maintenance.” (p. 5). The tests are aimed to validate these requirements or obtain limitations to the specific hinge types.

The specimen loaded vertically failed by crushing of the concrete from the top part. Cracks perpendicular to the cylindrical surface radiate outward just before failure. The lead interface material remains undamaged. The substantial vertical load resistance is in good resemblance to computed values.

A diagonal load acting on the specimen resulted in compression failure of the bottom part of the setup. This failure can be classified as premature because the failure location is outside the scope of the research. With an altered shape a higher diagonal force capacity can be achieved.

Testing of the rotation capacity included different axial loads to test the friction behaviour of the joint. A relation between the axial load and the moment to overcome static friction is obtained from this test. The results are presented in fig. 2.4a.

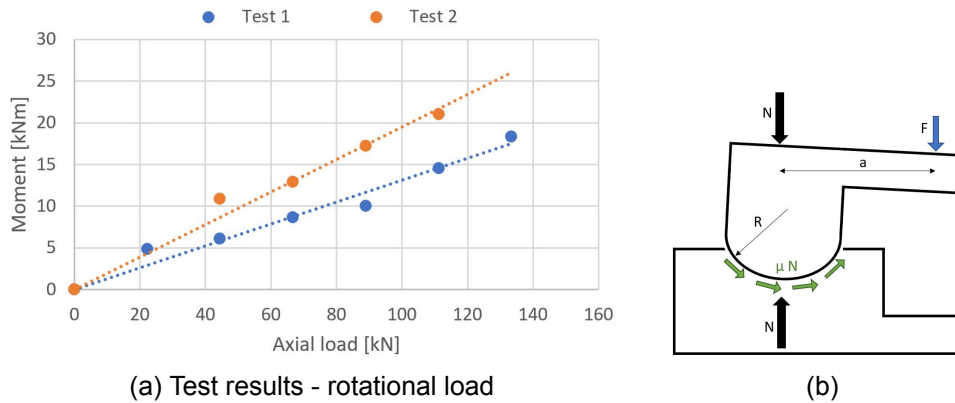


Figure 2.4

The mechanism displayed in fig. 2.4b shows the test conditions and an interface response based on the Coulomb friction model, explained later in section 2.3. Equilibrium of internal and external forces gives: $M = Fa = \mu NR$. Where μ is the nominal friction coefficient relating the interface reaction force to the present normal force. With this model the friction coefficient can be obtained from the test results in fig. 2.4a. The two tests with two different specimens show friction coefficients of 0.7 and 1.0 (for a radius of 0.2 m). The difference in friction between the two tests is assigned to different surface conditions due to difficulty in reproducing specimens. The capacity of the specimens under the rotational load was 15 % lower compared to the performed tests without rotation. This reduced capacity is caused by concrete compressive failure. The interface material remains undamaged when subjected to the rotational load [7].

2.1.3 Application of cylindrical hinges

Curved or cylindrical sliding bearings are predominantly used in the mechanical engineering field. Rotating shafts are supported and guided by slide bearings. At these locations vibrations may be reduced or local perpendicular loads transferred. These bearings can be lubricated or dry [8]. Bushing, plain, journal and pillow block bearings (see fig. 2.5) are commonly used in machinery.



Figure 2.5: Self-lubricating bearing types [9]

In large concrete structures, such as bridges, more complex bearings are applied. When

high loads need to be transferred with specific degrees of freedom disc, pot and spherical bearings can be used. An example of a cylindrical bridge bearing is depicted in fig. 2.6. The base and top plate are made from a high-grade steel and milled to precise tolerances to achieve optimal conforming conditions. The low friction between the chosen interface materials, in this case PTFE to stainless steel, ensures free deformation in the desired directions [10]. The material properties and mechanical behaviour is elaborated in the next sections.

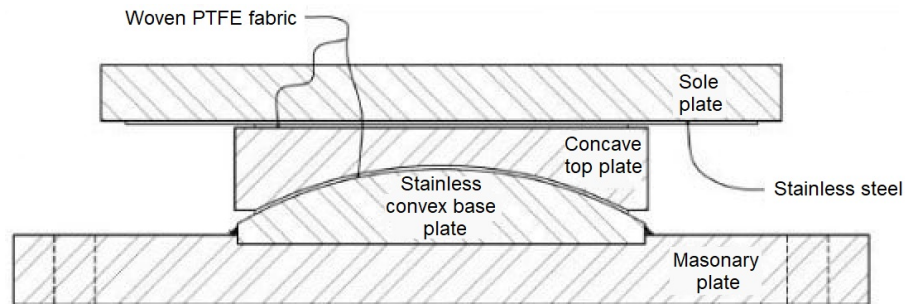


Figure 2.6: Cylindrical bridge bearing [11]

2.2 Sliding interface materials

This section investigates the different interface materials for a concrete sliding hinge connection. First, the requirements of the interface material are set out. Secondly, two different types of interface materials are reviewed. These two types are the bituminous Eshastick and a Polytetrafluoroethylene (PTFE)-stainless steel interface.

2.2.1 Interface requirements

For a concrete sliding hinge to act as a hinge the rotational degree of freedom must be unrestrained. A perfect hinge is impossible because of restricted sliding behaviour in the interface between both bodies. The exact contact mechanics causing this restricted rotation is reviewed in the next section. An example of a restricting action in sliding is friction. The interface between the two bodies should have low frictional properties to act as a hinge. The friction properties of several materials are tested by the Magnel laboratory for concrete research of the Gent University [12]. 10 different interface materials have been tested by the engineering company to investigate the friction properties with a setup as depicted in fig. 2.7. The interface material is applied between the concrete cubes. A constant predetermined normal force is applied horizontally based on the nominal stress in the design. The necessary vertical force is measured to displace the central cube with a specified load plan.

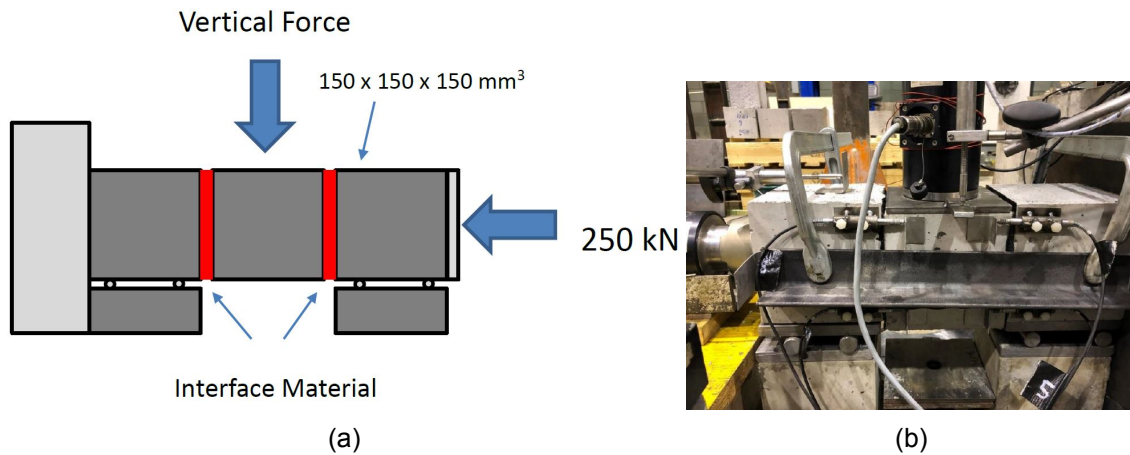


Figure 2.7: Interface material test setup a) Conceptual drawing b) Test setup [2]

A number of plastic-based and bitumen-based interface materials are tested known for their low frictional property. The friction is quantified by determining the friction ratio with eq. (2.1). The explanation behind this formula is covered in the next section. The results from the tests are visualised in table 2.1.

$$\mu = \frac{F}{2 F_N} \quad (2.1)$$

Table 2.1: Observed friction ratios of different interface materials [2]

Plastic	Max. friction force F (kN)	Friction ratio μ (%)
Epramid	242.7	48.5
Multilene	187.8	37.6
HDPE	179.9	36.0
PVC	164.7	32.9
Laurmid	168.2	33.6
PTFE-Concrete	218.4	43.7
PTFE-PTFE	150.0	30.0
Bitumen		
Eshaseal	159.6	31.9
Eshastick	5.4	1.1
Novacell	6.7	1.3

The client chose for each material category (plastic and bitumen) the material with the lowest amount of observed friction: PTFE and Eshastick. The full overview of these results, including force-displacement graphs are elaborated in appendix A. For the implementation of these interface materials a variation was made to the PTFE interface by combining it with a stainless steel counter surface. Finally, the durability is investigated. In an ideal case the interface service life would be the same as the lifetime of the structure. The condition of the interface can be improved during its service life with scheduled maintenance. Only general durability properties of the interface materials will be set out.

2.2.2 Eshastick

Bitumen is a viscous mixture of carbon hydrates remaining after the distillation of crude oil. On a simplified colloidal (larger than atoms, 1-1000 nm) micro-structure level, bitumen is a combination of elastic solid particles in a visco-elastic matrix. Bitumen has time and thermo-mechanical dependent properties and will therefore behave from elastic to visco-elasto-plastic [13]. A bituminous interface can slide at the interface between the bitumen and the concrete. This behaviour is governed by the shape and roughness of both sliding planes and the normal force present in the connection [14]. From the before mentioned small scale friction tests a coefficient of friction of 1% is observed for the bituminous Eshastick interface in the results presented in appendix A (The coefficient of friction is explained further in section 2.3). The sliding behaviour before reaching this friction plateau is governed by the shear stiffness and mechanical interlocking adhesion (see section 2.3). The initial sliding stiffness of this specific interface material can be obtained from testing with the results presented in fig. 2.8. According to this test a sliding stiffness of 0.33 N/mm^3 is acquired. When the bitumen adheres to the concrete a shear connection will be present limited by the shear capacity of the bitumen.

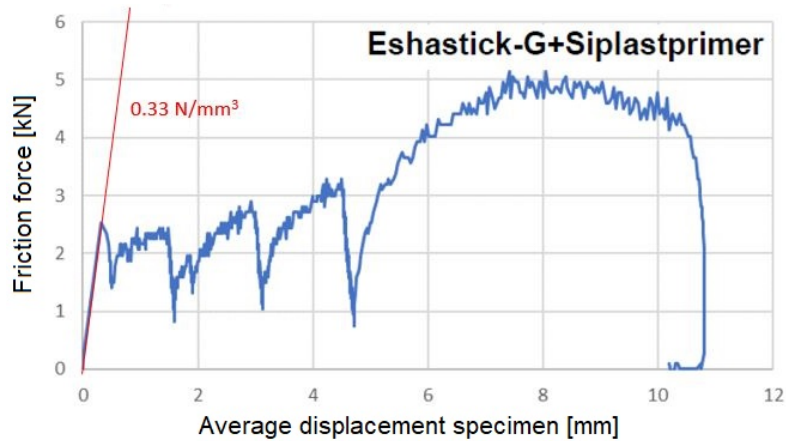


Figure 2.8: Vertical force vs displacement for a Eshastick based interface [15]

Eshastick can be classified as an asphalt reinforcing system. The product is composed out of a bitumen drenched glass fiber fabric enclosed by self-adhesive bituminous layers. The bottom is covered with removable plastic foil. The top is finished with sand [15]. This product is provided as a mat with a thickness of 3 mm.



Figure 2.9: Application of Eshastick [15]

This system is designed for reinforcing road surfaced as a Stress Absorbing Membrane Interface (SAMI). Reflective cracks, due to disturbances in the sub layers, in newly resurfaced asphalt roads can be prevented when applying this system. Additionally, existing cracks in road surfaces can be repaired by applying this material. The mats must be placed between a specific asphalt layers at critical locations to have optimal effect (see fig. 2.9) [15].

Aging of bituminous materials has a significant impact on the mechanical properties. Over time the viscosity and stiffness will increase possibly forming a brittle mixture. Stiffness-based criteria of fatigue resistance are therefore not a proper way to determine the durability. However, the stress relaxation capability is more essential in determining the durability. With a reduced stress relaxation behaviour cracking becomes more prominent. Increasing time, pressure and mostly temperature will result in higher residual stresses [16]. Fatigue deterioration from cyclic loading shows a decrease in stiffness without the appearance of microcracks or structural changes such as metallic materials would. The

bitumen can even recover some, or all, of its initial stiffness when the material is allowed to rest. The strain amplitude of the load cycle determines the stiffness loss. [17]

2.2.3 PTFE to stainless steel

Polytetrafluoroethylene (PTFE) or Teflon was developed by the chemical company Chemours DuPont in 1938. The self-proclaimed favorable properties of this material are [18]:

- Chemical inertness
- Non-stick / Self cleaning
- Low friction / Self-lubricating
- Dielectric properties
- Weather resistance / Non-ageing
- Insensitive to UV radiation
- Non-toxic
- Broad temperature range (- 200 °C / up to + 260 °C)
- Non-flammable

The low friction, self-lubricating, weather resistant and non-ageing properties of PTFE are properties beneficial for the considered application as a bearing. The self-lubrication properties can be considered as a distinctive feature, demonstrated by the creation of a fine PTFE film during sliding, significantly reducing the friction. PTFE consists of carbon polymers with strong carbon-fluorine bonds. These bonds protect the carbon chain from chemical attack and reduces the surface energy resulting in a non-stick low friction material. To achieve these properties extremely high molecular weight polytetrafluoroethylene is produced. This in turn will create difficulties in thermoplastic production processes because the material will have an extremely high melt viscosity [18].

From the before mentioned small scale friction tests a maximum coefficient of friction in a PTFE-PTFE interface of 30% is observed followed by a friction 3 times lower when sliding is initiated (see appendix A). The sliding behaviour before reaching the maximum static friction is governed by the sliding stiffness. fig. 2.10 shows the relation between the acting force and sliding displacement with an initial sliding stiffness of 9.06 N/mm^3 .

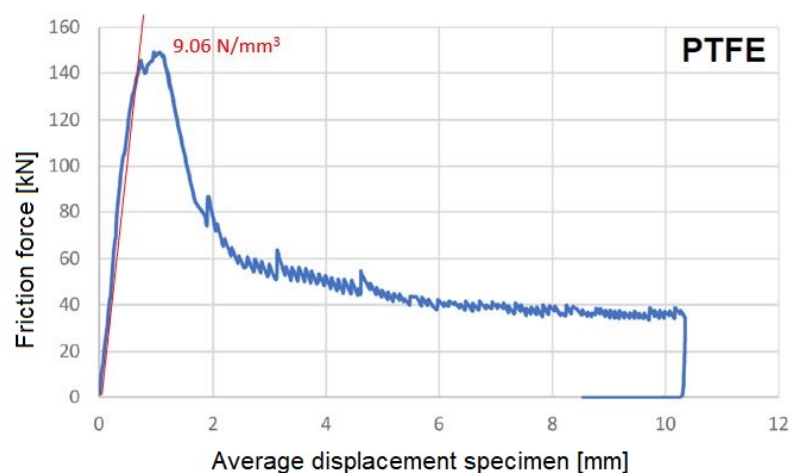


Figure 2.10: Vertical force vs displacement for a PTFE based interface [15]

The combination of PTFE and stainless steel is often used (see fig. 2.11). An example of an application can be seen in the spherical bridge bearing of fig. 2.6. In the case of a large bearing the PTFE surface needs a stable friction counter surface. Stainless steel is ideal because of its formability and rigidity. The interface behaviour of this connection is dependent on many factors. The surface roughness of the stainless steel effects the friction behaviour and more importantly the wear of the PTFE [19]. The friction coefficient between PTFE and stainless steel is around 5 % [20][21] depending on the sliding speed.

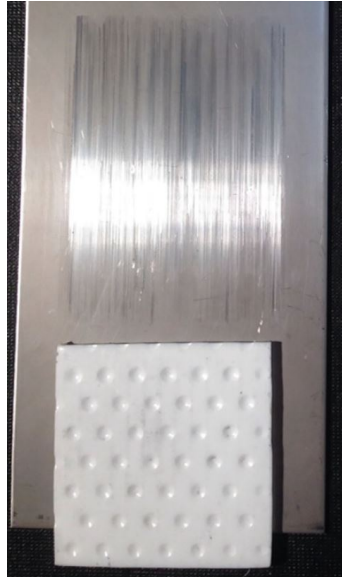


Figure 2.11: PTFE to stainless steel friction and wear test [22]

The PTFE can be reinforced to increase the bearing capacity and prevent creep. In the past, glass fibres were added to construct complex convex shapes and to prevent creep. This development is discontinued due to scratching of these fibres on the stainless steel resulting in larger friction [22]. Besides glass fibers different fillers are used to strengthen the PTFE matrix. Adding bronze or graphite particles does not influence the friction behaviour and wear when the particle size is sufficiently small. The creation of a PTFE film during loading also prevents wear between the added particles and the counter surface [23].

2.3 Contact mechanics

The constitutive properties of a loaded sliding hinge connection are investigated in this section. The theory of contact mechanics is an essential discipline in the engineering sciences. The analysis of stress distribution in bodies in contact is vital in the design process of joints. Friction, wear and lubrication mechanisms are covered by the Tribology discipline. Tribology is defined as "the branch of science and technology concerned with interacting surfaces in relative motion and with associated matters" [24]. Friction is a mechanism which dissipates energy at microscopic level. In many engineering applications this friction is minimized to allow for unrestricted motion [14]. A minimal friction is desired in a connection to act as closely to a hinge as possible. PTFE is known for its non-adhesive property. Bitumen however has significant adhesive properties. The constitutive property of adhesion is elaborated in general and for more complex cases. Different theories concerning the mentioned aspects are outlined and explained in this section.

2.3.1 Hertzian theory

The problem of contact between two curved elastic bodies is solved by Heinrich Hertz in 1882. This was achieved before the time of micro-technology so no expansion to adhesive contact is added. The Hertzian theory is limited to non-conforming bodies. This means that the area of contact is small compared to the radii of curvature of the bodies and the contact surface can be mathematically characterized as an infinity large body, or half plane. Furthermore, only deformations in the elastic range of the material are considered as perpendicular loading to the surface is allowed to neglect shear stresses and friction in the interface [25]. This condition is met when metallic materials with high stiffness are applied to limit the strain to the elastic range. The theory predicts the shape of contact growing with increasing load with the corresponding stress distribution. The contact problem is depicted in fig. 2.12.

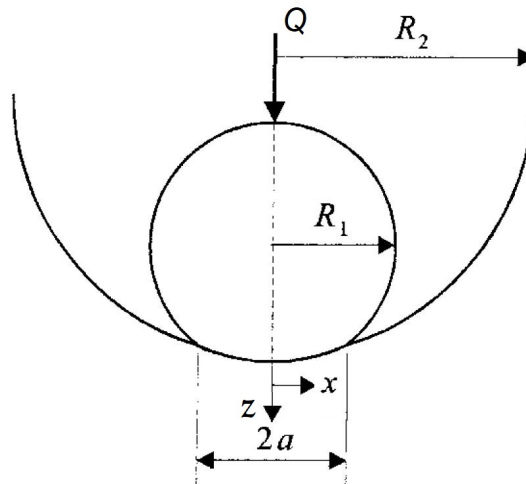


Figure 2.12: Hertzian contact for a cylinder in a cylindrical cavity [26]

Hertz found the parabolic contact pressure distribution well fits the contact area.

$$q(x) = P_0 \frac{\sqrt{a^2 - x^2}}{\sqrt{1 + z^2/a^2}} \quad \text{for } x \leq a \quad (2.2)$$

Where P_0 is the maximum Hertz pressure at the center and zero at the outer edge of the contact half width a . The z coordinate is presented according to the polar coordinate system radiating out from the contact surface. The integrated pressure over the contact area is equal to the total pressure per unit length Q . From this the maximum pressure can be derived:

$$Q = \int_{-a}^a q(x) dx \rightarrow P_0 = \frac{2Q}{\pi a^2} \quad (2.3)$$

The half width is calculated by differentiating the displacement field eq. (2.4).

$$a = \sqrt{\frac{4QR_e}{\pi E_e}} \quad (2.4)$$

Where R_e is the equivalent radius and E_e is the equivalent Young's Modulus calculated from:

$$\frac{1}{R_e} = \frac{1}{R_2} - \frac{1}{R_1} \quad (2.5)$$

$$\frac{1}{E_e} = \frac{1 - \nu_1^2}{E_1} + \frac{1 - \nu_2^2}{E_2} \quad (2.6)$$

where R_i is the radius, E_i is the Young's Modulus and ν_i the Poisson ratio of the respected body. When a situation is created where $a = R$ the contact pressure distribution can be visualised in a contour plot. The stress field is normalised by dividing the result by the contact force.

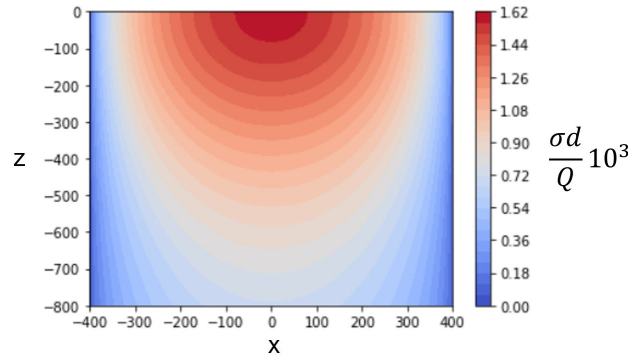


Figure 2.13: Normalised normal stress field (full contact with $R = 400$)

Tangential tensile stresses are present along the interface reaching their maximum at the apex of the curved contact surface. The stresses can be evaluated with eq. (2.7) at this part of the interface in the z -direction away from the surface. [27]

$$\sigma_t(z) = \frac{1}{d} 2\nu P_0 \left(\sqrt{1 + \frac{z^2}{a^2}} - \left| \frac{z}{a} \right| \right) \quad (2.7)$$

Where d is the length over where the cylindrical interface is present and the forces are spread.

2.3.2 Other relevant theories

The Hertzian theory of contact is only correct for specific conditions. When the radii of the considered bodies are conforming the Hertzian theory does not hold. The contact area size is comparable to the dimensions of the two bodies resulting in contact stresses depending on the general stress distribution. The solution to this extended problem was first solved by Steuermann in 1939. He assumed the gap between the two bodies by a power series. With finite difference methods a pressure distribution can be solved. By including the higher order terms this solution better matches the conditions compared to the Hertz equations [26]. Persson (1964) solved the problem with the same contact criterion in a different way. He assumed the contact surface to be cylindrical and formulated the boundary condition as an integro-differential equation. Persson calculated the pressure distribution of a vertical force applied on a disc in an infinite plate with a circular hole (fig. 2.14) [28].

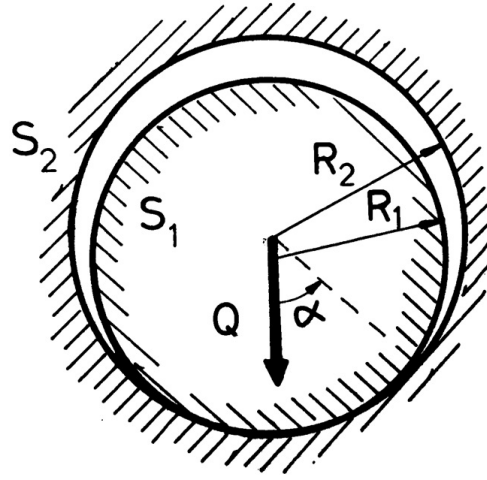


Figure 2.14: Hertzian contact for a cylinder in a cylindrical cavity [28]

Persson solved the pressure distribution in the contact region for conforming bodies with identical material properties, simplified conforming bodies ($R_1 \approx R_2 \approx R$):

$$q(y) = \frac{2Q\sqrt{b^2 - y^2}}{\pi R(1 + y^2)\sqrt{1 + b^2}} + \frac{F}{2\pi Rb^2(b^2 + 1)} \cdot \ln \frac{\sqrt{b^2 + 1} + \sqrt{b^2 - y^2}}{\sqrt{b^2 + 1} - \sqrt{b^2 - y^2}} \quad \text{for } -b \leq y \leq b \quad (2.8)$$

Equation to solve for the contact coordinate b :

$$\frac{E(R_2 - R_1)d}{N} = \frac{2}{\pi} \frac{1 - b^2}{b^2} - \frac{I_6}{\pi^2 b^2(1 + b^2)} \quad (2.9)$$

With:

$$I_6 = \int_{-b}^b \frac{\ln \left(\frac{\sqrt{b^2 + 1} + \sqrt{b^2 - t^2}}{\sqrt{b^2 + 1} - \sqrt{b^2 - t^2}} \right)}{1 + t^2} dt \quad (2.10)$$

Where the elastic displacement field is presented as $y = \tan(\frac{\theta}{2})$ for the interface angle θ and the contact coordinate as $b = \tan(\frac{\alpha}{2})$ or as the variable t in eq. (2.10). The contact

angle α is the angle of full contact between the two bodies. Ciavarella and Decuzzi (2000) extended this problem for elastic dissimilarity and found that the pressure distribution only depends on the area of contact. This area depends on the loading conditions and the material parameters. All results from Persson hold for the strength of the contact because the effect of dissimilarity is negligible for the dimensionless pressure distribution [29][30]. The pressure distribution over the contact range from the Hertzian eq. (2.2) and Persson eq. (2.8) theory is presented in fig. 2.15 for conforming contact. According to the analytical formulations of the contact stresses a further generalisation can be made to the stress distributions by multiplying the stresses by the element thickness d and dividing by the applied axial force.

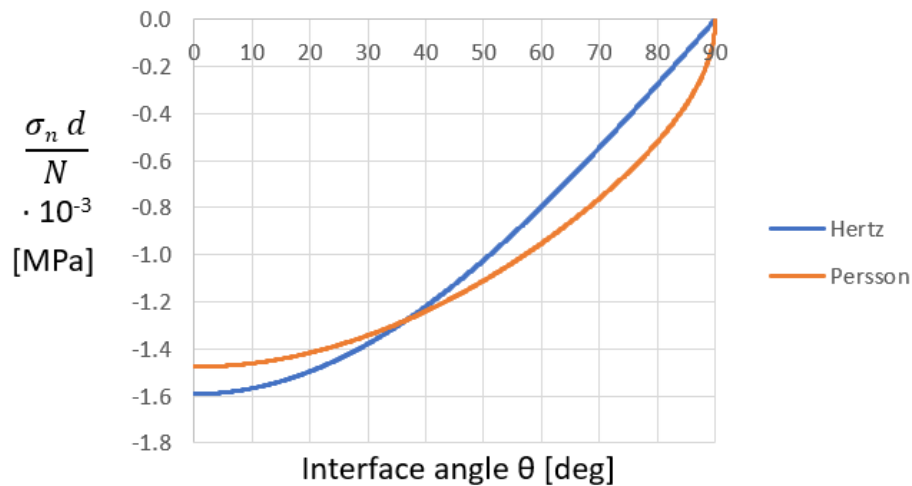


Figure 2.15: Generalised normal stress Hertz vs Persson

With the stress normal to the contact face $\sigma_n = \frac{q(\theta)}{d}$. From the graphs it is visible that the Hertzian theory shows a larger maximum pressure in the base of the contact area and a lower pressure at the outer edges of the contact compared to the Persson theory. This effect is enhanced for increasing contact angles. To complete the solution to the problem of elastic similar conformal cylindrical contact the internal stress field is required. Persson provided the closed form stress distribution at the contact line for friction-less contact.

The Hertzian model of contact between smooth bodies was extended in 1971 with the JKR model after observations diverging from the theory. For elastomeric materials under low loads greater contact area was observed than expected with strong adhesion between the bodies. The additional contact forces are identified to originate from Van der Waals bonding and thus the surface energy of the materials [31].

2.3.3 Friction

Leonardo da Vinci first described the friction phenomena in his Codex-Madrid in 1495. He performed experiments to obtain alloys with low friction. Da Vinci derived two fundamental laws of friction [14]:

1. The frictional force is proportional to the normal force.
2. The frictional force is independent of the contact surface area.

The friction ratio following from the experiments showed a typical value of $\frac{1}{4}$ between metallic surfaces. This relation was forgotten over time but rediscovered 200 years later by Guillaume Amontons [14].

Amontones received the credit for the proportionality of the frictional force known as Amontons' Law:

$$F = F_N \cdot \mu \quad (2.11)$$

Where F_N is the normal force and μ is the friction ratio.

The laws of friction are satisfied in the majority of unlubricated sliding actions. Polymers with a low stiffness and hardness often do not follow these laws. Coulomb (1781) extended the laws of friction with the following law: The frictional force is independent of the sliding velocity. It must be noted that all these laws are based on empirical observations with no physical basis. This third law is only valid for dry friction and a moderate range of sliding velocities.

Mohr-coulomb

Coulomb tested many different material combinations, surface compositions and sliding speeds. A distinction is made between static friction and dynamic friction. Static friction is the region where no relative movement takes place and the force of static friction increases to a critical force. The kinetic friction describes the behaviour between two sliding bodies in motion. The coefficient of dynamic friction (μ_k) is typically lower than the coefficient of static friction (μ_s). A typical example for friction behaviour between two bodies is presented in fig. 2.16. Here some relative displacement is observed in the static regime originating mainly from shear deformation of the interface. Dynamic friction is discerned by relative sliding displacement present between the interfaces.

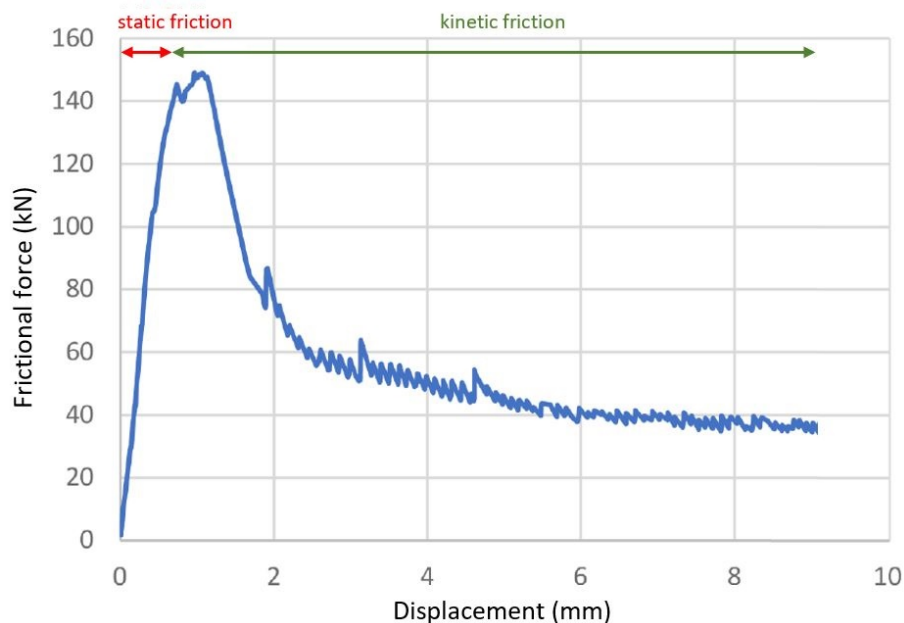


Figure 2.16: Friction PTFE-PTFE test project Oosterweel [12]

The distinction between static and kinetic friction cannot be made on microscopic level. The transition is continuous and in some case static friction can emerge as kinetic friction with a very low velocity [14]. Another observation by Coulomb is the rise of the static force with a logarithmic increase in the amount of the time an object remained stationary. [24]. This dependency cannot be easily explained for all cases. For metallic materials the increase of friction can be attributed to creep processes at atomic scale. Elastomers are

influenced by their visco-elastic property resulting in this behaviour. Coulomb's view on the physical origin of friction is based on the interaction between the surface roughnesses between two bodies. this is depicted in one of his original sketched in fig. 2.17a.



Figure 2.17: Interaction between the surface roughnesses between two bodies, [14]

The problem is simplified in fig. 2.17b as a point mass acting on a corrugated surface. The coefficient of friction is determined in terms of the inclination angle θ . The equilibrium conditions of the free body diagram are as follows:

$$x : R \cdot \sin(\theta) = F \quad y : R \cdot \cos(\theta) = F_N \quad (2.12)$$

Combining these equation gives:

$$F = F_N \cdot \tan(\theta) = F_N \cdot \mu \quad (2.13)$$

This theory is extended with the collaboration of Otto Mohr resulting in the Mohr-Coulomb failure criterion. This criterion is a set of linear equations describing the conditions for which an isotropic material will fail. The criterium can be expressed in the major stress (σ_I) and the minor stress (σ_{III}) or the normal stress (σ) and shear stress (τ). The intermediate stress (σ_{II}) is neglected in this model. Mohr's contribution is the condition of failure depending on σ_I and σ_{III} displayed on the failure plane in relation to the failure envelope for a combination of σ and τ . The relation between σ and τ can be nonlinear [32]. The Mohr diagram and Coulomb failure envelopes is shown in fig. 2.18.

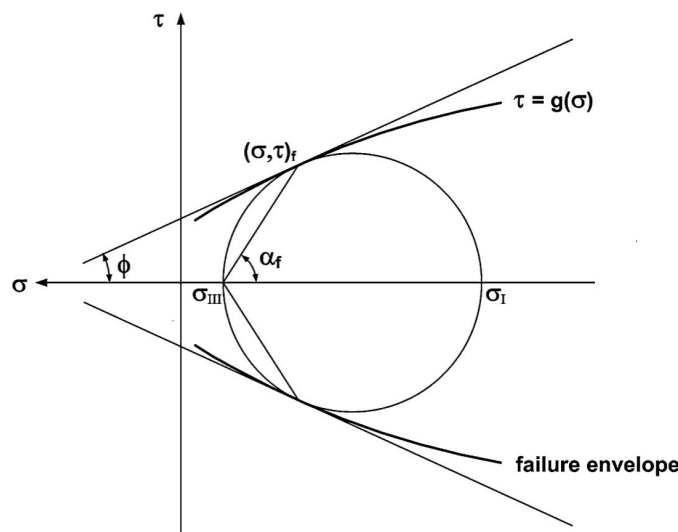


Figure 2.18: Hertzian contact for a cylinder in a cylindrical cavity [32]

Coulomb proposed a typical linear relation between the shear and normal stress from his investigations of soil mechanics:

$$|\tau| = c + \sigma \cdot \tan(\theta) \quad (2.14)$$

Where c is the cohesion describing the inherent shear strength of the material. From Mohr's circle it can be observed that:

$$\tau = r \cdot \cos(\theta) \sigma = \sigma_f - r \cdot \sin(\theta) \quad (2.15)$$

With $r = \frac{\sigma_I - \sigma_{III}}{2}$ and $\sigma_f = \frac{\sigma_I + \sigma_{III}}{2}$. Combining eq. (2.14) and eq. (2.15) gives:

$$c \cdot \cos(\theta) + \sigma_f \cdot \sin(\theta) = r \quad (2.16)$$

The Mohr-Coulomb failure surface is a hexagonal cross section in the deviatoric plane (see fig. 2.18). For $\theta = 0$ the failure surface reduces to the Tresca model. For $\theta = 90$ the model would reduce to the Rankine model [33].

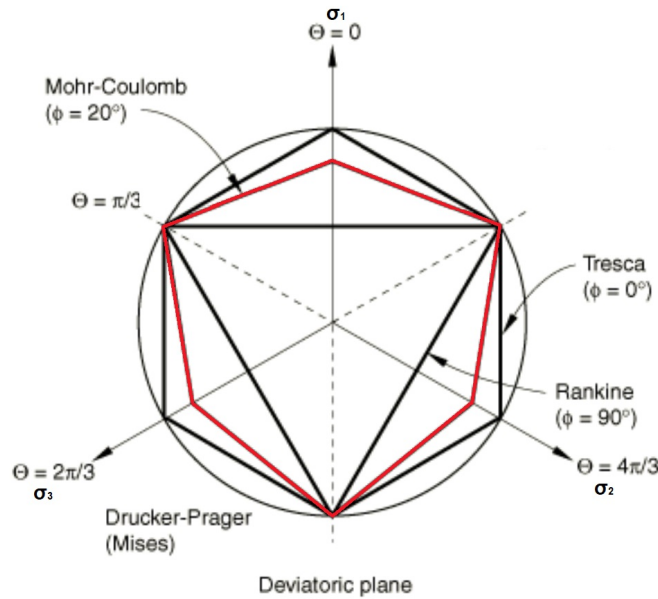


Figure 2.19: Yield surface in the deviatoric plane for different theories. [33]

The advantage of the Mohr-Coulomb model is the simplicity and clear physical meaning. The yielding behaviour creates problems in the corners of the deviatoric plane as opposed to the smooth Drucker-Prager (Von Mises) function as can be seen from fig. 2.19 [32].

Friction parameters

The coefficient of friction depends on a variety of parameters. The influence of these parameters are not covered with the Mohr-Coulomb model. The relation of the frictional force to the normal force can deviate from the described model for some cases. When the real contact area is evaluated the dependence is no longer valid. For soft metals, e.g. lead, or visco-elastic polymers or elastomers the relation holds only for a certain force domain. The influence of contact time to friction was already discovered by Coulomb and described in the previous part. The third law of friction states that the frictional force is

independent of the sliding velocity. This law for kinetic friction is only valid for a certain velocity range. When the coefficient of friction decreases with an increase in sliding speed the motion may become unstable and give rise to frictional instabilities. The roughness of a specimen is used as an explanation of Coulomb's laws of friction. However, smooth surfaces can even create higher friction compared to rough surfaces. This can be caused by material impurities or the creation of interface films. The coefficient of friction is not dependent on temperature when the material composition or state does not change. When a softening or melting temperature is subjected to the friction action large increases or decreases in friction can be expected [14] [24]. PTFE is a material with a moderate static coefficient of friction, but when sliding occurs under large normal forces a thin film is created. This film gives rise to a significant reduction in friction with highly aligned polymer chains. [24]

2.3.4 Adhesion

A certain amount of adhesive force is always present between two bodies. Of influence are the surface smoothness, material softness and microscopic systems of a body. At atomic level Van der Waals forces are presented between electrically neutral atoms. These forces depend on the relative distance and the surface energy density γ . The Lennard Jones Potential describes the potential energy (U) of interaction between two particles, repulsive and attractive [34]. From fig. 2.20 it can be observed that for the separation between the particles ' r ' for direct contact ($r = r_0$) the potential energy reaches its minimum.

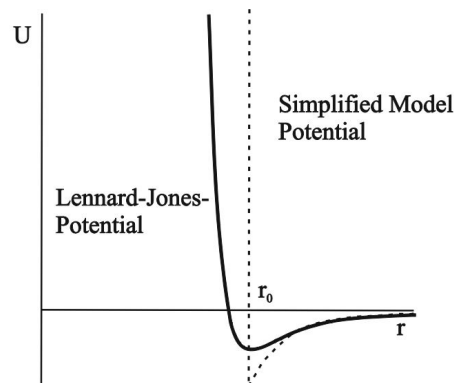


Figure 2.20: Lennard-Jones-potential and the simplified model potential [14]

The van der Waals stress for direct contact is:

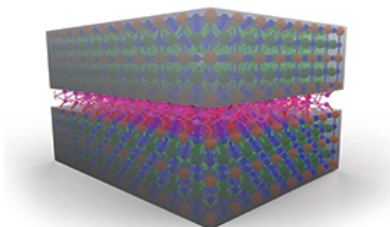
$$\sigma = \frac{F}{A} = -\frac{4\gamma}{r_0} \quad (2.17)$$

For metallic interaction, the γ has a value of $1-2 \text{ J/m}^2$ with $r_0 = 4 \cdot 10^{-10} \text{ m}$. This results in the ability of 1 cm^2 of surface area to hold 100 tons of weight. These adhesive abilities are not observed in reality. The explanation can be found on a macroscopic scale at the surface of a body. The molecular bond is never homogeneous due to existing flaws. The assumption of complete smoothness cannot be achieved resulting in an extreme overestimation of the adhesion. The shear stiffness combined with roughness parameters gives the adhesive property of a material. This relation can be described as linear for the shear stiffness of a material resulting in an approximately 5 times higher adhesion for elastomers compared to stiff metals [14].

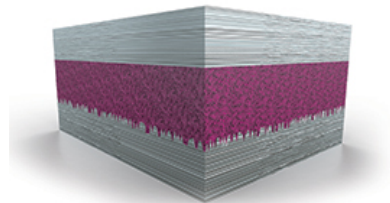
Adhesion types

Producers of adhesive bonding products rely on a variety of adhesion types. Each adhesion type works at a different scale and is applicable for a small amount of situations. four common recognized methods are [35]:

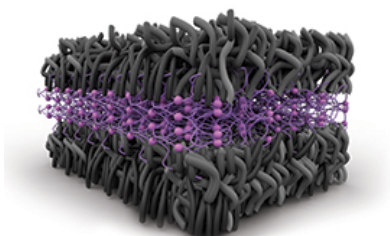
- Chemical adhesion: relies on molecular contact of the surface and substrate. The strongest adhesion type and the bases of epoxy bonding various materials (see fig. 2.21a).
- Mechanical Interlocking Adhesion: where adhesive flows penetrate the pores of the substrate providing a mechanical interlocking. Prevents crack propagation and increase the adhesion contact area. Surface preparation and curing techniques are vital for a durable bond. Flow of adhesion continues to flow over time, increasing the strength (see fig. 2.21b).
- Diffusion Adhesion: is based on adhesive polymers penetrating and entangling with a substrate composed out of polymeric material. The adhesion connects the polymer chains of the substrate. Low surface energy materials (e.g. PTFE) are suitable for this mechanism (see fig. 2.21c).
- Electrostatic Adhesion: relies on electrostatic charge of surfaces to adhere with oppositely charged adhesive material. This bond is often relied upon for tape. The applications are limited due to the relative low bond strength (see fig. 2.21d).



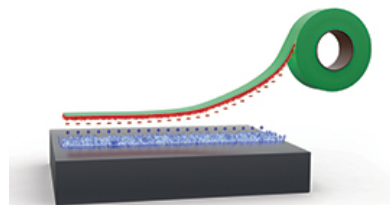
(a) Chemical adhesion



(b) Mechanical Interlocking Adhesion



(c) Diffusion Adhesion



(d) Electrostatic Adhesion

Figure 2.21: Adhesion types [35]

Adhesive friction

When smooth surfaces are in contact under large loads the true area approximates the apparent area of contact. From the Hertzian theory the contact area (a) of two cylindrical bodies is proportional to the load (Q or F_N) to the power 1/2 (see eq. (2.4)). When the coefficient of friction is presented as the limiting case for plastic deformation:

$$\mu = \frac{F}{F_N} = \frac{\tau_{mean} 2aL}{F_N} \propto \frac{F_N^{\frac{1}{2}}}{F_N} \propto F_N^{-\frac{1}{2}} \quad (2.18)$$

In eq. (2.18) it is clear that the coefficient of friction tends to decrease for increase normal force. This behaviour is observed for polymers and can be explained by the weak chemical bonding between the polymer chains. Adding to this reduction of friction is the creation of a polymer film for contact against hard counter surfaces. The bond between the created film and the counter surface is often stronger than its connection to the bulk material. The coefficient of friction of polymers do depend significantly on the normal force present. This normal force creates a hydrostatic pressure (P) in the material influencing the shear yield stress (τ) with the following relation :

$$\tau = \tau_0 + \alpha P \quad (2.19)$$

Where τ_0 and α are parameters determined for polymers with conventional mechanical tests. This relation is also present in the coefficient of friction:

$$\mu = \frac{F}{F_N} = \frac{\tau}{P} = \frac{\tau_0}{P} + \alpha \quad (2.20)$$

The coefficient of friction tends to decrease for increasing hydrostatic pressure and converge to α . [24]

2.4 Discrete non-linear interfaces in finite element models

The bearing of the concrete hinge has specific properties which are examined by material testing. This data has to be implemented correctly in a computational model to obtain prevailing behaviour. A localised interaction between parts of a finite element model with significant changes in constitutive behaviour can be modelled in several ways. A distinction can be made between a continuum and discrete approach. Continuum elements can be applied to create a smeared interface at locations where specific boundary conditions are met. This approach is ideal for when the location of the exceedance of these boundary conditions is unknown. An example is the formation of cracks in concrete where the principle stress exceeds the tensile capacity. The discrete approach to modelling the interaction between different parts of the model relies on localized interfaces. A precondition is that the location of the interface is known. The properties of these interface can be customized to comply with true physical behaviour. The cylindrical sliding interface of a concrete hinge is ideal for a discrete modelling approach. This chapter elaborates discrete interfaces in finite element models. The principles and constitutive properties are investigated. Following this, non-linear properties of the interface are explained on the basis of specific applications.

2.4.1 Constitutive behaviour

Discrete connections are composed of three different elements:

- nodal interface elements
- Two-dimensional line interface elements
- Plane interface elements

The interface surface and directions of the nodal interface elements are user-specified in contrast to the other two types where these are evaluated automatically from the geometry. The interface elements describe the interface behaviour with a relation between the normal and shear traction (t_n & t_s respectively) and the normal and shear displacement (Δu_n & Δu_s respectively). The variables are displayed in fig. 2.22 for a two-dimensional line interface.

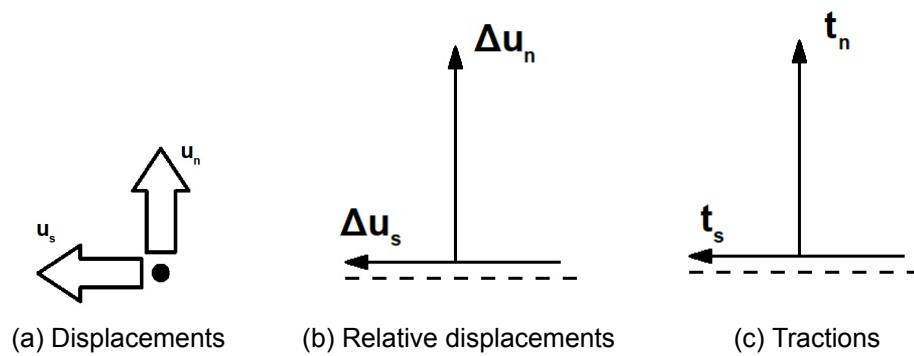


Figure 2.22: Structural 2D line interface variables [36]

The relations between the variables for interface elements with a uncoupled stiffness matrix is expressed as:

$$\begin{bmatrix} t_n \\ t_s \end{bmatrix} = \begin{bmatrix} k_n & 0 \\ 0 & k_t \end{bmatrix} \begin{bmatrix} \Delta u_n \\ \Delta u_t \end{bmatrix} \quad (2.21)$$

Where the normal stiffness $k_n = E/t$ and the shear stiffness $k_t = G/t$ with thickness t . This relation is based on a linear spring mechanism. Different behaviour can be modelled with more complex mechanisms. fig. 2.23 gives an overview of different models describing material behaviour. All models are composed out of spring and/or dashpots with spring stiffness E and damping coefficient η . Elastic material behaviour under direct loading can be described with a spring model. However, when visco-elastic behaviour is expected a model combining a spring and a dashpot is better suited. Simple examples are the Maxwell and Kelvin models where the relation between stress and strain is based on a first-order differential equation. Creep and relaxation are possible mechanisms to be modelled with these elaborated models [37]. The Maxwell model places the spring and dashpot in series resulting in the following stress - strain relation: $\dot{\epsilon} = \frac{\dot{\sigma}}{E} + \frac{\sigma}{\eta}$ describing the visco-elastic fluid behaviour. The Kelvin model is based on a spring and dashpot placed in parallel resulting in the following stress - strain relation: $\sigma = E\epsilon + \eta\dot{\epsilon}$ describing the visco-elastic solid behaviour.

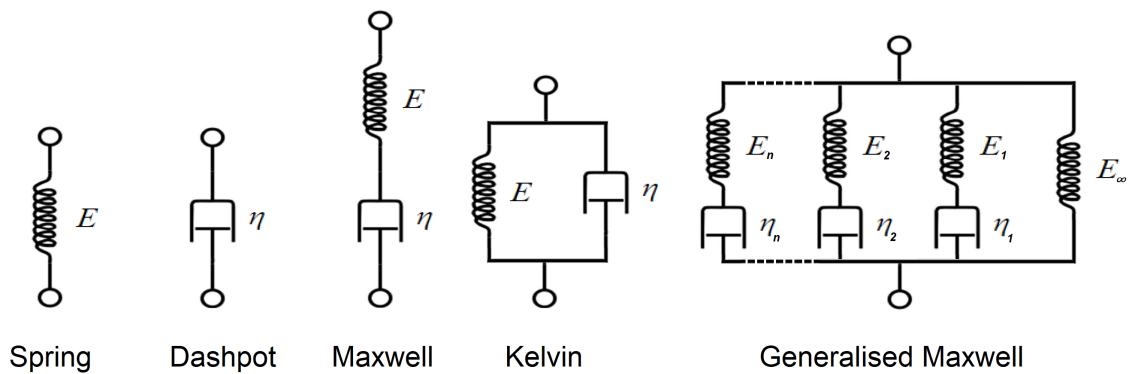


Figure 2.23: Constitutive models [38]

2.4.2 Non-linearity

Considering a sliding hinge, several interfaces are of interest. The stiffness in normal (or radial) and tangential direction does not have to be linear. Bituminous materials can show nonlinear resistance to deformation [39] with even elasto-plastic characteristics. Another example of a possibility with a nonlinear description of the stiffness is an interface with a certain clearance. A relation between the stiffness and relative displacement can be described to allow for a specific clearance. Relations can also be formulated between the radial and tangential component. A good example of this is a Coulomb interface where the shear stress is related to the normal stress by a friction angle limit [21]. Additionally, a no-tension interface can be modelled to display the ability to have only compressive resistance for the opening of an interface and the loss of tensile resistance. Several interface models with a use in the considered sliding hinge connection are elaborated in this section.

No-tension interface

Connections where only compressive forces can be transmitted require a nonlinear formulation of the normal and tangential stiffness. For relative normal compressive (or positive) displacements the interface behaves as a regular interface with specific input stiffness properties. However, when relative normal negative displacement occurs, the interface stiffness must be negligible. This is achieved by imposing a dummy, or penalty stiffness for the case of negative relative displacement. This stiffness difference cannot be too large in order to avoid an ill-conditioned overall system of equations [21]. The penalty parameter should be a function of the mesh size to limit the error due to the penalty stiffness.

$$\Delta u_n < 0 \rightarrow k_{n,p} = p k_n \quad (2.22)$$

Where $k_{n,p}$ is the penalty stiffness and p is the penalty parameter. The penalty parameter must ensure that the elastic response of the penalty stiffness does not have any influence on the overall linear elastic response of the structure [40].

Clearance interface

The clearance present between the two concrete parts of the cylindrical connection (dR) can be implemented in the finite element model without the use of a contact analysis. This interface model is an extension to the no-tension model. only the critical relative normal displacement is set to be equal to the clearance. [21]

Coulomb friction interface

A friction angle with a shear capacity limited by the normal stress magnitude and an input friction parameter can be implemented in a finite element model. This in combination with a no-tension requirement would represent an interface incorporating a sliding mechanism. fig. 2.24 and the equations below show the calculation method of the DIANA TNO software concerning this interface.

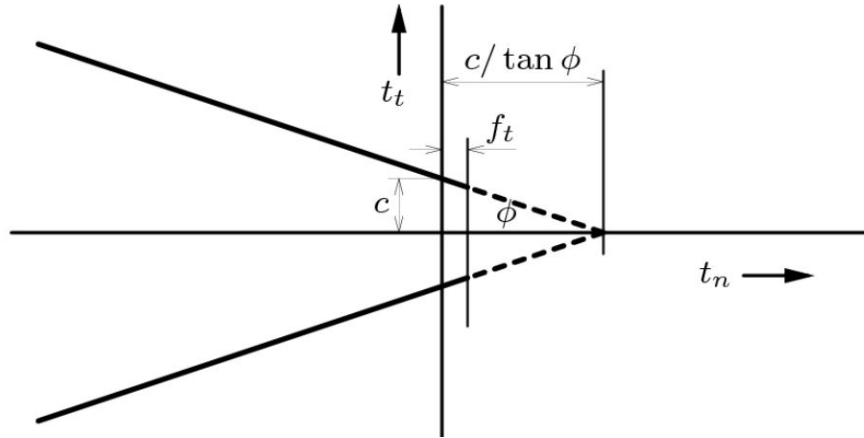


Figure 2.24: DIANA TNO Coulomb friction criterion [36]

Where:

c = cohesion

Φ = friction angle or as a friction coefficient $\mu = \tan(\Phi)$

f_t = tensile strength

This matches the Mohr-Coulomb friction model as described in section 2.3.3. Formulas are rewritten below to include the element traction and clearly show the capacity of the interface. The shear stress capacity ψ and the hydrostatic pressure capacity χ can be calculated in the interface by the finite element software based on the friction angle.

$$\psi = \frac{t_t}{t_{t,max}} \quad (2.23)$$

$$\chi = (t_{t,max} - t_t) \tan(\Phi) \quad (2.24)$$

with the shear traction limit set by the friction angle:

$$t_{t,max} = c + t_n \tan(\Phi) \quad (2.25)$$

Plasticity on element level is determined by the criterion:

$$\begin{array}{ll} \text{Associated plasticity if} & \psi = 1 \rightarrow t_t = t_{t,max} \\ \text{Nonassociated plasticity if} & \psi < 1 \end{array}$$

2.5 Summary of literature

Various concrete hinges have been developed over the last 150 years. The first concrete hinges are implemented in arched structures by means of curved sliding and saddle hinges. More complex reinforced concrete hinge types were designed in the early 20th century based on a constricted connection. These were favoured over the rolling and sliding hinges in the engineering practice because of the freedom in form and less strict contact surface requirements. However, the sliding hinge showed promising results in large scale test projects.

Sliding concrete hinges can be equipped with a bearing to minimise the sliding resistance. Early designs used lead or steel as bearing materials. With the introduction of PTFE in 1938, a new material was available to be implemented in a wide range of bearings for various connections. The low friction of 30% for PTFE to PTFE and as low as 5% for PTFE to stainless steel indicates the potential of PTFE as a bearing. Also, bitumen-based interface materials showed promising low friction in small scale material testing. A friction ratio of 1% was found for the bituminous drenched fiber fabric Eshastick. The added benefit of this material is the limited sliding stiffness observed during small scale testing. The material properties of bituminous materials are however influenced significantly by temperature changes, fatigue deterioration and aging.

Contact stresses resulting from the contact between two circular bodies is investigated with different contact theories. The Hertzian and Persson theory are both able to show comparable contact stresses. The Hertz formulation is more comprehensible but is not able to show correct contact stresses for conforming contact. For the introduction of the friction mechanism in the contact a friction model needs to be implemented. The Mohr-Coulomb friction model can be used when the friction limit of the material is obtained from a known friction force to normal force relation. Adhesion can be implemented in the contact problem by extending the friction formulation with a shear stress limit, dependent highly on the hydrostatic pressure.

The concrete hinge interface can be modelled in a finite element analysis by implementing a discrete line interface. Nonlinear tractions to relative displacement relations can be attributed to the interface matching material parameters. A no-tension relation can be described with the use of an appropriate penalty stiffness for specific relative displacement (or clearances). A limit for the relation between tractions in normal and perpendicular to normal direction is possible with the Coulomb friction interface. These interface specifications combined can display the behaviour as described with the addressed contact theories.

3 Mechanical models

The need for a hinged connection originates from a tunnel structure with specific loading conditions, as defined by the client. These loads are depicted in fig. 3.1 below. The loads indicated in green represent vertical downward loads originating from soil and water pressure in case of the tunnel roof structure and traffic for the intermediate floor levels. The horizontal soil pressure is represented in red. These loads act on the vertical diaphragm walls of the tunnel and are transmitted to the floors as a strut structure. The blue arrows represent vertical loads from the soil to the bottom of the tunnel structure. When soil is removed to build a tunnel weight is removed causing the remaining soil to heave to re-establish equilibrium. The magnitude of the resulting imposed deformations depends on the soil type. For substantial swelling, differing over the contact area, measures must be taken to ensure the structures ability to mitigate these loads.

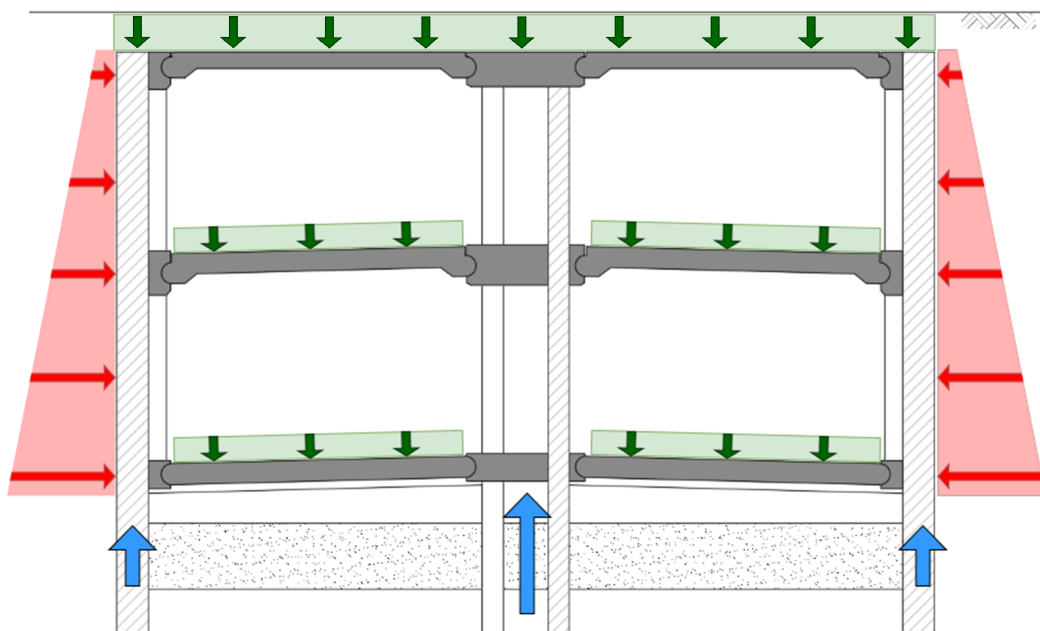


Figure 3.1: Load overview

A specific floor slab can be simplified to a beam supported at the two ends loaded with the described loads. The supports represent the connection between the floor and the wall of the tunnel. Vertical and horizontal loads must be converted to represent the effect of the original loads. Axial and perpendicular forces acting on the beam result in well known axial, shear and bending stresses. In addition to this, the relative imposed deformation (heave) of the beam end will result in a bending moment at the support. The magnitude of this bending moment depends on the amount of rotation in the connection and the rotational stiffness. To minimise the bending moment at the supports a low rotational stiffness of the connection is required.

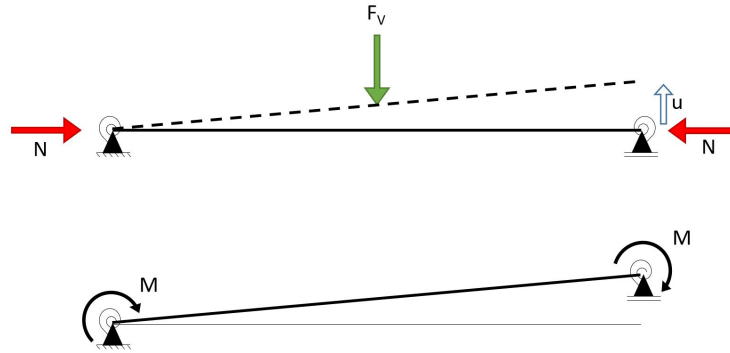


Figure 3.2: Simplified floor loading situation

Where:

N = normal force originating from the horizontal soil pressure

F_V = vertical force representing dead and/or traffic loads

u = imposed deformation

M = bending moment in connection due to imposed rotation

Different connection designs are possible to reduce the rotational resistance. This research is aimed at the application of a concrete sliding hinge. A concrete sliding hinge relies on a bearing between the two bodies to be connected. To achieve sliding with a low amount of restriction in rotation a bearing with low frictional properties is desired.

3.1 Mechanism

The heave of one of the support relative to the other creates a mechanism as shown in the figure below. This model is based on the equilibrium between internal and external work.

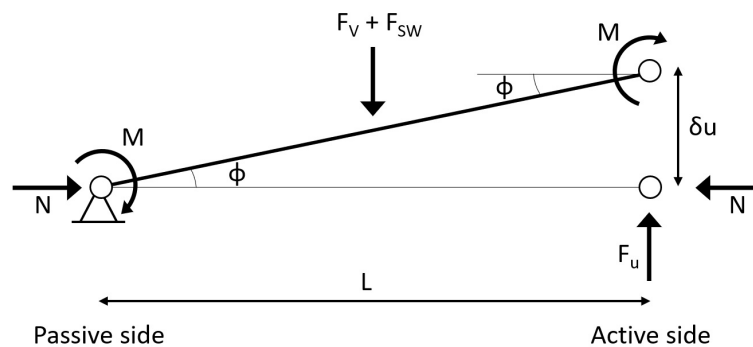


Figure 3.3: Mechanical model

Where:

N = normal force originating from the horizontal soil pressure

F_V = vertical force representing dead and/or traffic loads

F_{SW} = self-weight of the beam

M = bending moment in connection due to imposed rotation

δu = imposed deformation, ϕ imposed rotation

F_u = uplifting force required to achieve the imposed deformation

$$F_u \delta u - (F_V + F_{SW}) \frac{1}{2} \delta u = 2M\phi \quad (3.1)$$

Yields with $\phi = \delta u/L$:

$$F_u - \frac{1}{2}(F_V + F_{SW}) = \frac{2M}{L} \quad (3.2)$$

The term F represents the uplifting force subtracted by the support reaction from the vertical force and the self-weight of the beam:

$$F = F_u - \frac{1}{2}(F_V + F_{SW}) \quad (3.3)$$

The bending moment at the connection becomes:

$$M = \frac{FL}{2} \quad (3.4)$$

A loading setup has been proposed by the client to investigate dominant shear forces on the connection. More extreme shear forces can be admitted to the connection by shifting the vertical load (F_V) to the passive side. Moreover, unwanted rotation due to this load are prevented.

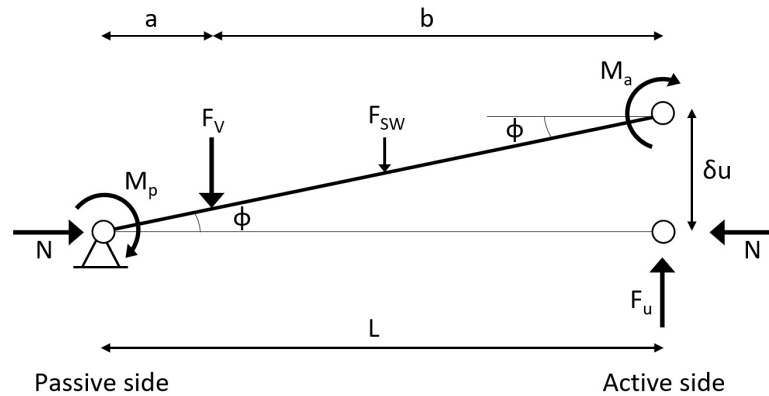


Figure 3.4: Mechanical model: shifted vertical force

Gives the following equilibrium:

$$F_u \delta u - F_{SW} \frac{1}{2} \delta u - F_V \frac{a}{L} \delta u = (M_p + M_a) \phi \quad (3.5)$$

Yields with $\phi = \delta u/L$:

$$F_u = \left(\frac{1}{2} F_{SW} + \frac{a}{L} F_V \right) + \frac{M_p + M_a}{L} \quad (3.6)$$

A relative uplifting force F can be introduced to represent the uplifting force subtracted by the support reaction from the vertical force and the self-weight of the beam.

$$F = F_u - \frac{1}{2}F_{SW} - \frac{a}{L}F_V \quad (3.7)$$

By inserting eq. (3.7) into eq. (3.10) the relative uplifting force becomes:

$$F = \frac{M_p + M_a}{L} \quad (3.8)$$

3.2 Hinged connection

3.2.1 Axial loading situation

Axial and shear force in the connection determine the sliding behaviour of the considered connection. When relying on friction a Coulomb friction material model can be implemented to understand the sliding behaviour. This theory gives a relation between the normal stresses (σ_n) and the occurring shear stresses (τ) in the onset of motion in terms of the friction coefficient (μ). In the case of a concrete hinge with a cylindrical contact shape the normal stress distribution is of utmost importance. The created bending moment can be described as the integrated shear stress over the contact surface multiplied by the radius. The stress distribution of a connection loaded by a normal force is depicted below.

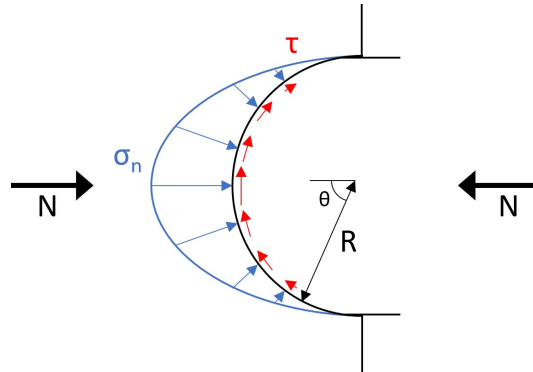


Figure 3.5: Assumed interface stress distribution under dominant axial force

$$M = d \int \tau R dS = d \int \tau R R d\theta \quad (3.9)$$

Yields with $\tau = \mu\sigma_n$:

$$M = d \int \mu\sigma_n R R d\theta = d\mu R^2 \int \sigma_n d\theta \quad (3.10)$$

The Hertzian theory for contact between two curved elastic bodies is introduced in section 2.3.1 with the following normal stress formulation:

$$\sigma_n = \frac{p(x)}{d} = \frac{P_0}{d} \sqrt{a^2 + x^2} \quad \text{with } P_0 = \frac{2N}{\pi a} \quad (3.11)$$

Where:

N = normal force originating from the horizontal soil pressure

P_0 = maximum Hertz pressure

d = depth of the connection surface

a = contact half width

x = coordinate perpendicular to the normal force

A simplification to this formula can be made by assuming complete half contact of the cylindrical surface with $a = R$. The contact coordinate can be transformed into polar coordinates with: $x = R \sin(\theta)$.

$$\sigma_n = \frac{2N}{d\pi R} \sqrt{1 - \sin^2(\theta)} \quad (3.12)$$

The formulation of the bending moment then becomes:

$$M = d\mu R^2 \int_{\theta_1}^{\theta_2} \sigma_n d\theta = \frac{2N}{\pi R} \left[\sqrt{\cos^2(\theta)} \tan(\theta) \right]_{\theta_1}^{\theta_2} \quad (3.13)$$

With $\theta_1 = -\frac{\pi}{2}$ and $\theta_2 = \frac{\pi}{2}$ to comply with the simplification of complete half contact of the cylindrical surface:

$$M = \mu R^2 \left(\frac{1}{R} N \frac{4}{\pi} \right) = \mu N f R \quad \text{with } f = \frac{4}{\pi} \quad (3.14)$$

Where the factor f can be described as the contact factor for this specific loading condition and boundary conditions. The contact factor describes the proportion of the total contact force distributed in normal direction to the applied normal force.

$$f = \frac{M}{\mu N R} = d \int \sigma_n \frac{R}{N} \quad (3.15)$$

3.2.2 General loading situations

The previously described stresses in the cylindrical connection are only valid for dominant axial loads. This situation can present itself in the tunnel structure at the lower floor levels. At this location, the soil pressure N (axial load) is at its maximum and relatively large compared to the traffic loads (crosswise load) for tunnels with large depths. The attribution of the shear force resulting from the crosswise loads can be implemented in the model by taking the resultant of this force and the axial force as Q .

$$N \rightarrow Q = \sqrt{N^2 + V^2} \quad (3.16)$$

In the symmetric loading situation the shear force can be formulated as $V = \frac{1}{2}(F_V + F_{SW})$ for the case described in fig. 3.3. Additionally, it is expected that the contact factor f is not

constant for different normal force to shear force combinations. Therefore, the contact factor is further specified:

$$f = f_0 = \frac{4}{\pi} \quad \text{for } N \gg V \quad (3.17)$$

$$f = f_V \quad \text{for } N \ll V \quad (3.18)$$

This results for the case of dominant normal force loading in:

$$M = \mu Q f_0 R \quad \text{for } N \gg V \quad (3.19)$$

By substitution eq. (3.19) in eq. (3.4) to obtain a formulation for the friction ratio:

$$\mu = \frac{FL}{2Q f_0 R} \quad (3.20)$$

For the case when the shear forces are larger in comparison to the axial forces, a different stress distribution is created.

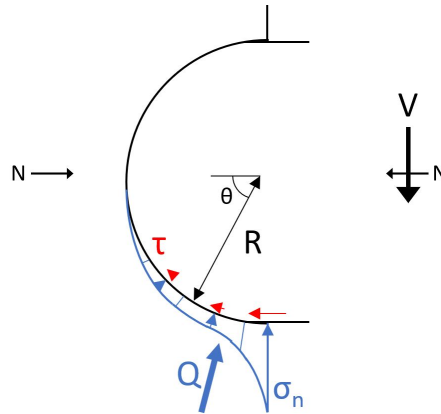


Figure 3.6: Assumed interface stress distribution under dominant shear force

The original formulation for the bending moment is still valid. However, the altered normal stress distribution results in a different contact factor. When analytical normal stress distributions for dominant shear force loading situations are not obtainable a finite analysis can be performed to obtain the contact factor (f_V).

$$M = \mu R^2 \int_{\theta_1}^{\theta_2} \sigma_n d\theta = \mu Q f_V R \quad \text{for } N < V \quad (3.21)$$

The loading situation described in fig. 3.6 and by eq. (3.8) (shifted vertical force) both connection loading variants occur in the mechanism. At the passive side, a shear force dominates the stress distribution and at the active side a dominant normal force. Bending moments at the connections from the uplifting force are no longer identical. By assuming these different bending moments as follows eq. (3.8) can be evaluated further.

$$M_p = \mu Q_p f_V R \quad \text{for } N \ll V_i \quad (3.22)$$

$$M_a = \mu Q_a f_0 R \quad \text{for } N \gg V_i \quad (3.23)$$

Where:

$$Q_p = \sqrt{N^2 + V_p^2} \quad \text{and} \quad Q_a = \sqrt{N^2 + V_a^2} \quad (3.24)$$

By substituting eq. (3.22) and eq. (3.23) in eq. (3.8) the following formulation for the bending moment on the connection at the passive side is valid:

$$M_p = \frac{FLQ_p f_V}{Q_p f_V + Q_a f_0} \quad (3.25)$$

With this solution the friction ratio can be formulated as:

$$\mu = \frac{FL}{(Q_p f_V + Q_a f_0)R} \quad (3.26)$$

It is clear that for $Q_p = Q_a$ and thus $f_V = f_0$ eq. (3.26) reduces to eq. (3.20).

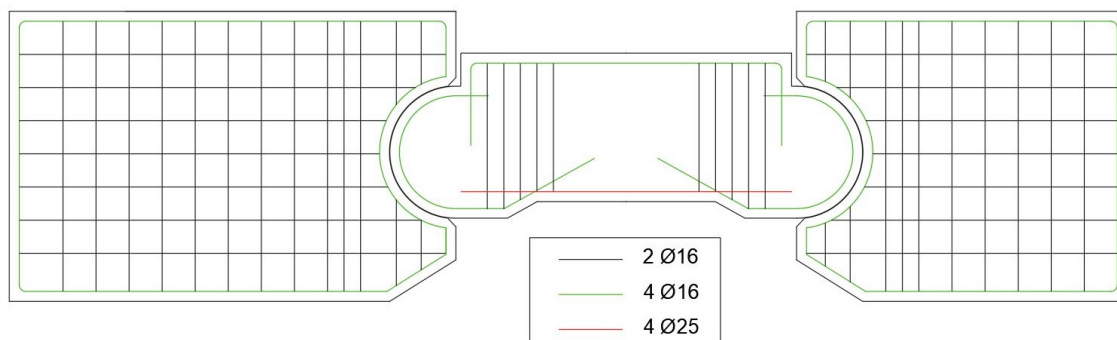


Figure 4.2: Simplified rebar design

The concrete elements are equipped with two different type of sliding bearings:

- Eshastick - concrete (see fig. 4.3b and fig. 4.3a)
The concave part of the mother elements are equipped with a layer of Eshastick: a bitumen covered glass fiber fabric. The layer has a thickness of 1.5 mm and has a rough surface finish.
The convex part of the father element is smooth concrete left untreated after de-moulding.
- PTFE - stainless steel (see fig. 4.3c and fig. 4.3d)
A sheet of 1.5 mm PTFE is bonded to the concrete concave surface of the mother elements after hardening of the concrete.
A stainless steel (SST) sheet is casted into the convex surface of the father element.

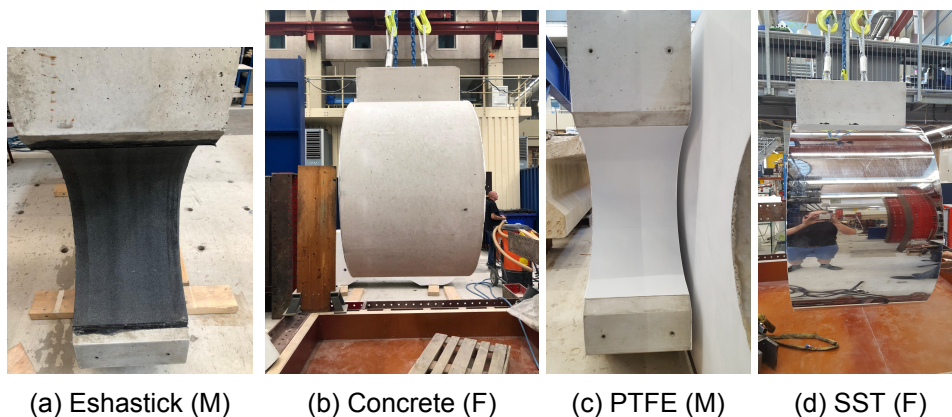


Figure 4.3: Interface variants

4.2 Test plan

A distinction is made between the floor and roof test. The floor test represents a floor level at the bottom of the tunnel. At this location horizontal soil forces are high compared to the vertical forces resulting from traffic loads. This test is named "dominant normal force". The roof test is set up with a relative low normal force compared to the large vertical force corresponding with the tunnel roof. The roof is the part of the tunnel with the lowest horizontal soil pressure combined with a large top load from the overburden with the associated vertical loads. This test is named "dominant shear force".

4.2.1 Test setup

The concrete elements are placed in a test setup composed out of steel members. The frame is made as stiff as possible by locally strengthening the steel sections. Vertical prestress is applied to the specimens by means of external post-tensioned tendons. Pre-stress is applied to achieve a certain concrete stress during the test and to ensure the vertically fixed rigid boundary conditions for the passive mother element. The test setups with loads of interest are depicted in fig. 4.4 and fig. 4.5 recreating the loading conditions previously described.

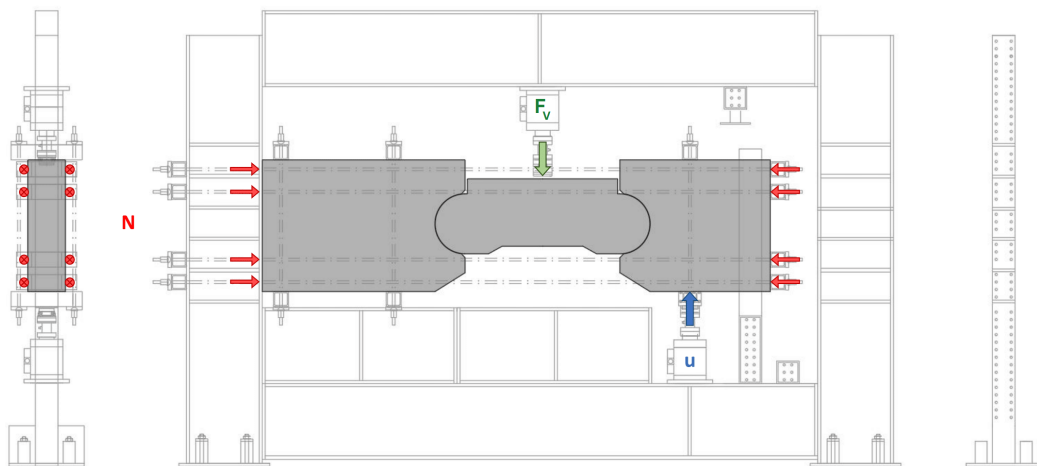


Figure 4.4: Testing setup "dominant normal force"

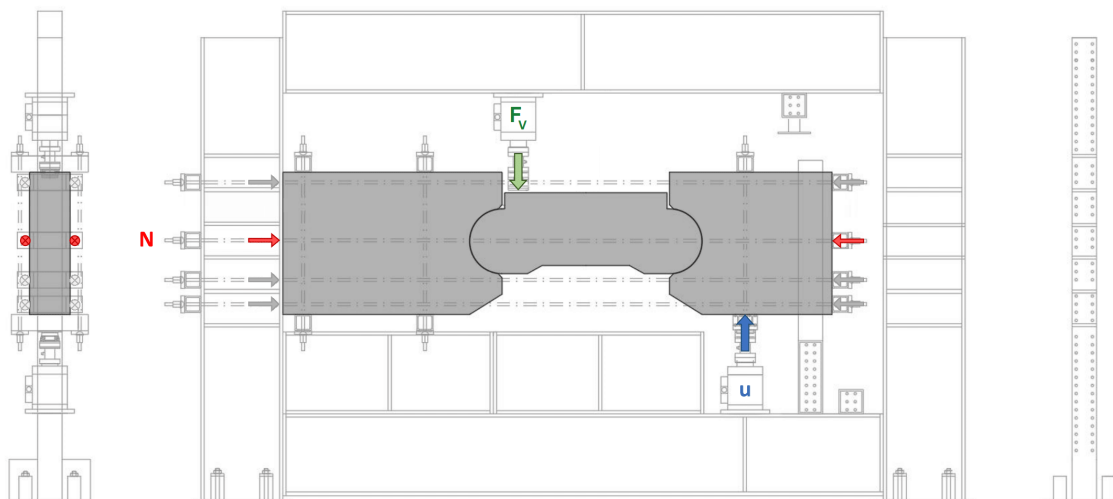


Figure 4.5: Testing setup "dominant shear force"

The passive mother element is supported by a vertical jack which is displacement controlled (u). This concrete element is supported by a hinge on the jack, ensuring free rotation. A horizontal post-tensioning system is applied to create the varying normal force in the system (N). The system is composed out of eight external post-tensioning tendons (Y1050H 32R) connected to the test frame and the active mother elements with stiff steel tubes and end-plates. The prestressing force is applied alternately in stages. The prestress distribution over the eight tendons is unrestricted as long as an equilibrium is created. To achieve the dominant vertical load situation, solely prestress is applied to the central tendons. The remaining tendons are in place to restrict unwanted rotations. A vertical load (F_V) can be applied with the top jack located on the father element. This jack is operated with load control. Different load combinations can be created within the limits of the testing setup. The location of the top jack over the father element can be adapted. For the dominant normal force situation, a centrally position is required. The top jack is placed more to the edge of the father element to achieve the desired high shear force.

4.2.2 Measurement plan

The performance of the connection is to be measured with the aid of several different sensors. The behaviour of the connection is of interest during operational loads. Relative rotations and displacements of the elements in combination with the applied load magnitudes are investigated to obtain a good insight in the sliding behaviour. The restricted rotation caused by the friction in the interface is measured indirectly with the applied sensors. The force in the external tendons is measured to obtain the correct magnitude of normal force for a certain loading combination. Additionally, the differential tendon forces are measured during the loading of the specimens. The limit state is determined by monitoring potential failure mechanisms. The interface is monitored, as mentioned before, with the focus on internal failure of the bearing material. When the tensile capacity of the concrete is approached cracks are formed at critical locations. From the prevailing contact theories reviewed in chapter section 2.3 it is observed that the apex of the concave is a region where the tensile stresses reach their maximum. For this reason the strain is measured in this region.

Overview of the applied sensors:

- LVDT - Linear Variable Differential Transformer
LVDT's can measure relative displacement between two points. These sensors are used to obtain element displacements and rotations. Crack widths can be measured when they are formed in between the measurement points.
- SG - Strain Gauge
All eight post-tensioning tendons are equipped with strain gauges. The stiffness of the steel is investigated with tensile tests where samples are pulled to failure. The tendon force with the corresponding normal force can be derived from this stiffness with the measured strain.
- DIC - Digital Image Correlation
The strains of a surface can be measured with the DIC measurement system. A camera registers images of a specially prepared surface with a stochastic pattern. Post-processing software is used to correlate and track the measured data. Full field displacements can be derived with the system to validate the displacements measured with the LVDT technique. Crack widths of the concrete can be measured to investigate the limit state of the connection.

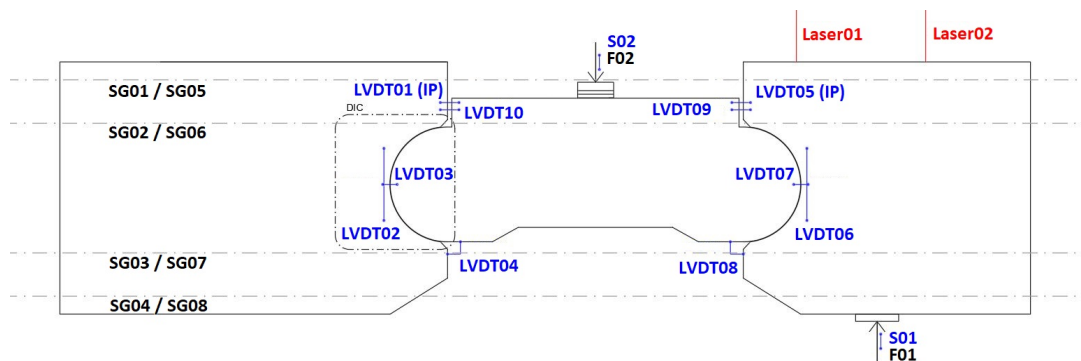


Figure 4.6: Measurement plan "dominant normal force"

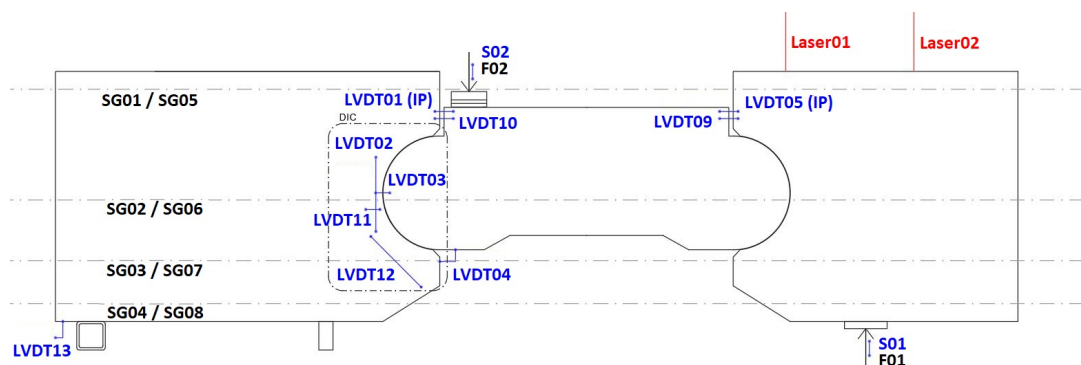


Figure 4.7: Measurement plan "dominant shear force"

The data from the LVDT's (LVDT & S), strain gauges (SG) and the jack load sensors (F) are amplified and collected by a central computer. These measurements are displayed in real-time during testing. The DIC system is manually operated during the experiment and the obtained image collection is processed after the completion of the test.

4.2.3 Load plan

The client proposed a load plan to test the behaviour of the connection with a SLS test and the limit state with a ULS test. The loading program with the magnitudes of the loads is displayed in table 4.1. The general loading procedure is to start with loading of the normal force. This force is reached in stages by alternately tensioning the external tendons. When the required normal force is introduced in the system a vertical load is applied by the top jack with a predetermined loading speed. The displacement controlled jack, supporting the passive mother element, is in its neutral position during the application of the vertical load. This jack will take over when the desired vertical force is reached and displace the passive mother element upward along a predetermined loading path with a lifting speed of 0.004 mm/s. This is prescribed by the client to be sufficiently slow to resemble the actual load. The order of loading ensures that a normal force is always present before subsequent loading is present, as is the case during the life-time of the structure. A certain normal force is required for the connection before large shear loads are introduced to prevent excessive interface opening.

Table 4.1: Loading program

Load combination		N (kN)	F_V (kN)	u (kN)
a-0 : dominant N	SLS	2000	200	30
	ULS	3000	300	0
b-0 : dominant F_V	SLS	200	600	30
	ULS	300	900	10
a-1 : dominant N	SLS	2150	400	30
	ULS	3250	600	30
b-1 : dominant F_V	SLS	200	775	30
	ULS	200	1050	30
c : max Q	final	200	max	0

An overview of the testing program is shown in table 4.2. Every test starts with the SLS load combination. The vertical loads are reset to its neutral level before the ULS test follows. The normal force is increased from the previous load combination value to the required magnitude. This procedure is repeated for the case of the limit load.

Table 4.2: Testing program

Test	specimen set	Type	Interface material	Load combinations
0	A	Trial test	Eshastick	a-0
1	B	Trial test	Eshastick	b-0
2	C	Main test	Eshastick	a-1, b-1 and c
3	D	Main test	PTFE-SS	a-1, b-1 and c
4	E	Repeat test	Eshastick	a-1, b-1 and c
5	F	Repeat test	PTFE-SS	a-1, b-1 and c

5 Finite element analysis

Different finite elements model (FEM) variants are created to support the testing project. A simplified model is created to investigate the contact mechanics of the cylindrical concrete connection. Variations in interface properties will be investigated. Extending from this a model is made based on the actual test setup. A two-dimensional model is created to investigate the structural behaviour of the setup. All sliding hinge connections have identical dimensions in this analysis.

5.1 Cylindrical connection models

Two models are created to investigate the behaviour of a sliding hinge connection for different loading conditions. Firstly, a model is set up to investigate an axially loaded connection. Besides the distribution of various stresses along the interface, the effect of clearance is investigated. Secondly, more complex loading situations, such as axial-shear force combinations with rotational loads are investigated with a second cylindrical connection model. With this model the contact parameter for a connection loaded dominantly in shear is obtained.

5.1.1 Simplified cylindrical connection model

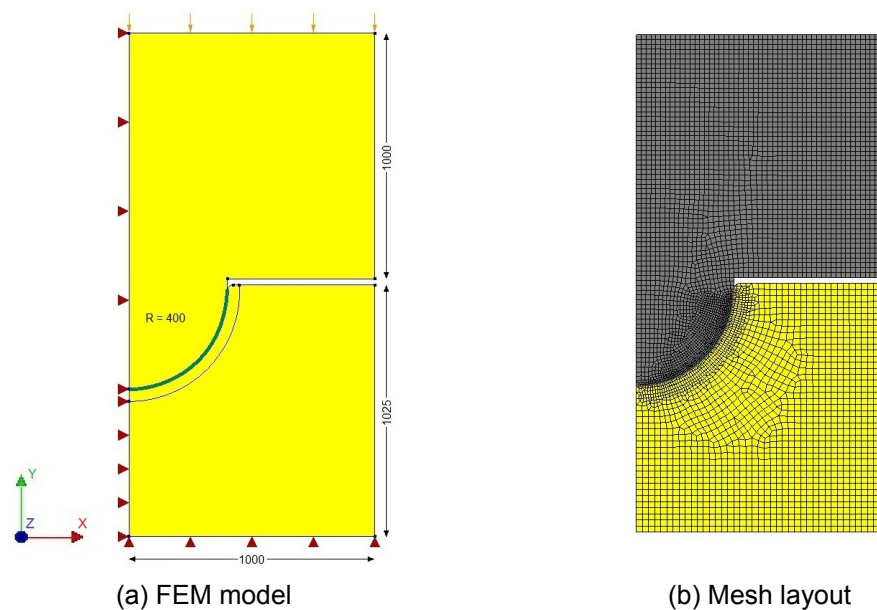


Figure 5.1: Simplified cylindrical connection model

The geometry of the simplified cylindrical connection model is simplified by means of symmetry boundary conditions. Displacement in X-direction (and therefore also the rotation around the Z-axis) is prevented on the left edge of the modelled connection to conform to the symmetry conditions. The radius of the cylindrical interface is set at 400 mm to resemble the dimensions in the testing project. This is also the case for the 500 mm thickness of all elements. An interface is created between the concave bottom part and the convex top part along the cylindrical edge. The top edge of the top element is loaded by line load of 1000 N/mm denominated as N/2.

Table 5.1: Model parts

Parts	Color code	Element type		Element size
Concrete specimens	yellow	CQ16M, CT12M	plain stress	30 mm (*10 mm)
Support interface	green	CL12I	structural interface	10 mm

* Mesh refinement is applied along the edge of the interface to obtain more accuracy on this area of interest.

5.1.2 Full cylindrical connection model

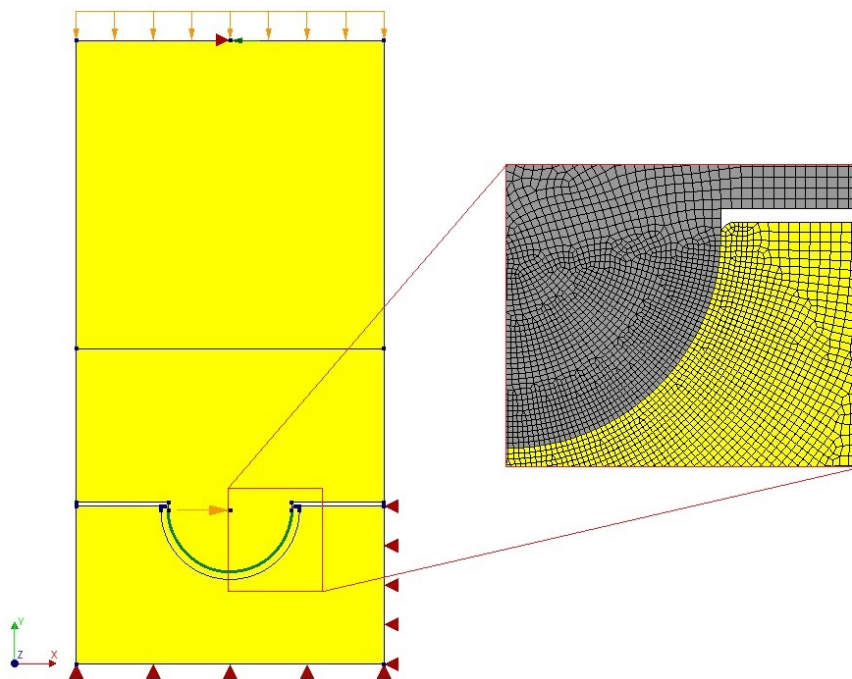


Figure 5.2: Full cylindrical connection model FEM model and mesh

The simplified cylindrical connection model is expanded to allow more complex loading situations. Symmetry conditions are removed to obtain the behaviour of the full cylindrical interface. The top concrete part is extended and supported at the end to allow for a prescribed deformation causing rotation in the connection. Besides the line load on top representing the axial force, a point load in X-direction is applied to the connection. This loads the connection in shear. Different combinations of axial and shear force are introduced into the connection to investigate stress distribution at rest and during rotation. A Coulomb friction interface is used in this model. With the absence of clearance, a conforming contact is achieved in this model. This interface does not have any tensile capacity and will have a limited shear capacity dependent on the normal stress and the friction ratio. By varying the axial and shear force ratio different stress distributions will become apparent. The contact factor described in section 3.2 can be validated and extended to more loading situations.

5.1.3 Parameters

Table 5.2: Material properties concrete

Element type	CQ16M, CT12M	
Thickness	500	mm
Linear elastic		
Young's modulus E	33000	N/mm^2
Poisson's ratio ν	0.2	
Mass		
Mass density	$2.4 \cdot 10^{-9}$	T/mm^3

Table 5.3: Coulomb friction interface

Element type	CL12I	
Thickness	500	mm
Linear properties		
Normal stiffness k_n	1000	N/mm^3
Shear stiffness k_t	1	N/mm^3
Coulomb friction		
Cohesion	10^{-15}	
Friction angle	1.72	deg
Interface opening		
Model	Gapping	
Tensile strength	0.01	N/mm^2
Shear mode II	brittle	

* friction angle of 1.718 degrees represents a friction ratio of 3 %. This friction parameter is chosen to be relatively low to achieve the friction limit condition over the complete interface with minimal imposed rotation.

5.1.4 Results

Two models are created to investigate the stress distributions in the connection for different loading situations.

Stress distribution at rest for an axial load

The stresses to be evaluated are located at the edge of the concave mother element of the sliding hinge connection. fig. 5.3 shows the considered stress tensors and their directions for a specific concrete element along the interface. The model displaying solely the cylindrical connection is loaded in the Y-direction with $N = 2000$ kN. This together with the dimensions of the connection result in the stresses over the contact angle as presented in fig. 5.4

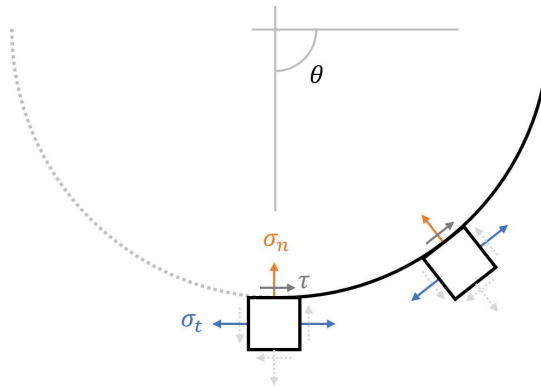


Figure 5.3: Clarification contact stresses

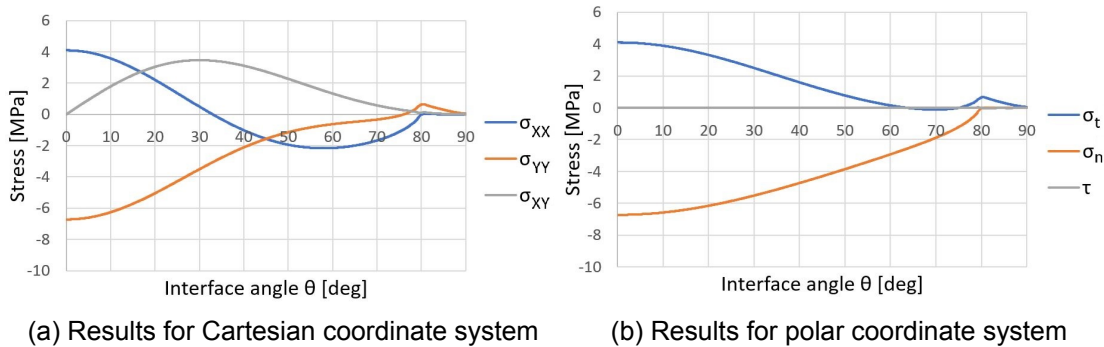


Figure 5.4: Stress distribution mother element along the interface

The graphs of stresses converted to the polar coordinate system show compressive stresses in radial/normal direction and tensile stresses in the tangential direction. The extreme stress magnitudes are located at the base of the connection. The shear stresses (τ) over the contact line are zero as can be expected by the low dummy shear stiffness of the interface. According to the analytical formulations of the contact stresses a further generalisation can be made to the stress distributions by multiplying the stresses by the element thickness and dividing by the applied axial force:

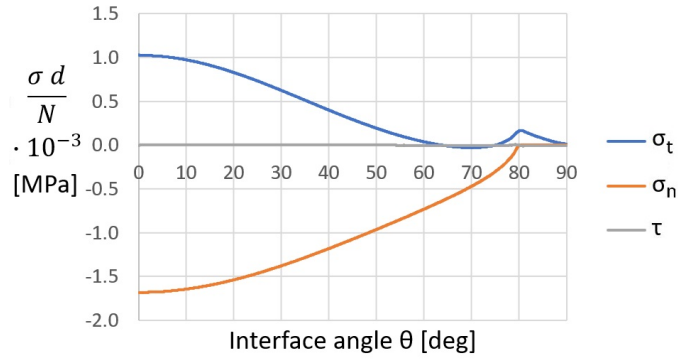


Figure 5.5: Generalised stress distribution mother element along interface

Clearance effect for an axial load

The clearance (dR) is the difference in radius between the radius of the convex (R_1) and the radius of the concave (R_2) cylindrical elements: $dR = R_2 - R_1$. Effects of this clearance to the normal stress distribution is investigated. Interface properties are adjusted to obtain a certain clearance as a relative displacement limit at which significant normal stiffness is present. Different clearances are implemented in the no-tension interface non-linear elastic relative displacement-traction diagrams:

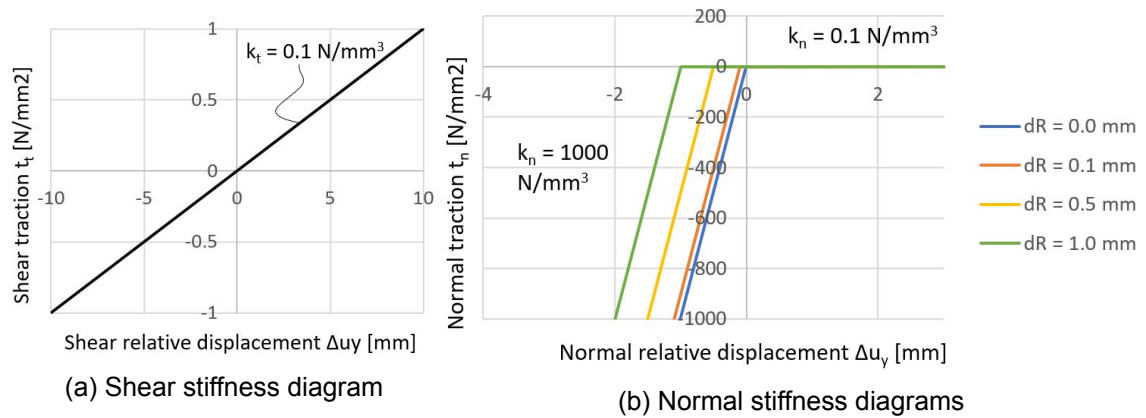


Figure 5.6: No-tension interface stiffness

The generalised normal stress distribution over the contact surface for the different clearances is presented in fig. 5.7. As can be seen from the obtained results, linear interface properties show a peak stress at the ends ($\theta = 90^\circ$) of the connection. This can be explained by tensile stresses at the end of the interface due to the inability of a linear analysis to create a no-tension interface. Further analysis has been performed with non-linear interface properties where no tensile stresses are allowed and a certain clearance can be implemented. The normal stress distribution changes significantly when relatively small clearances are modelled. For clearances over 0.1 mm a clear increase in maximum stress at the base is visible.

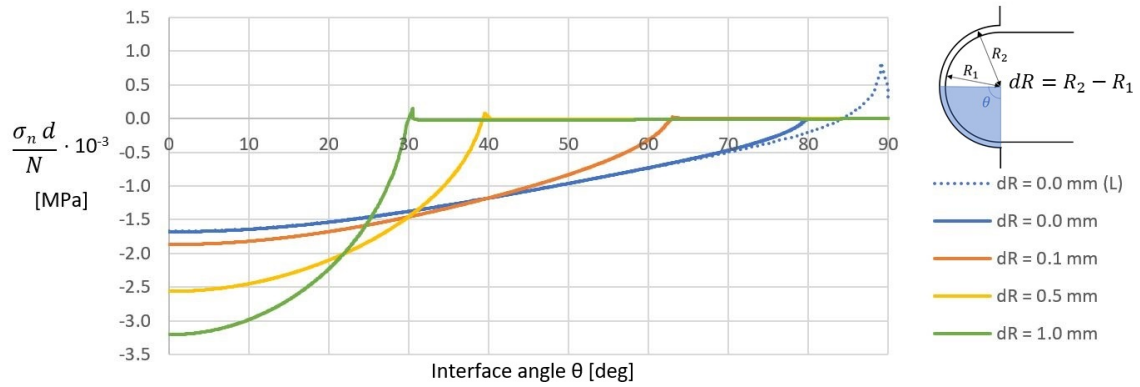


Figure 5.7: Generalised normal stresses for different clearances

The contact factor can be determined based on the bending moment in the connection. In eq. (3.15) it is clear that the contact factor depends only on the normal stress distribution scaled by the contact force and the radius. Therefore, the contact factor for different clearances can be obtained for different clearances. In this case the radius R in eq. (3.15) is taken as the radius of the mother element R_2 .

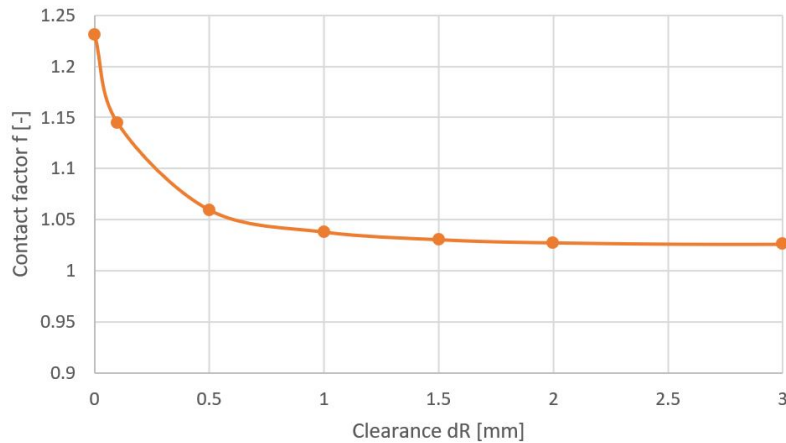


Figure 5.8: Contact factor for different clearances

It is observed from fig. 5.8 that the contact factor f for conforming contact ($dR = 0$) is approximately $\frac{\pi}{4} \approx 1.25$. The contact factor tends to converge to 1.0 for larger clearances. This effect is made clear by fig. 5.9 where the normal stresses are almost fully in the direction of the normal force load. The stiffness of the mother and father elements are expected to influence the contact factor. With more deformable elements the contact factor is expected to converge slower to 1.0 when increasing the clearance.

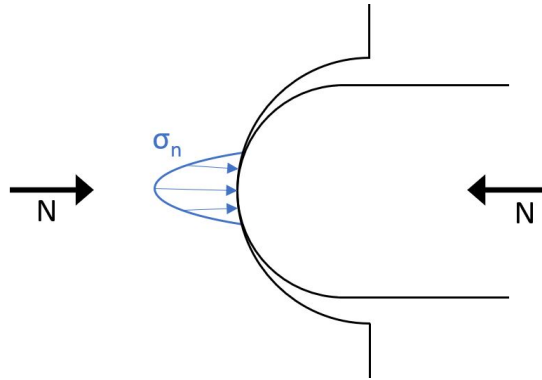


Figure 5.9: Normal stress distribution for substantial clearances

Stress distribution in motion for different loading combinations without clearance

The full cylindrical connection model is loaded with different axial / shear force combinations (not generalised). The normal stress distribution is depicted below. The Coulomb friction interface will ensure a shear stress distribution based on the normal stress distribution scaled by the friction ratio with sufficient rotation. The rotation initiated by the imposed deformation of the top support in X-direction must be of significant magnitude to allow for these limiting shear stresses. A conforming contact (without clearance) is assigned to the interface.

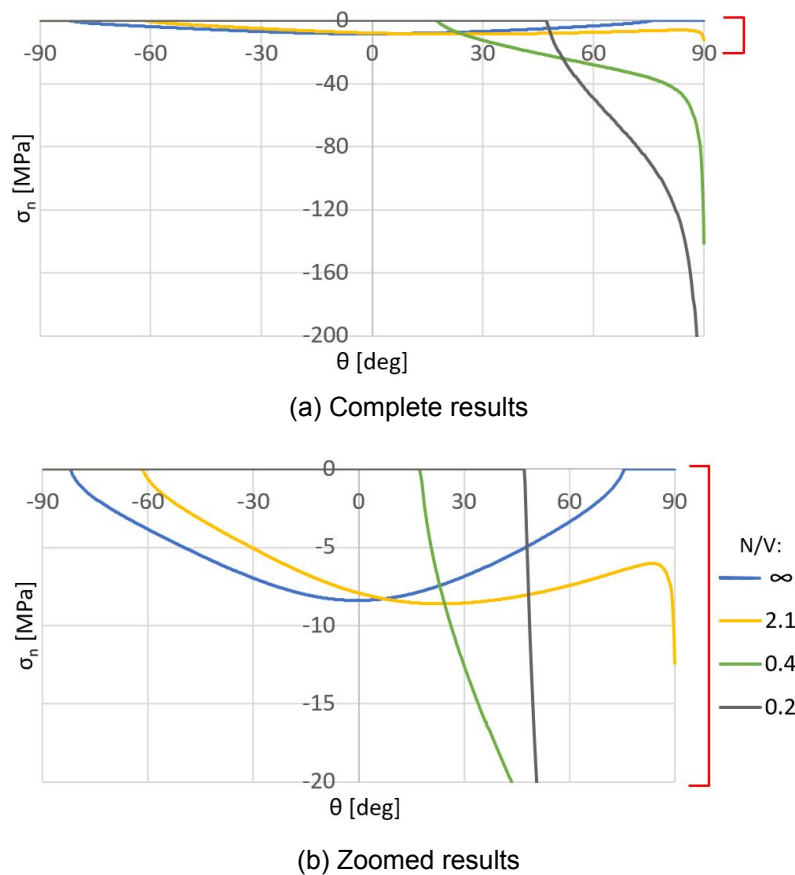


Figure 5.10: Normal stress distribution for different N/V

The contact factor is determined for different N/V ratios is calculated with eq. (3.15) and displayed in the graph below. The N/V ratio is presented in logarithmic scale to cover most of the load combinations.

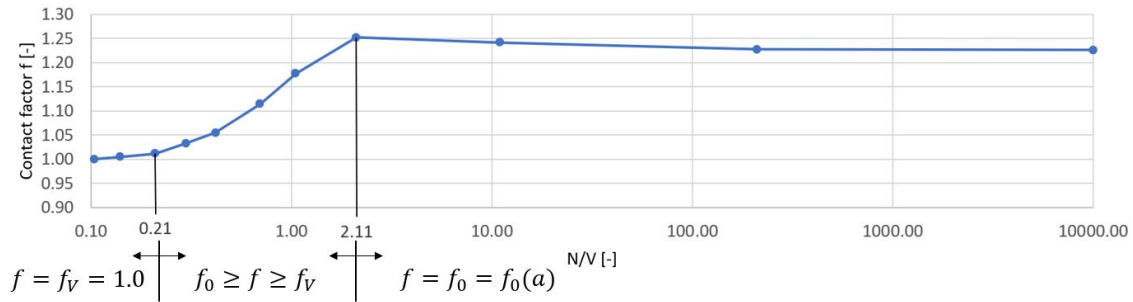


Figure 5.11: Contact factor for different N/V

It is expected that the contact factor is also influenced by the normal stiffness of the interface. To verify this the analysis is repeated with a normal stiffness k_n of 10 times lower (100 N/mm^3). The effect of this parameter is observed to be limited as can be seen in fig. 5.12. It is apparent that for N/V ratios smaller than 0.2 the contact factor can be taken as 1.0. For N/V ratios larger than 2.0 a contact factor calculated according to the method described in section 3.2.1 is admissible resulting in a value of approximately 1.25. For load combinations in between these limits a power series can be formulated to describe the observed behaviour of the finite element results, as in eq. (5.1).

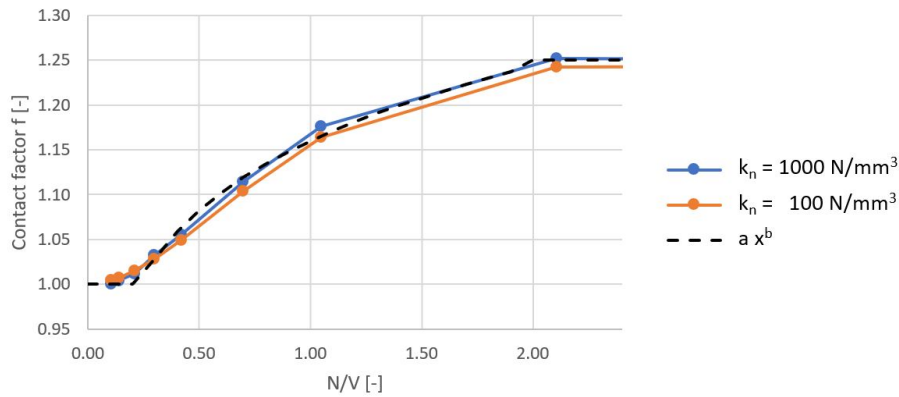


Figure 5.12: Contact factor

$$f = a(N/V)^b \text{ for } 2.0 \geq N/V \geq 0.2 \quad (5.1)$$

Where $a = 1.16$ and $b = 0.1$. Only valid for $dR = 0$ (no clearance).

5.2 Test setup models

A finite element model is setup containing all the relevant parts of the test setup. The goal is to achieve realistic connection behaviour and to have the ability to extend from the test project. Loads or properties can be adjusted to obtain the limit of the considered connection. A interface in conforming contact is implemented by the assumption that the interface material assures full contact and no clearance.

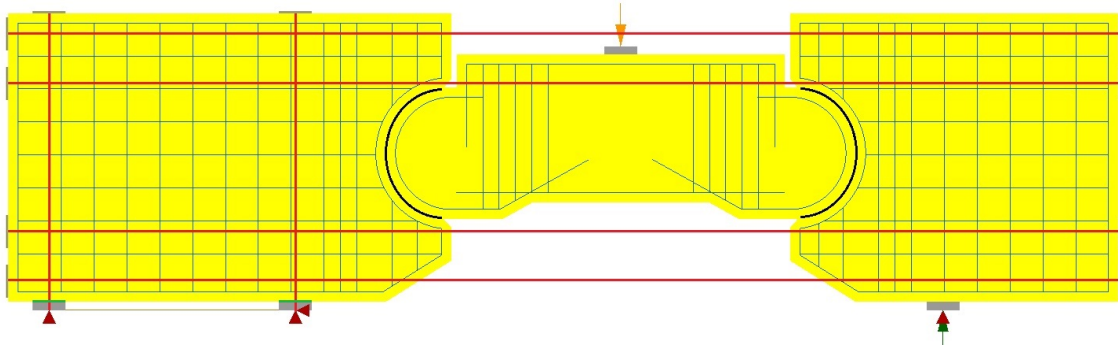


Figure 5.13: FE model "dominant normal force"

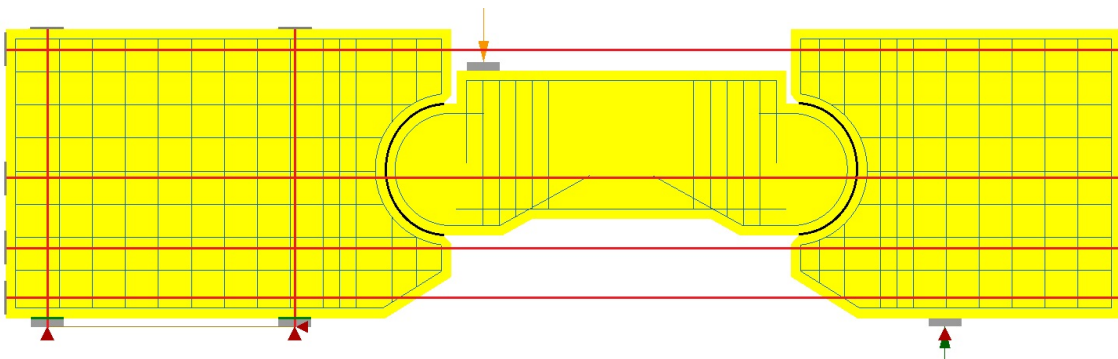


Figure 5.14: FE model "dominant shear force"

The model consist out of several parts modelled separately. These parts are visible in fig. 5.13 and fig. 5.14 with different colors. Each part represents an element of the actual test setup (see table 5.4) and has a different function. The location of the top load and the pre-stressed tendon layout can be varied to match the performed test in the laboratory.

Table 5.4: Model parts

Parts	Color code	Element type	
Concrete specimens	yellow	CQ16M, CT12M	plain stress
rebars	blue	*	embedded reinforcement
Support plates	grey	CQ16M, CL9BE	plain stress and beam
Pre-stress tendons	red	L2TRU	regular truss
Slide bearing interface	black	CL12I	structural interface
Support interface	green	CL12I	structural interface

Three main loads are included in the model. Each load is implemented with care to match the actual situation in practice. The loads are set out below:

- Horizontal pre-stressing of the tendons
- Downward load on top of the father element (force control)
- Upward load at bottom of active mother element (displacement control)

The magnitude of the applied loads is identical to the main and repeat laboratory tests with load combination a-1 for dominant normal force tests and load combination b-1 for dominant shear force tests. The elements are meshed to an element size of 25 mm for all plain stress elements. The mesh is refined at the sliding interface to an element size of 10 mm to capture an accurate stress and displacement field over this interface. A detail of the mesh layout is presented in fig. 5.15.

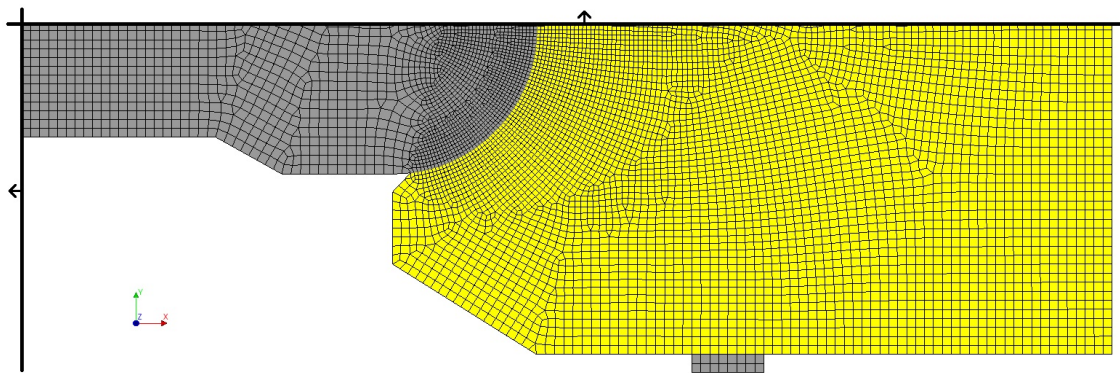


Figure 5.15: Mesh layout

5.2.1 Parameters

Structural elements

The model consists out of different parts with varying tasks and accompanying properties. A division is made between structural elements and interface elements. The structural elements are all voluminous parts where stresses are spread and/or transferred to adjacent elements or supports. The structural elements are initially modelled with linear material properties. These properties are based on material tests when these are available. Relevant properties, such as the concrete Young's modulus and the varies mass densities, are estimated when no material data is available.

Table 5.5: Material properties structural elements

Part	Concrete specimens	Steel tendons	Steel plates
Element type	CQ16M, CT12M	L2TRU	CQ16M
Thickness/diameter	500	2x32	500 <i>mm</i>
Linear elastic			
Young's modulus E	33000	210000	210000 N/mm^2
Poisson's ratio ν	0.2	0.3	0.3
Mass			
Mass density	$2.4 \cdot 10^{-9}$	$7.9 \cdot 10^{-9}$	$7.9 \cdot 10^{-9}$ T/mm^3

Interfaces

Several interfaces are present in the model. The passive mother element is supported with non-linear no-tension interfaces between the supporting plates and the concrete specimen. The interface properties are presented in table 5.6a. The properties are chosen to behave as stiff support in normal compression with low shear stiffness. However, in tension load a no tension behaviour is achieved by reducing the stiffness in all direction to a negligible magnitude. A Coulomb friction interface is applied between the father element and both mother elements. Besides choosing suitable normal and shear stiffness properties a relation for a shear stress limit depending on the normal stress is inputted in table 5.6b.

Table 5.6: Interface properties

(a) No-tension interface			(b) Coulomb friction interface		
Element type	CL12I		Element type	CL12I	
Thickness	500	mm	Thickness	500	mm
For compression			Linear properties		
Normal stiffness k_y	1000	N/mm^3	Normal stiffness k_n	100	N/mm^3
Shear stiffness k_x	1	N/mm^3	Shear stiffness k_t	var.	N/mm^3
For tension			Coulomb friction		
Critical interface opening	10^{-5}	mm	Cohesion	10^{-15}	
Stiffness reduction factor	10^{-6}		Friction angle	var.	rad
			Interface opening		
			Model	Gapping	
			Tensile strength	0.01	N/mm^2
			Shear mode II	brittle	

The different interface materials are implemented by varying the shear stiffness k_x and the friction angle. The results from the small scale Eshastick interface test are used to obtain the sliding stiffness. By neglecting any effect of limitations set by the shear capacity, the sliding stiffness for a bituminous interface is as determined in section 2.2 to be $0.33 N/mm^3$. The more stiff and higher friction interface representing a PTFE-SST interface is not tested in the small-scale tests. The sliding stiffness of this interface is obtained by fitting the uplifting force - rotation results for a heave load with the actual test results (see fig. 6.3). A sliding stiffness of $1.50 N/mm^3$ shows similar rotational stiffness for the case when both interfaces are rotating during the heave load (rotations > 0.001 rad). The approximate normal stiffness and expected friction angles are obtained from the laboratory test results described in chapter 6. Normal displacements in the sliding interface are simplified to be 0.1 mm for a normal force of dominant normal force ULS level ($N = 3250kN \rightarrow k_n = \sigma_n/0.1mm = 10/0.1 = 100 N/mm^3$). For a complete overview of the relevant interface properties see table 5.7.

Table 5.7: Interface variations

Interface material	Normal stiffness k_n [N/mm ³]	Sliding stiffness k_t [N/mm ³]	Friction angle μ [deg]
IF 1 (Eshastick)	100	0.33	0.86 (1.5%)
IF 2 (PTFE-SST)	100	1.50	2.86 (5.0%)

5.2.2 Results

All main load combinations, as mentioned in the previous chapter, are applied to the model and analysed with a phased structural non-linear calculation. First the normal force is applied, followed by the vertical force and finally the uplift of the active mother element. Rotations are observed between the concrete parts over the interfaces when substantial loads are applied. These rotations are linked to tangential displacements resulting in interface shear stresses (or tractions). The shear traction integrated over the interface surface multiplied by the cylindrical interface radius gives the bending moment present in the concrete hinge (as in eq. (5.2))

$$M = \int_{\theta_1}^{\theta_2} \tau R d\theta \quad (5.2)$$

The normal and tangential stress distribution in the interface loaded with dominant normal force is given in fig. 5.16 and fig. 5.17. The situation for the connection subjected to the full vertical load (V+N) and of the full heave load (N+V+u) is set out. A overview of the relevant internal and external forces is given in table 5.8.

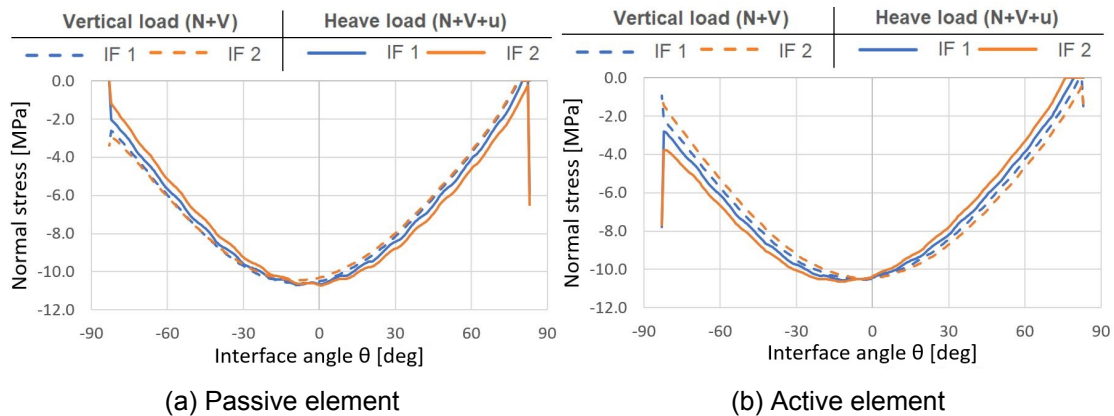


Figure 5.16: Normal stresses - LC: dominant normal force

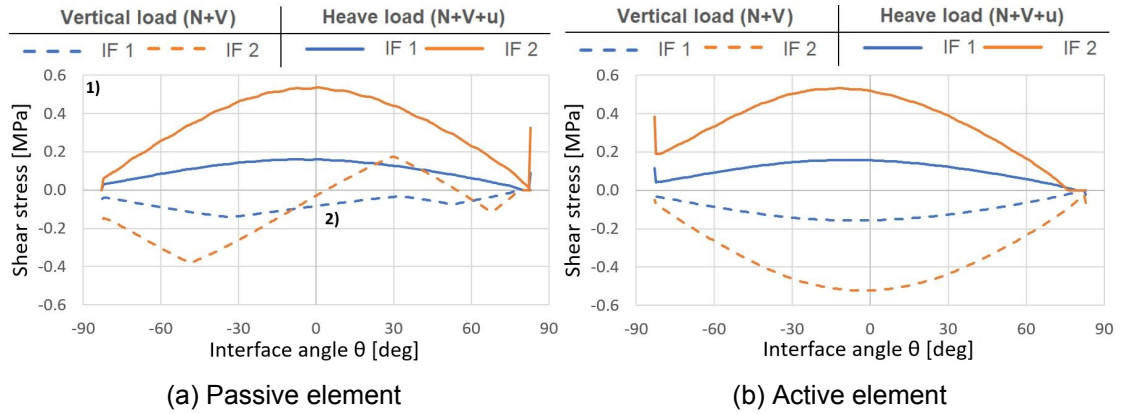


Figure 5.17: Shear stresses - LC: dominant normal force

The stage where the shear load is added as a load is presented in the dashed lines. This load phase is of importance as can be observed from the substantial shear stresses. The interface with IF-1 properties shows smaller shear stresses as the IF-2 interface (note 1 in fig. 5.17a). This is because of the larger friction angle for IF-2, causing higher stresses for identical displacements. The parabolic shear stress distribution at the active side resembles the distribution of the normal stresses because the friction angle limit is reached. Note 2 in fig. 5.17a highlights distinctive stress distribution behaviour. At this location in the interface the shear displacement is too small to achieve the friction angle limit or the normal stress is sufficiently small to allow for the linear material property to be valid. This behaviour is described by the condition described in eq. (5.3). The bending moment after the shear loading phase is observed to be 70 % and 30% of the maximum bending moment possible by reaching the friction angle limit for the IF-1 and IF-2 interface model respectively.

$$\Delta u_t k_t > \mu \sigma_n \quad (5.3)$$

An overview of the results for the model loaded with dominant normal force is given in table 5.8.

Table 5.8: Results - LC: dominant normal force

	IF-1	IF-2	
μ	1.5	5.0	%
F	43.8	128.9	kN
$M_{p;V}$	17.2	22.6	kNm
$M_{a;V}$	24.4	81.1	kNm
M_p	24.3	81.1	kNm
M_a	24.4	81.2	kNm
μ^*	2.8	8.2	%

Note: All bending moments are acting in the direction as displayed in fig. 5.20 and fig. 5.21.

The results show the magnitude of the bending moments present during the shear loading phase. This results in the difference in the input friction ratio (μ) and the friction ratio calculated according to the analytical method (μ^*) as described in chapter 3.

An overview of the results for the model loaded with dominant shear force is given in fig. 5.18, fig. 5.19 and table 5.9.

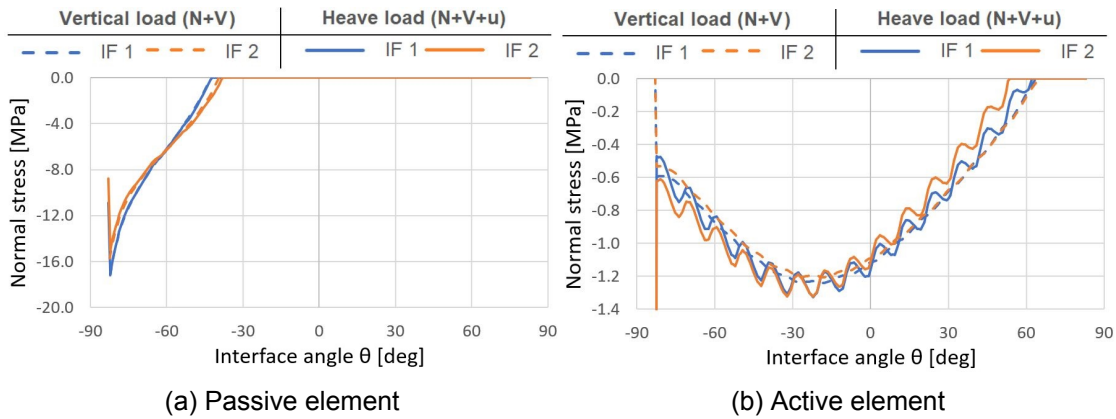


Figure 5.18: Normal stresses - LC: dominant shear force

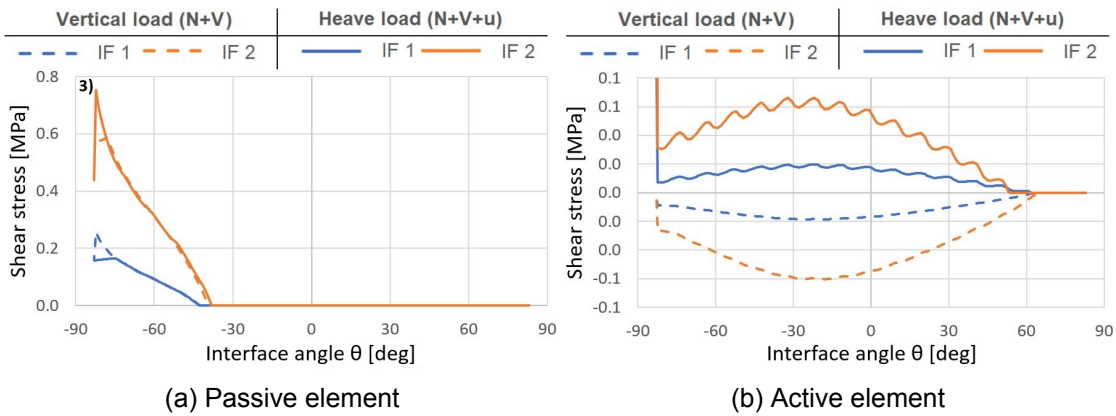


Figure 5.19: Shear stresses - LC: dominant shear force

Table 5.9: Results - LC: dominant shear force

	IF-1	IF-2	
μ	1.5	5.0	%
F	2.8	8.6	kN
$M_{p;V}$	5.7	19.9	kNm
$M_{a;V}$	2.6	8.4	kNm
M_p	6.2	20.5	kNm
M_a	2.6	8.4	kNm
μ^*	1.0	3.1	%

The graphs presenting the normal force distribution for this dominant shear force combinations show a clear shear force transfer peak at the bottom part of the contact surface ($\theta < -40$ deg) of the interface at the passive element. At the active element side, a shift of the resultant contact force is visible, giving rise to a specific contact factor. The wavy

behaviour of the stress distribution during the heave phase at the active mother element is caused by the analysis equilibrium iteration method. More load steps would smoothen the results but would also increase the computation time. fig. 5.19a shows the shear stresses originating from shear displacements on the passive element interface. Note 3 in fig. 5.19a shows for the (dashed) shear force application phase the shear stress caused by the displacement concerning the opening of the interface. This behaviour is unique to the dominant shear force tests. The mismatch between the analytically determined friction ratio and the input friction ratio shows a big underestimation by disregarding the bending moment present after the shear loading phase.

To restore the compatibility of the analytical derivation of the friction ratio, the bending moment generated from the vertical load needs to be taken into account. The motion of the elements relative to each other is displayed in fig. 5.20 and fig. 5.21 in a simplified manner.

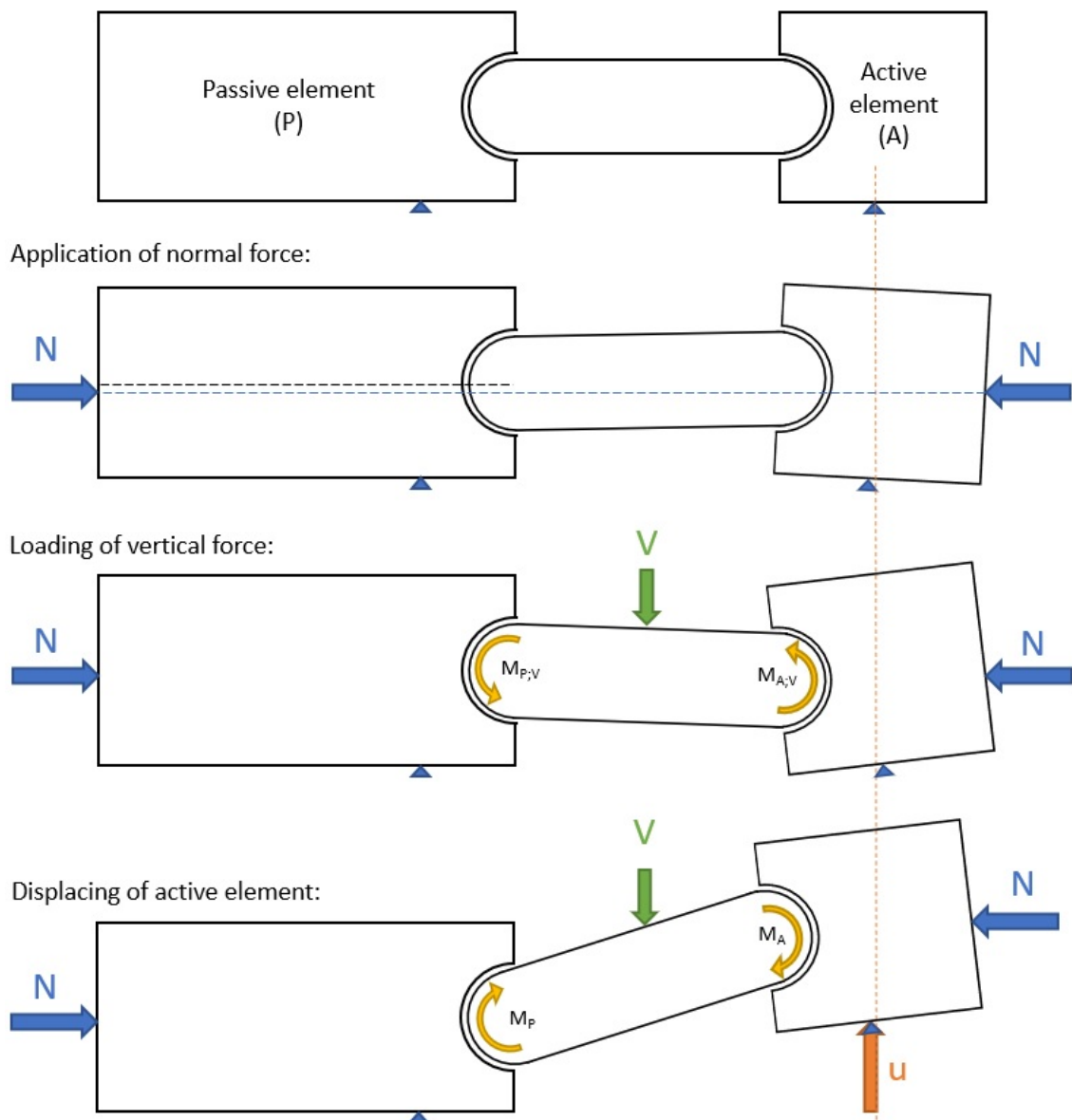


Figure 5.20: Element behaviour during different loading stages - dominant normal force

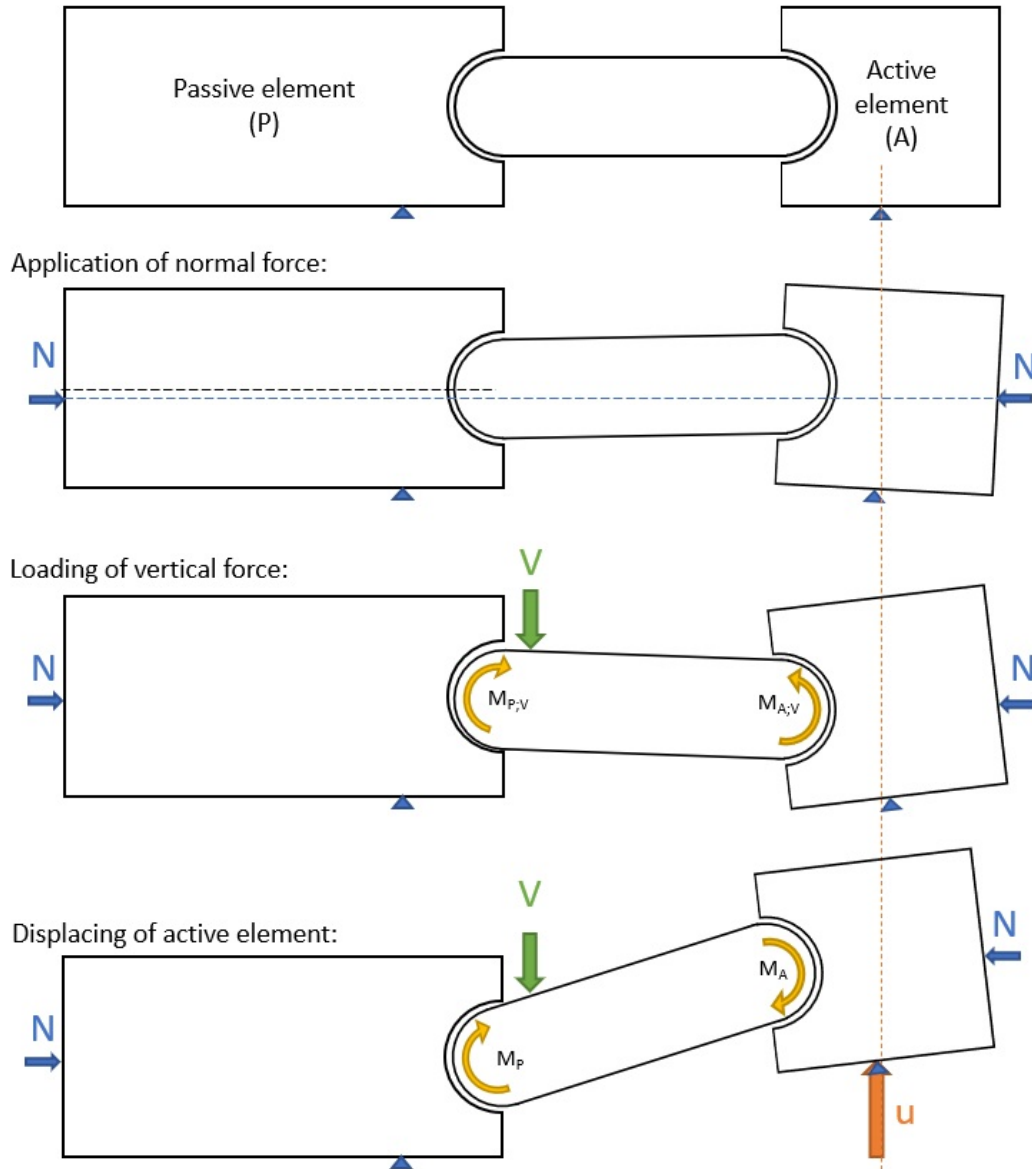


Figure 5.21: Element behaviour during different loading stages - dominant shear force

Implications on the moment and friction derivation for dominant normal loading (case a) are elaborated below. Equation for bending moment in the hinge according to the mechanism obtained from chapter 3:

$$M = \frac{FL}{2} \text{ (or } 2M = FL) \quad (5.4)$$

With the insights shown in fig. 5.20 bending moments are present in the hinges before the application of the heave load. The total increase in bending moment must be attributed to the equilibrium equation as internal work. Below follows the improved mechanical model.

$$\Delta M_p + \Delta M_a = FL \quad (5.5)$$

Where:

$$\Delta M_p = M_p + M_{p,V} \text{ and } \Delta M_a = M_a + M_{a,V} \quad (5.6)$$

The bending moment resulting from the shear load at the active element interface $M_{a,V}$ is only dependent on the resultant contact force Q and the accompanying contact factor f_0 combined with the friction ratio μ . The friction limit is reached due to substantial rotations of the active mother element relative to the father element. The bending moment at this loading phase for the passive side $M_{p,V}$ is not completely governed by the friction limit due to limited rotations along the interface. This bending moment is calculated in the same manner as on the active side but reduces by 70 % for the IF-1 interface and by 30 % for the IF-2 interface, due to the before mentioned effect. This shows the extent of the contribution of each interface side in the bending moment distribution.

$$M_{a,V} = \mu Q_a f_0 R \quad (5.7)$$

For IF-1 interface model:

$$M_{p,V} = \mu Q_p f_0 R 0.7 \quad (5.8)$$

For IF-2 interface model:

$$M_{p,V} = \mu Q_p f_0 R 0.3 \quad (5.9)$$

The assumption is made of identical bending moments at both the passive and active interface during the heave phase due to reaching the Coulomb friction limit. This analytical solution is not valid for interfaces with very small shear stiffness. In that case the friction limit would not be reached. So, for the general case of a shear stiffness where the heave load causes the connections to reach the friction limit:

$$M = M_p = M_a \quad (5.10)$$

By inserting eq. (5.10) into eq. (5.6) and this into eq. (5.5) the formulation for the bending moment in the hinge becomes:

$$M = \frac{FL - M_{p,V} - M_{a,V}}{2} \quad (5.11)$$

With this solution the friction ratio can be formulated as in eq. (3.20) in the formula below. The introduction of the bending moment in the shear load phase causes circular reasoning because these in turn are dependent on the friction ratio. An iterative procedure is required to obtain the correct friction ratio.

$$\mu = \frac{FL - M_{p,V} - M_{a,V}}{2Q f_0 R} \quad (5.12)$$

Implications on moment and friction derivation for dominant shear loading (load case b):

Equation for relative uplifting force depended on the bending moment in both hinge interfaces, obtained from chapter 3:

$$F = \frac{M_p + M_a}{L} \text{ (or } M_p + M_a = FL) \quad (5.13)$$

With the insights shown in fig. 5.21 and the formulations made previously, this changes into the same formulation as in eq. (5.5) for the dominant normal force load case:

$$\Delta M_p + \Delta M_a = FL \quad (5.14)$$

Where:

$$\Delta M_p = M_p - M_{p,V} \text{ and } \Delta M_a = M_a + M_{a,V} \quad (5.15)$$

The formulation of ΔM_p differs here compared to the dominant normal force loading situation. The difference here is that the bending moment at the passive side before the heave phase is of opposite sign due to the opening of the interface, as can be observed in fig. 5.21. By substituting eq. (3.22) and eq. (3.23) from chapter 3 in eq. (5.14) the following formulation for the bending moment on the connection at the passive side is valid:

$$M_p = \frac{(FL + M_{p,V} - M_{a,V})Q_p f_V}{Q_p f_V + Q_a f_0} \quad (5.16)$$

With this solution the friction ratio (as in eq. (3.26)) can be formulated as:

$$\mu = \frac{FL + M_{p,V} - M_{a,V}}{(Q_p f_V + Q_a f_0)R} \quad (5.17)$$

The bending moment resulting from the shear load at the active element interface $M_{a,V}$ is calculate as in the dominant normal force load case because this interface is loaded dominantly in normal force. The friction limit is reached due to substantial rotations of the active mother element relative to the father element. The bending moment at this loading phase for the passive side $M_{p,V}$ is in this case also dependent on the contact force in normal direction due to the substantial peak stress in the shear contact region.

$$M_{a,V} = \mu Q_a f_V R \quad (5.18)$$

$$M_{p,V} = \mu Q_p f_0 R \quad (5.19)$$

With this new insight and the extended analytical formulations, the friction ratio can be calculated correctly and compared to the finite element results. Care must be taken to obtain the correct contact factor f . The 30 to 70 % reduction of the bending moment from the shear load from the full bending moment limited by the friction angle limit does not change between SLS and ULS load levels.

5.2.3 Non-linear structural analysis

To predict the limit state of the concrete hinges a further physical non-linear analysis is preformed. Tensile stresses along the interface are expected to exceed the local tensile capacity so crack formation is expected in the laboratory testing. The extend and pattern of the cracks should be quantified to validate the sensor plan. The material properties of the concrete and reinforcement steel are adjusted to allow for cracking and yielding. The concrete material properties are obtained from testing. It must be noted that this analysis is purely a exploratory investigation in possible areas prone to cracking. It is in no way a model to predict the actual failure modes due to the complex nature of the test.

Table 5.10: Non-linear concrete material properties

Total strain based crack model		
Crack orientation	Rotating	
Tensile behaviour		
Tensile curve	Exponential	
Tensile strength	3.7	N/mm^2
Mode-I tensile fracture energy	0.148	N/mm
Compression behaviour		
Compression curve	Ideal	
Compression strength	43	N/mm^2

Table 5.11: Non-linear rebar material properties

Table 5.12: Coulomb friction interface

Von Mises plasticity		
Total strain-stiffness ratio		
Yield strength	500	N/mm^2
Hardening hypothesis type	Isotropic strain hardening	

The principle stress and crack width are presented for specimens under the different ULS loading conditions. The normal force (N), vertical force (V) and heave (u) magnitudes can be obtained from the loading program, as in table 4.1.

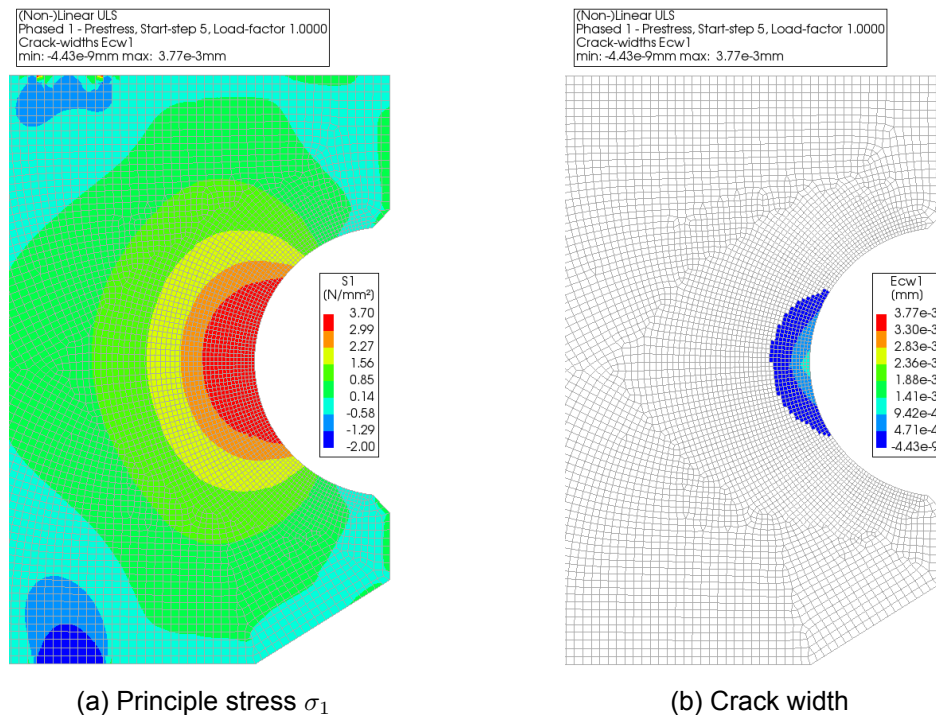


Figure 5.22: Results dominant normal force ULS (Load: N, LC: a-1))

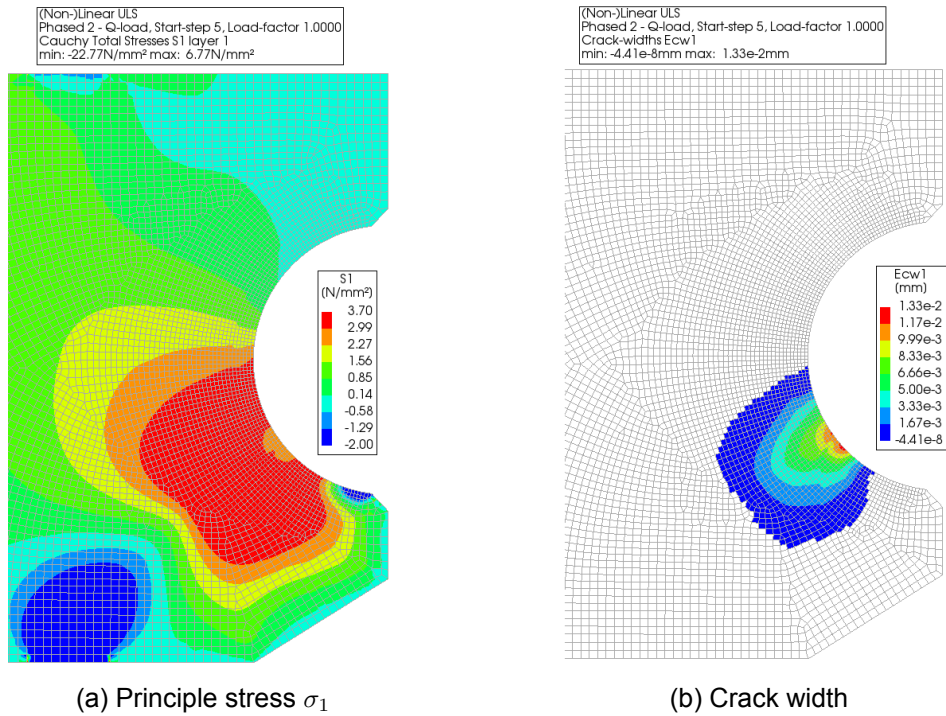


Figure 5.23: Results dominant shear force ULS (Load: N+V, LC: b-1))

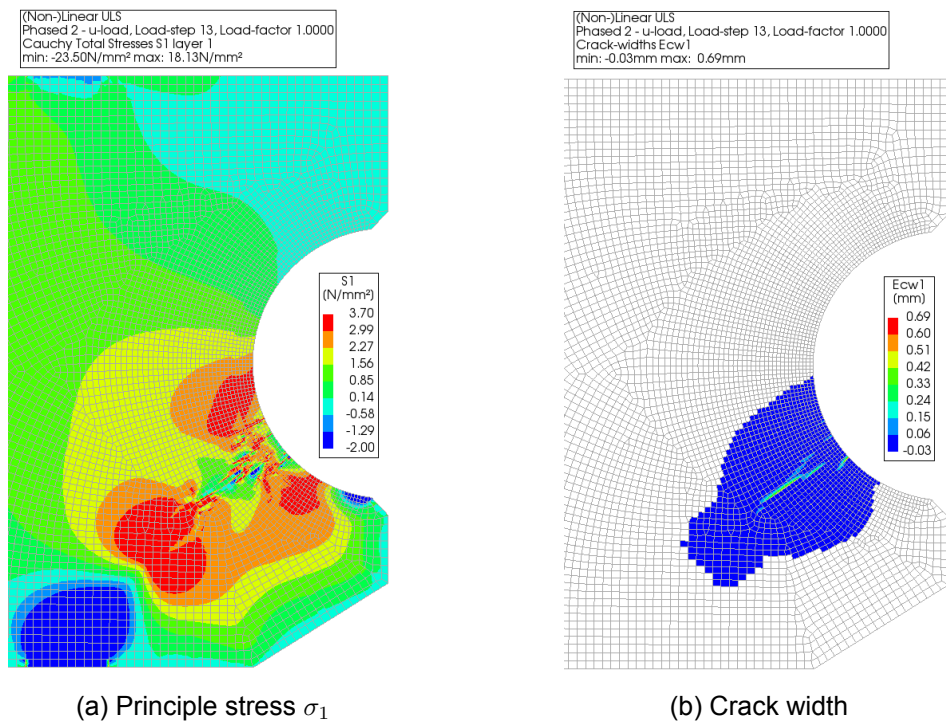


Figure 5.24: Results dominant shear force ULS (Load: N+V+u, LC: b-1))

The specimens pre-stressed with the maximum ULS normal force show tangential stress exceeding the tensile capacity of the concrete. This is the cause for the splitting cracks observed in fig. 5.22. The large shear load on the passive mother element is visualised

in fig. 5.23. Shear cracks are extending from the resultant contact force location to the support of the concrete element. When the heave is applied to the active mother element rotation is initiated in the interfaces. This rotation creates additional shear stresses in the interface. fig. 5.24 shows this load being the culprit of the formation of significant localised cracks. Bending cracks of the father element and splitting cracks originating from the tendon layout are also present. However, these specific cracks are not of interest in this test and do not effect the operation of the hinge. The normal force and vertical force are further increased to obtain possible failure modes in the figures below. A setup loaded solely by a normal force shows a fully spread crack pattern along the interface (fig. 5.26). A clear failure limit is visible based on the loss of stiffness at 14000 kN/0.5 m, observed in fig. 5.25 where the normal force is set out against the opening of the connection (AB). On the other hand, loads in the vertical shear direction show large cracks due to the bottom "corbel" disconnecting from the mother element. Additionally, substantial cracks are observed in fig. 5.28 at the apex of the interface where the circular reinforcement bar is straitening due to the vertical force. The shear force is set out against the vertical displacement of the corbel (B) in fig. 5.27. The majority of the stiffness is lost at 1100 kN/0.5 m with a maximum shear capacity of 1700 kN/0.5 m. Both normal and shear force failure modes show ductile failure with significant cracking.

Normal/axial force failure:

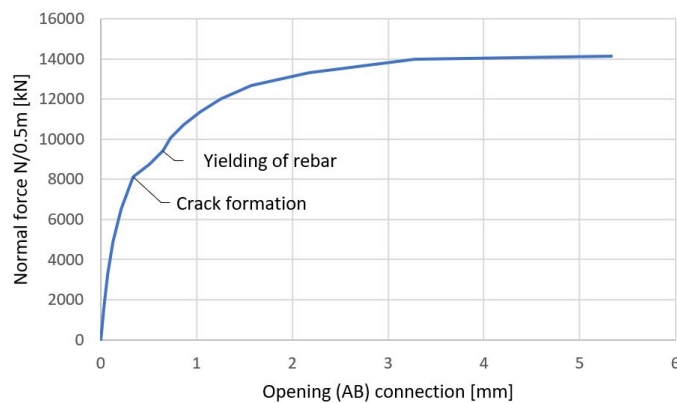


Figure 5.25: Normal force vs opening (AB) connection

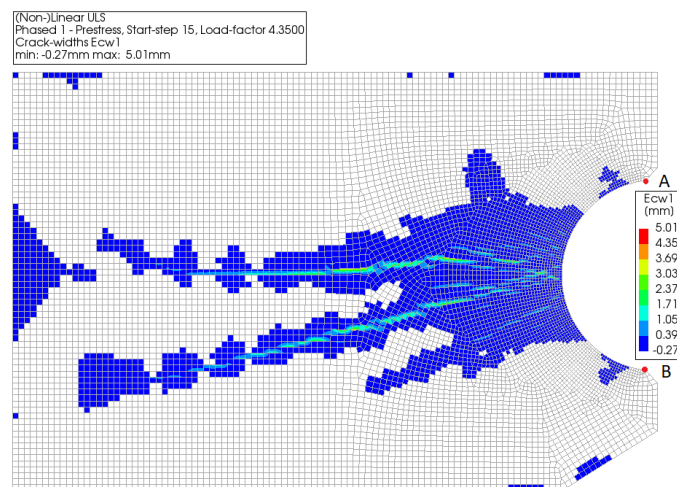


Figure 5.26: Crack width for $N = 14000 \text{ kN/0.5 m}$

Shear force failure:

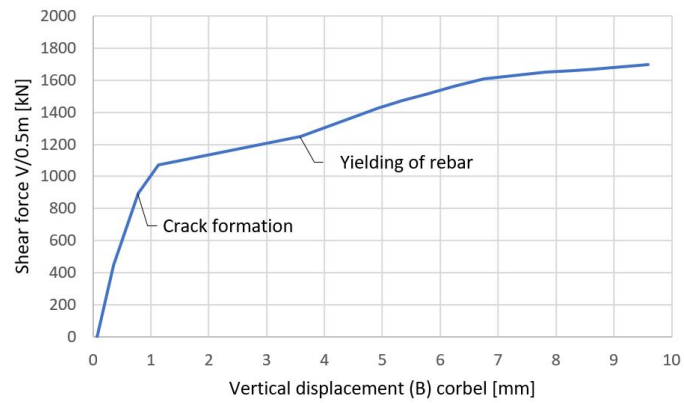


Figure 5.27: Shear force vs vertical displacement (B) corbel

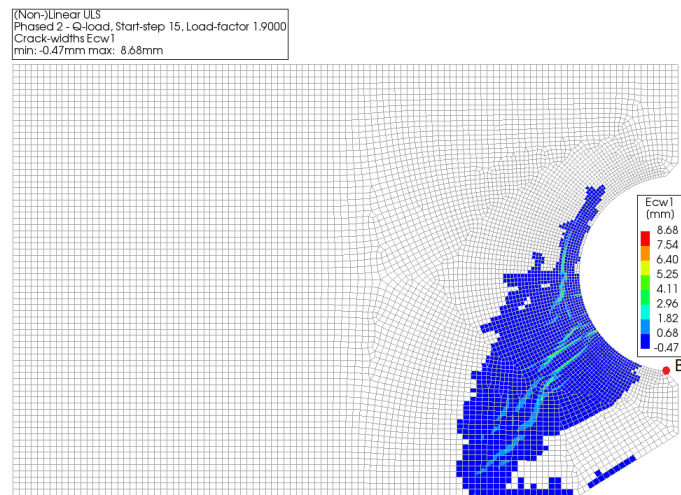


Figure 5.28: Crack width for $V = 1700 \text{ kN/0.5 m}$

6 Analysis of results

Results from the tests and the finite element analysis are analysed in this chapter. The results obtained from the FE elements models, as described in section 5.2, are limited to the topics concerning connection stiffness. Trial tests are excluded from this analysis. This is because different boundary conditions were present during testing affecting the results. Testing of the 2 interfaces for 4 different loading situations with each a repeat test gives 16 data sets. In table 6.1 an overview is presented for all tests with the resultant normal force Q . Load case a-1 contains the dominant normal force load combination and load case b-1 the dominant shear force load combination. Comparable resultant normal forces for each load case would imply a comparable loading situation.

Table 6.1: Resultant normal force Q - passive side

Test	Interface	Load case		Q (kN)
2	Eshastick	a-1	SLS	2176
3	PTFE-SST			2171
4	Eshastick			2183
5	PTFE-SST			2181
2	Eshastick		ULS	3240
3	PTFE-SST			3242
4	Eshastick			3244
5	PTFE-SST			3227
2	Eshastick	b-1	SLS	721
3	PTFE-SST			749
4	Eshastick			716
5	PTFE-SST			707
2	Eshastick		ULS	1011
3	PTFE-SST			980
4	Eshastick			975
5	PTFE-SST			1002

Different properties of the sliding concrete connection are presented and analysed. First, translation and rotation stiffness magnitudes are presented. Secondly, frictional properties are obtained by means of results from the tests and analytical friction theory. Finally, the limit state of the different parts of the connection from the test are compared to the non-linear finite element analysis. Failure modes with the corresponding damage patterns are obtained and visualised. A full overview of the test result can be found in the test result report owned by the client [43].

The following denominations and color codes are used in the presentation of the results:



Figure 6.1: Legend

6.1 Connection stiffness

The stiffness properties of the concrete sliding hinge connection are investigated to obtain knowledge about the performance of the different interface types. Firstly, the translation stiffness is analysed by comparing the compression - normal force relations of the performed tests. Secondly, rotational stiffness behaviour is compared to quantify the friction and its influence on the induced bending moment during the heave loading phase.

6.1.1 Translation stiffness

The concrete elements are pressed horizontally by means of external prestressing steel tendons. The translation is measured during this operation in the test with local displacement sensors (LVDT03 and LVDT07). The amount of normal force can be calculated with the use of the measured data from the tendons equipped with strain gauges. The stress-strain relation of the specific type of high strength steel, which is used, is obtained from tensile testing. Strains in the prestressing tendons are converted to stresses by the elastic Young's modulus of 205000 MPa. The translation stiffness of the connection used in the finite element models is set to match 0.1 mm for a ULS normal force of 3250 kN as described in the parameters in section 5.2.

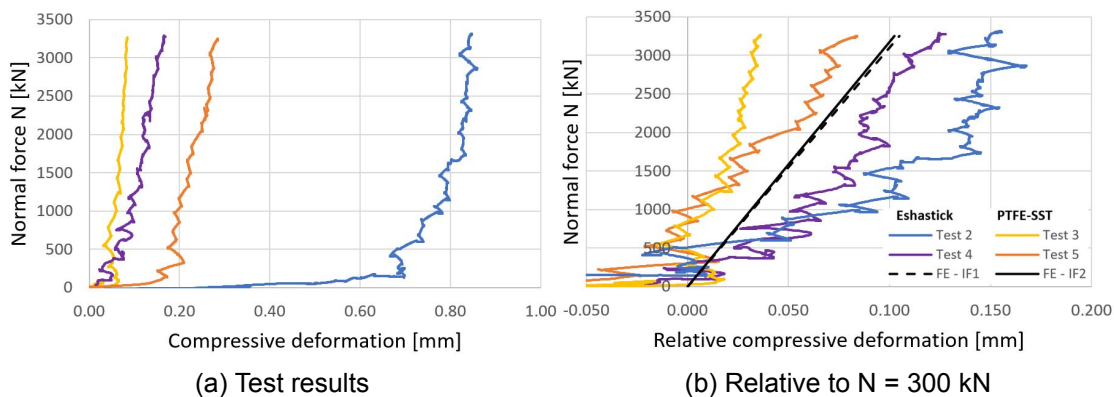


Figure 6.2: Normal force vs interface compression

From the graphs it is visible that the initial compression is distorted by settling of the samples in the test setup. To allow for a comparison between the interfaces a certain benchmark normal force is chosen where all undesirable test setup influence is excluded. In fig. 6.2b the normal force is set out against the relative interface compression from a normal force of 300 kN and onwards. When observing this graph, it is visible that for tests with interfaces equipped with PTFE-SST (test 3 and 5) show less compression of the interface compared to the tests with Eshastick interfaces (test 2 and 4). By linearising the stiffness relation and taking the average of the interface gives for Eshastick 24 mN/mm and for PTFE-SST 66 mN/mm. This simplification is only an indication and does not have

any statistical or realistic value because of the limit number of tests. Additionally, the stiffness relation of the tests with an Eshastick interface show possibly more exponential or bi-linear behaviour.

6.1.2 Rotation stiffness

The rotational stiffness is formulated as the relation between the rotation and the occurring bending moment in the hinge until the bending moment reaches its maximum. The bending moment is a function of the measured uplift force and the initial bending moment before the rotational load. In the graphs below the uplift force of the jack below the active mother element is set out against the prescribed hinge rotation. The support reaction of the vertical force and the self-weight are subtracted from the jack force to obtain this uplift force. First the uplift force - rotation graphs for the dominant normal force tests are displayed followed by the results from the dominant shear force tests. These graphs are obtained from the finite element test models as well. Here 2 calculations are performed: one with the low sliding stiffness and low friction (1.5 %) denoted as IF-1 and the second with the medium sliding stiffness and moderate friction (5.0 %) denoted as IF-2.

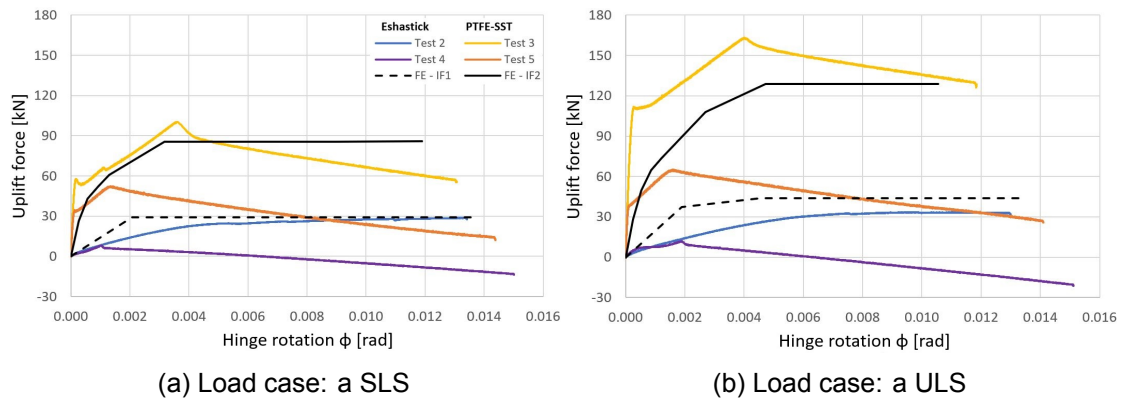


Figure 6.3: Uplift force vs rotation (N » V)

For the dominant normal force tests the graphs show clearly that the specimens with PTFE-SST interfaces require a larger uplift force to plateau. Additionally, more drastic uplift force changes are present compared to the tests where a Eshastick interface is used. From analysis of the sensor data it is clear that before the first sharp bend (at a rotation < 0.001 rad) in fig. 6.3 only the passive side showed relative rotation. This is followed by a less steep force increase while both interfaces are active. This behaviour is not observed for the Eshastick tests where a more smooth rotational resistance is observed. After reaching the maximum uplift force most tests showed a decrease in force except for test 2 where the uplift force stabilised or increased slightly. For the finite element analysis a low stiffness and low friction interface is applied in the IF-1 model. The parabolic stiffness reduction observed for the Eshastick tests is not observed in the IF-1 model due to the initial purely linear interface input parameters. The stiffness obtained from the IF-2 interface model, for the case when both interfaces are active, is matched to the second branch of the PTFE-SST tests. It is clear that for low rotations (< 0.001 rad) a more stiff response is measured for the PTFE-SST tests compared to the finite element analysis of the IF-2 interface model.

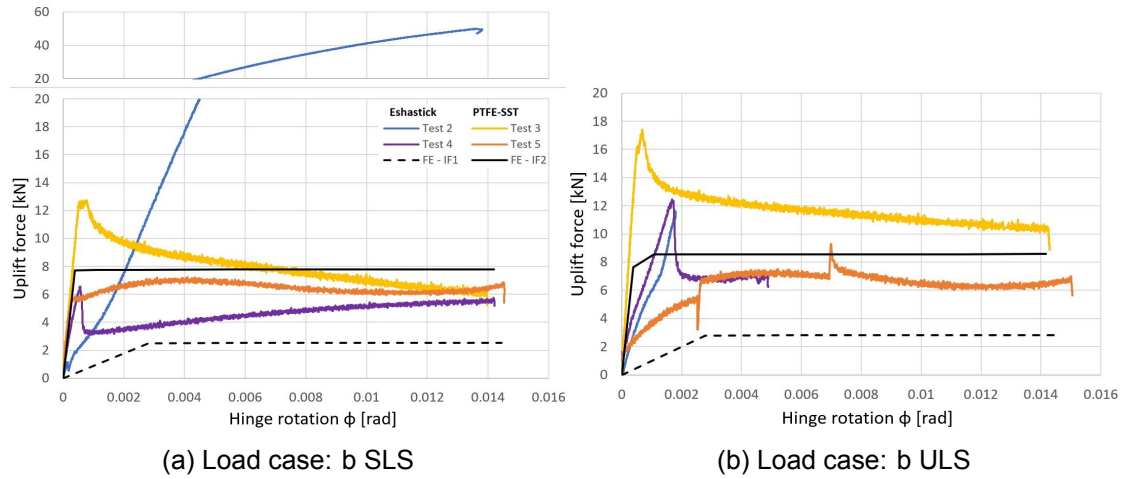


Figure 6.4: Uplift force vs rotation ($N < V$)

The dominant shear force tests show more grouped uplift force increase with the exception of test 2(b). During this test significant uneven in-plane motion of the father element relative to the mother element was observed, possibly affecting the results.

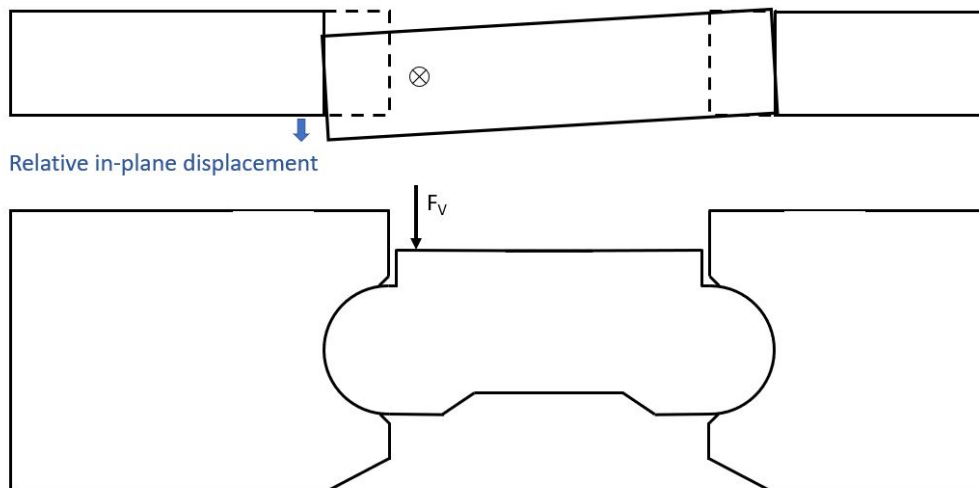


Figure 6.5: Relative in-plane displacement of father element

The absence of a clear plateau of the uplift force during the SLS force and excessive in-plane motion during the ULS test, results in the decision to exclude this test from further analysis. Test 3 and 5, both equipped with PTFE-SST interfaces, show different rotational resistance before reaching the maximum uplifting force. Only test 5 shows a smooth force increase during ULS loading, even compared to test 4 equipped with an Eshastick interface. It must be noted that in this specific case both interfaces showed relative rotation before reaching the maximum. This is not the case for all other tests with a PTFE-SST interface. When the maximum force is reached all graphed uplifting forces show a transition to a new equilibrium. This transition is more gradual with the PTFE-SST tests compared to test 4 with an Eshastick interface, where a more dramatic force reduction is observed. Finite element results of the IF-1 interface model show poor resemblance to the Eshastick tests, both in rotational stiffness and maximum uplift force. The IF-2 model coincides with

the PTFE-SST tests when the initial stiffness is evaluated. In this comparison the initial behaviour of the IF-2 model diverges from the observations from test 5, loaded under ULS conditions. This can be explained by the fact that during loading in test 5 both interfaces registered rotation, unlike all finite element models.

The rotational stiffness of all cases is displayed in the bar graph below. This rotational stiffness relates the bending moment to the rotation in the hinge. With the use of the analytical method and formulas from section 5.2.2 the bending moment is calculated before and during the heave load. The maximum bending moment in the connection at the passive side during the heave load phase is presented in fig. 6.6. It is assumed that the bending moment course follows the uplifting force behaviour. Because of this assumption the stiffness cannot be determined for the dominant normal force tests 3 and 5 due to non uniform rotations in the interface. The values correspond to an assumed linear initial stiffness for the initial 0.0005 rad.

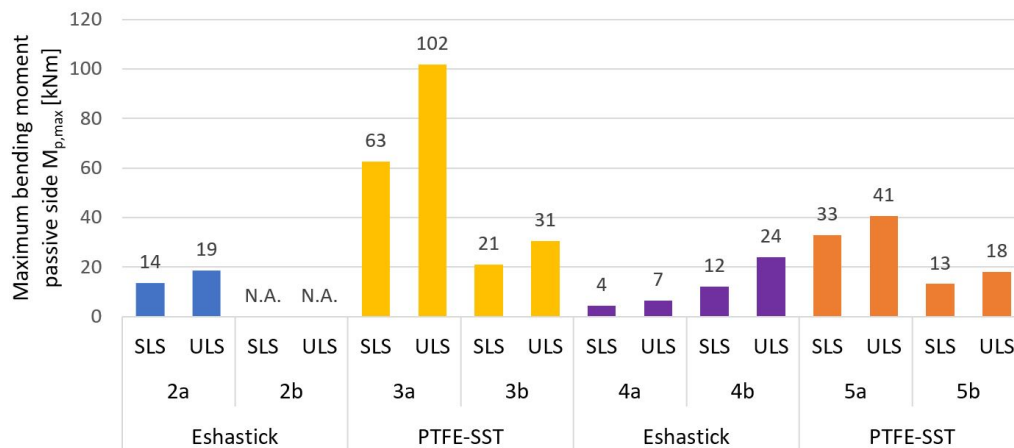


Figure 6.6: Maximum bending moment at passive side

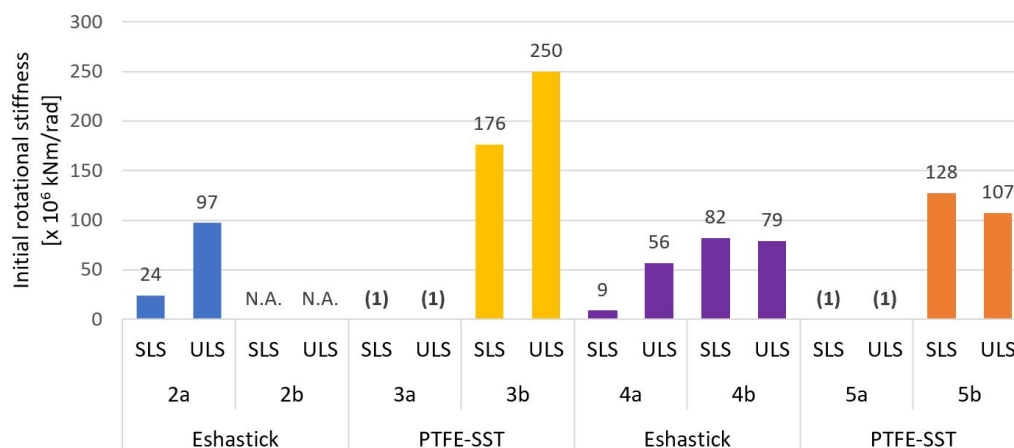


Figure 6.7: Initial rotational stiffness

The rotational stiffness of hinge with a PTFE-SST interface is larger compared to the hinge equipped with an Eshastick interface. Additionally, the test results for elements equipped with an Eshastick interface show already a flattened curve in this initial phase followed by a more significant smoothing until the maximum bending moment is reached.

6.2 Friction

The friction ratio is calculated according to the analytical formulations based on method described in section 5.2.2. For the dominant normal force load case a, the friction ratio is calculated with eq. (5.12). The friction ratio in case of the dominant shear force load case 'b' is calculated by using eq. (5.17). The maximum/plateau of the bending moment from the graphs from the previous section with the bending moment - rotation graphs are used to determine the maximum friction.

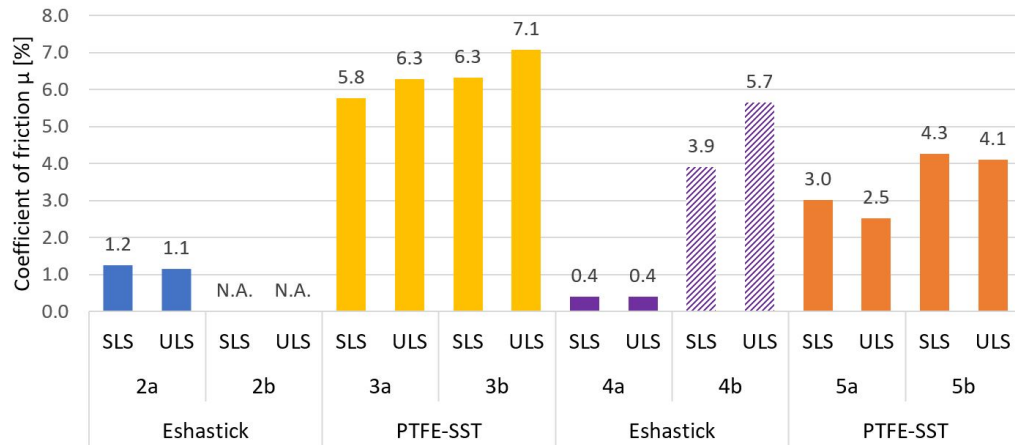


Figure 6.8: Calculated friction ratio

The friction of test 4 under the dominant shear force load cases b (SLS and ULS) is notably high compared to the dominant normal force tests. The course of the uplifting force showed unexpected drastic plateauing followed by a sharp decrease in force (in fig. 6.4). It must be noted that, as for test 2, this test was dominated by unwanted in-plane motion of the father element. With these observations one may conclude that the friction result may be an exaggeration of the actual friction. The cause of this large difference within one test may also be the noncompliance of the Eshastick interface to conform with the Coulomb friction theory. By contrast, the tests where the PTFE-SST interface was applied shows a more concise friction coefficient for the different tests with different contact forces. The majority of the tests show a reduced uplift force after reaching the maximum force. This implies a change in friction. In the case of a PTFE-SST interface this affect could be contributed to the creation of a film as described in the literature review.

6.3 Limit state test

Different limit state load levels are evaluated in the testing project. A serviceability load combination and an ultimate limit state load combination are applied to the setup for both the dominant normal force and dominant shear force tests. The vertical force F_V and the normal force N are varied in magnitude to match the corresponding serviceability or ultimate loads. The dominant shear force test is extended with an additional load to investigate further failure mechanisms by solely increasing the shear force load. When the limit of one of the parts of the concrete hinge is exceeded damage occurs. The occurrence of visible damage does not mean at once that the connection has reached its maximum limit. This depends on the severity and pattern of the damage. Critical parts in the concrete hinge are the interface and evidently the concrete along the cylindrical interface. Crack widths are monitored according to the sensor plan with local displacement sensors and DIC. A complete overview of the results from the crack analysis can be found in appendix B for all tests at SLS load level.

Observed crack pattern in the passive mother element after all testing (Load case a-1, b-1 and for the PTFE-SST test also load case c):



(a) Test 2 Eshastick



(b) Test 3 PTFE-SST



(c) Test 4 Eshastick



(d) Test 5 PTFE-SST

Figure 6.9: Cracks on passive mother element after testing

Three different indicators of failure modes become apparent already in the finite element analysis and are confirmed by the tests:

1. Concrete cracks due to increasing normal force.
2. Concrete cracks due to increasing shear force.
3. Concrete cracks due to rotation.

Additional failure mode indicators to the interface material become apparent during testing:

4. Damage to interface material

The extend of the different indicators of failure modes are investigated for dominant normal and dominant shear force testing and the two different interface compositions: Eshastick and PTFE-SST. Extensive damage is not observed during testing so no clear failure modes are obtained. The observed cracks did not cause the malfunction of the hinge.

6.3.1 Concrete cracks due to increasing normal force

Tensile stresses are expected in the mother elements when the normal force load is applied. The stress distribution of the connection shows the transfer of the normal forces by compression struts accompanied by a tensile tie (see fig. 6.10 in red). This effect is increased by the parabolic stress distribution as described by Hertz. At the apex of the cylindrical surface the tensile stresses reach their maximum. When this tensile stress exceeds the tensile capacity of the concrete a crack will occur.

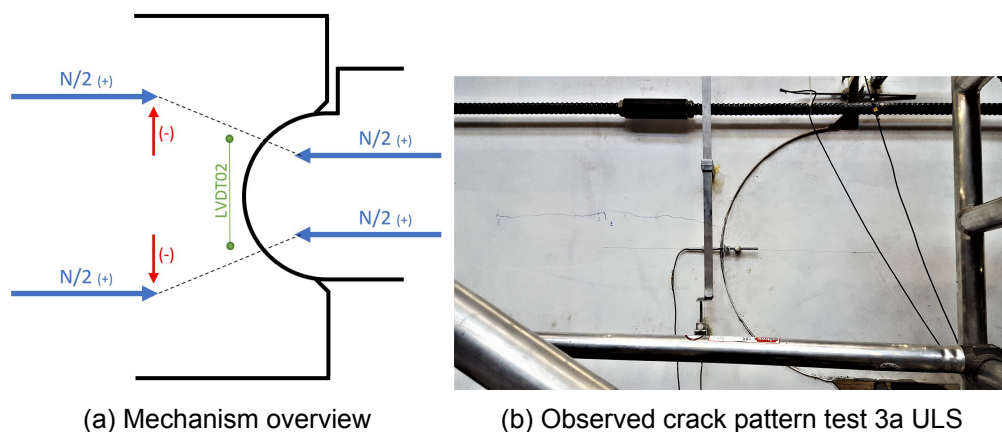


Figure 6.10

To measure this behaviour a distance measurement is implemented in the sensor plan. LVDT02 measures the distance over 500mm in the area of interest. Additionally, manual crack observations are obtained during testing where the crack width (w) and growth is reported. The splitting action of the concrete mother element is set out against the application of the normal force. This normal force is applied with external steel tendons equipped with strain gauges to monitor the total normal force. The dominant normal force tests (a) are evaluated in fig. 6.11.

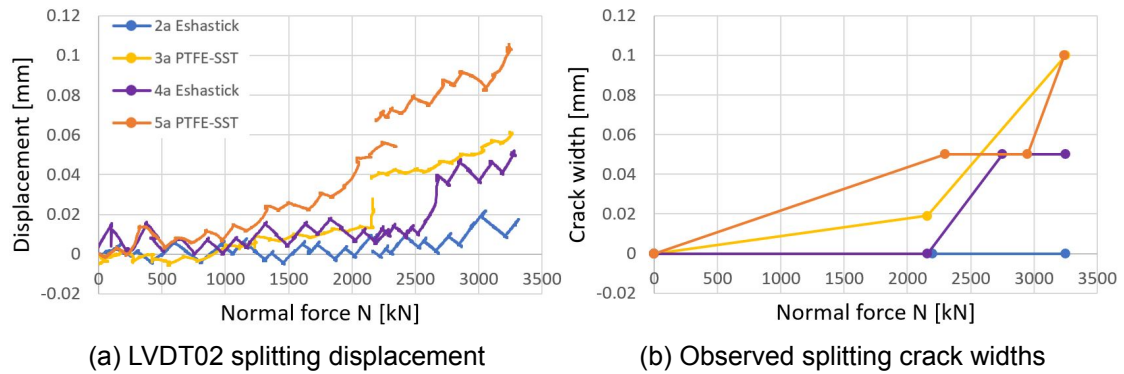


Figure 6.11

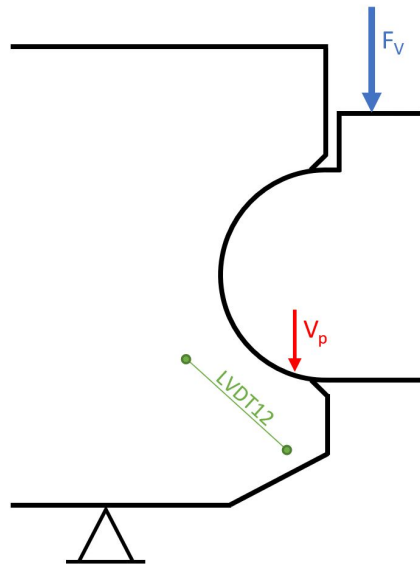
Table 6.2: Splitting crack behaviour overview

	Eshastick interface		PTFE-SST interface	
	Test 2	Test 4	Test 3	Test 5
Crack initiation at N [kN]	-	2600	2150	1500
w_{max} [mm] (at N=3250 kN)	-	0.05	0.10	0.10

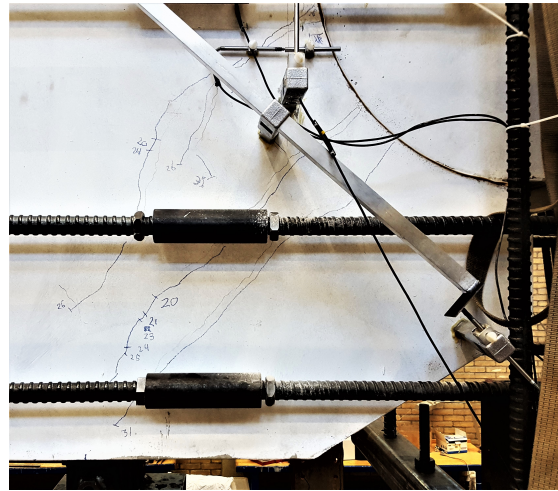
Both the SLS and ULS tests of the dominant shear force tests (a) are displayed. The ULS load is applied from the SLS normal force level of 2150 kN to 3250 kN. This separation is visible in the LVDT02 output because the SLS heave test is performed at the SLS level. For test 2a no splitting cracks are observed. This is supported by the data from the LVDT showing only elastic strains. All other tests show clear splitting behaviour at some point. The observed crack widths are in coincidence with the measured data from the LVDT02.

6.3.2 Concrete cracks due to increasing shear force

The shear load is introduced by applying a vertical force on the father element by means of a jack. For the test where the elements are dominantly loaded in shear this vertical load is placed as close to the passive mother element as possible. In this case the connection at the passive side is normative for the considered shear load. the concrete around the bottom half of the cylindrical behaves as a console. The shear behaviour is monitored by means of displacement measurements in the area of interest with a sensor measuring displacement over a length of 500 mm (LVDT12 as in fig. 6.12a). The cracks which arise in this loading stage are denominated as shear cracks and reported during the increase of the vertical force. The sensor displacement and observed cracks width are related to the relevant shear force. The shear force acting on the connection at the passive mother element is calculated by subtracting the support reaction of the active mother element from the applied vertical force.

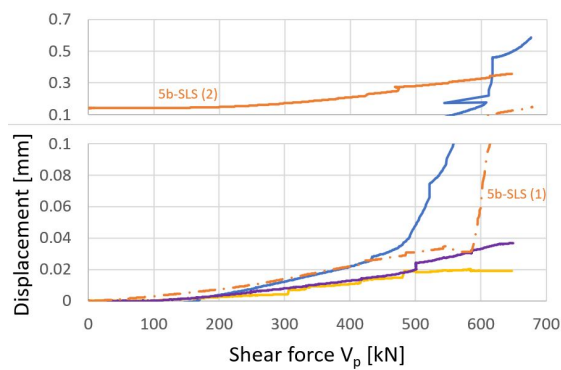


(a) Mechanism overview

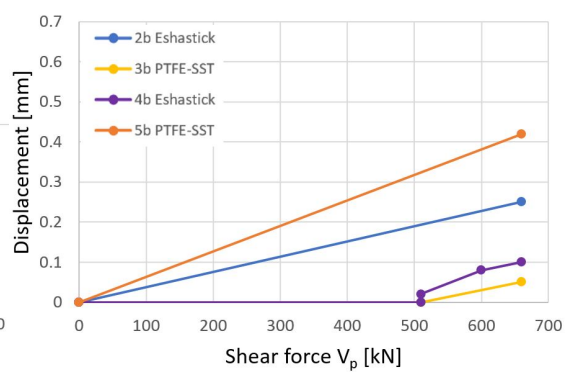


(b) Observed crack pattern test 3b ULS

Figure 6.12

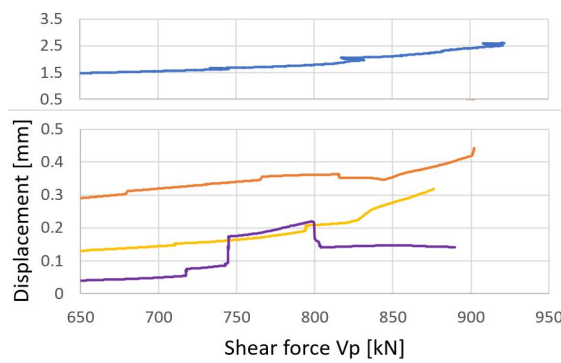


(a) LVDT12 shear displacement

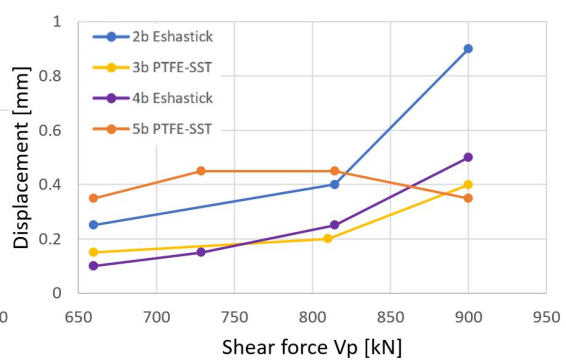


(b) Observed shear crack widths

Figure 6.13: SLS shear load test



(a) LVDT12 shear displacement



(b) Observed shear crack widths

Figure 6.14: ULS shear load test

Table 6.3: Shear crack behaviour overview

	Eshastick interface		PTFE-SST interface	
	Test 2	Test 4	Test 3	Test 5
Crack initiation at V_p [kN]	400	500	660	550
w_{max} [mm] (at $V_p=900$ kN)	0.9	0.2	0.4	0.6

The results are depicted in fig. 6.13 and fig. 6.14 where the data is separated in the SLS load stage (V_p 0-660 kN) and the ULS load stage (V_p 660-900 kN). From the graphs it is visible that for test 2 and 5 a noticeable shear crack is created at around 600 kN of shear force. Test 3 and 5 show less profound cracks in the observed crack overview and the graphed sensor data. A clarification is needed for test 5 where the first test (dash-dotted line 5b-SLS (1)) was not according to the set boundary conditions and repeated correctly causing the created crack to increase. After the SLS heave test having caused some increase in crack width the vertical force is increased to ULS level. Here the shear cracks increase in size slightly when the vertical force is increased. The displacement measured by LVDT12 in test 2 however shows substantial displacement which is not comparable to the observed crack widths. An explanation for this can be the fact that the main shear crack passed the connection point of the sensor causing a faulty displacement measurement.

6.3.3 Concrete cracks due to rotation

The heave, or prescribed upward displacement, of the active mother element created rotation in both concrete sliding hinges. This rotation is restricted by the friction in the interface. Tensile stresses are expected between the concrete element causing the formation of cracks or the opening of existing cracks. The following test results show the increase or decrease from the existing crack size or LVDT displacement measured of the previous loading phase.

Dominant normal force test results

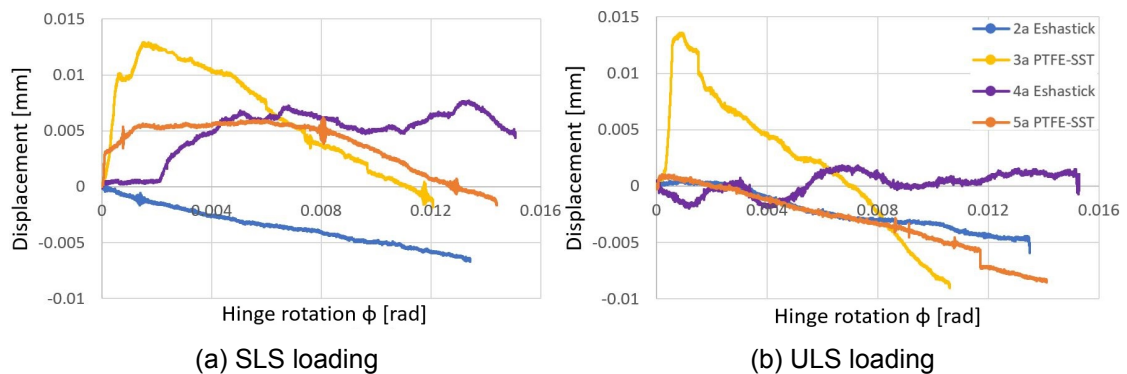


Figure 6.15: Change in LVDT02 splitting displacement heave load test

A further overview of crack observations outside of the measurement range:

Table 6.4: Observed crack width increase (N>V)

Test	2a	3a	4a	5a
SLS	-	-	-	+0.05 mm (new)
ULS	-	-0.05 mm	-	-

In the dominant normal force tests, most of the test results do not show any cracking of the concrete during rotation of the concrete hinge connection. A small reduction of the strain or closing of the cracks is visible for some of the tests. Only during test 5 (PTFE-SST interface), under SLS and ULS loading, a crack formation is observed.

Dominant shear force test results

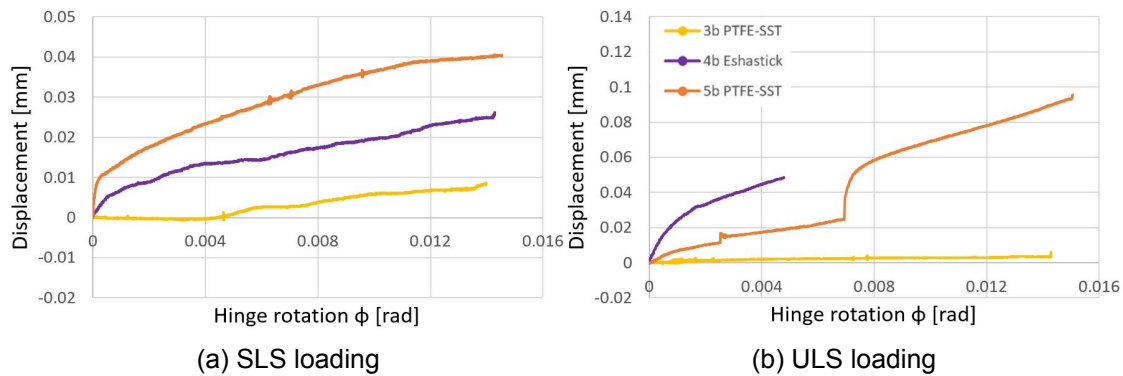


Figure 6.16: Change in LVDT02 splitting displacement heave load test

* LVDT02 not present during test 2

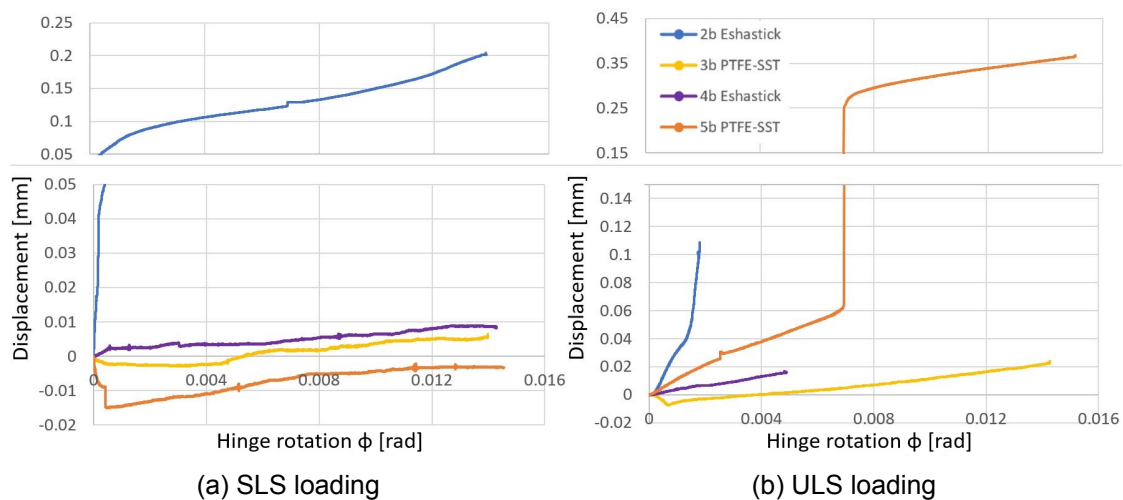


Figure 6.17: Change in LVDT12 shear displacement heave load test

Table 6.5: Observed crack width increase (N<V)

Test	2b	3b	4b	5b
SLS	Crack growth see graphs	-	Crack growth see graphs	Crack growth see graphs
ULS	Crack growth see graphs	Crack growth see graphs	+0.10 mm +0.05 mm	+0.4 mm +0.3 mm

For the test under dominant shear force significant cracking is observed. Under SLS conditions a shear crack increased in width with about 0.2 mm for test 2 where the interface is equipped with Eshastick. For the ULS load significant cracking is visible in test 5 (PTFE-SST interface) with a crack width increase of almost 0.4 mm. From table 6.5, the table presenting the observed cracks, it is clear that test 5 shows the largest cracks during the heave load. The concerning crack extended significantly to the support. This observation is supported by the crack pattern visible when removing the PTFE interface sheet from the passive mother element (see fig. 6.18). It has to be mentioned that the full heave could not be applied for the tests with Eshastick interfaces (test 2 and 4) due to in-plane movement. The sensor measuring the displacement in the shear zone shows a steep increase of displacement until the premature ending of this test.



(a) Test 3



(b) Test 5

Figure 6.18: Cracks interface passive mother element (PTFE sheet removed)

6.3.4 Damage to interface material

- Eshastick interface

Material tests performed by the Gent laboratory investigated multiple bituminous interfaces and showed that extrusion of bitumen during compression is possible. Eshastick was described as the least prone to this phenomenon. During the application of the normal force a limited amount of extrusion of the bitumen was observed in the latter stage of the ULS prestressing.



(a) Extrusion of bitumen (test 2a ULS)



(b) In-plane motion (test 2b ULS)

Figure 6.19

More problematic was the in-plane motion of the father element relative to the mother elements. Small eccentricities in the tests frame may have induced this motion amplified by large contact pressure in the interface. When the in-plane displacement was reaching 10% of the width with a significant rate the testing was aborted as happened during the ULS heave load for the specimens loaded dominantly in shear. This mechanism can be present in the plain strain condition for infinite connection width due to torsional moments in the floor (father element).



(a) Passive mother element



(b) Father element

Figure 6.20: Interface condition test 2 after extraction

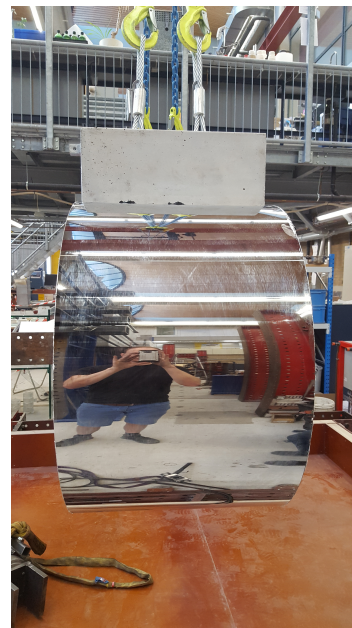
The condition of the interface after testing is shown in fig. 6.20 for test 2. The majority of the interface material has migrated to the father element. This is most probably due to the high contact pressure from the dominant normal force tests.

- PTFE-stainless steel interface

No failure modes were observed during testing for the tests where the concrete elements were equipped with PTFE-SST interfaces. The condition of the interface after testing is shown in fig. 6.21 for test 3. Some parallel marks are present over the length of the interface and the SST sheet metal accompanied by black residue. This deposit could be identified as a PTFE film created during the hinge rotation. Some wrinkling of the PTFE sheet is present at the base where the shear load was transmitted.



(a) PTFE sheet passive mother element



(b) Stainless steel on father element

Figure 6.21: Interface condition test 3 after extraction

7 Connection specifications and design

7.1 Contact mechanics

7.1.1 Stresses at rest

Finite element results of the simplified connection model (section 5.1.1) are compared to the Hertzian and Persson analytical models with no clearance between the two bodies of the connection. The generalised stresses normal to the contact surface are presented in the figure below. It is clearly visible that the Hertzian stress distribution is incomparable with the FE and Persson results. This can be explained by the limitation of the Hertz formulation to non-conforming bodies resulting in an inaccurate contact width. However, the Persson stress resembles the FE results, the angle at which contact is made is overestimated resulting in a lower extreme stress at the base of the line of contact.

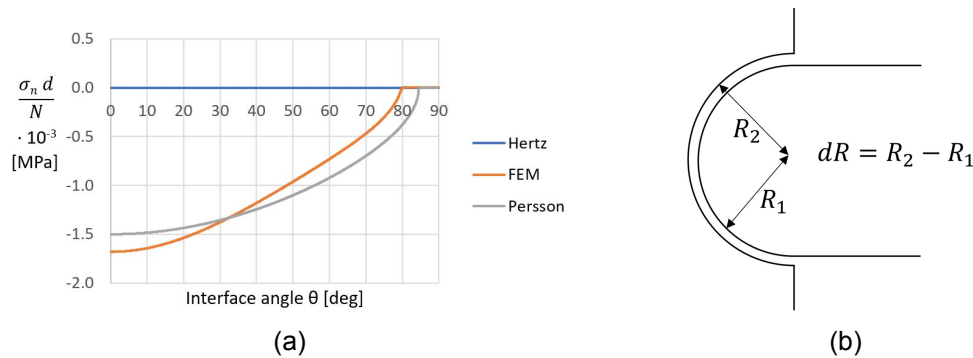


Figure 7.1: Interface normal stress comparison

When different clearances are evaluated the sensitivities of the analytical models become apparent. From a clearance of 0.1 mm the Persson stress distribution closely matches the critical contact angle. The Hertzian theory only complies to the other calculation methods from a clearance of 1.0 mm and onwards.

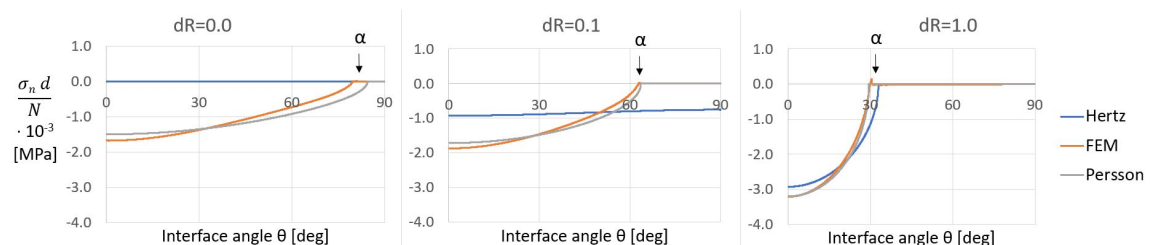


Figure 7.2: Clearance effect comparison

The contact angle for different clearances is graphed below. From this it can be observed for what clearance the Persson or Hertzian contact theory is more accurate:

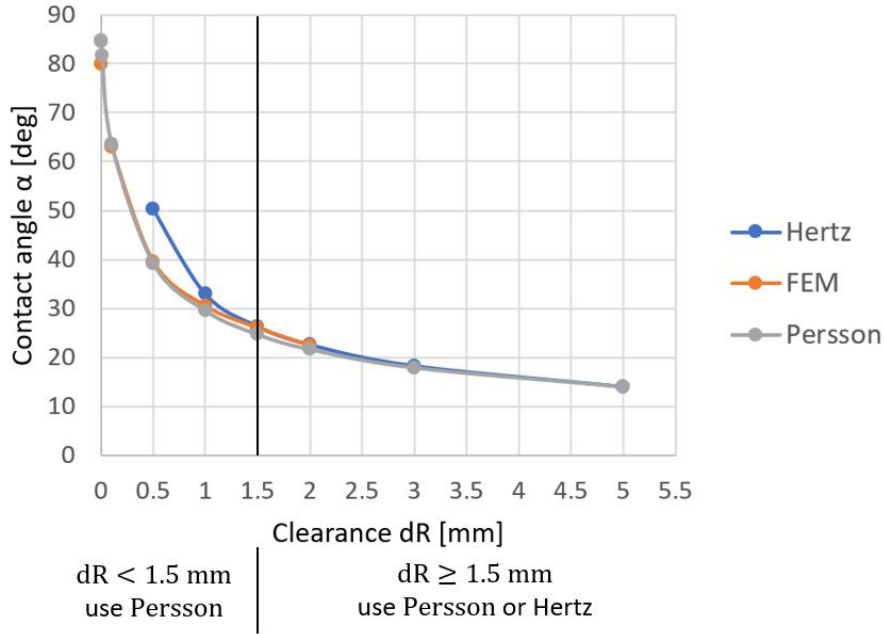


Figure 7.3: Clearance effect on contact angle

However, the more simple Hertz formulation of the contact stresses can still be used for conforming contact when the contact half width (a) is calculated with the more accurate Persson formulation of the contact angle:

$$a_{Persson} = \sin(2 \arctan(b)) R_2 = \frac{2 R_2 b}{b^2 + 1} \quad (7.1)$$

The contact factor for different clearances is determined with a finite element model in fig. 5.8. The observed effect of the clearances can also be calculated with the analytical formulations when the simplification explained above is applied. The contact half width $a_{Persson}$ from eq. (7.1) is implemented in the formulation according to the Hertzian contact theory eq. (2.2) to obtain the relation displayed as a blue line in fig. 7.4. The results shows compliance between the finite element model results and the analytical theory for the considered small clearances.

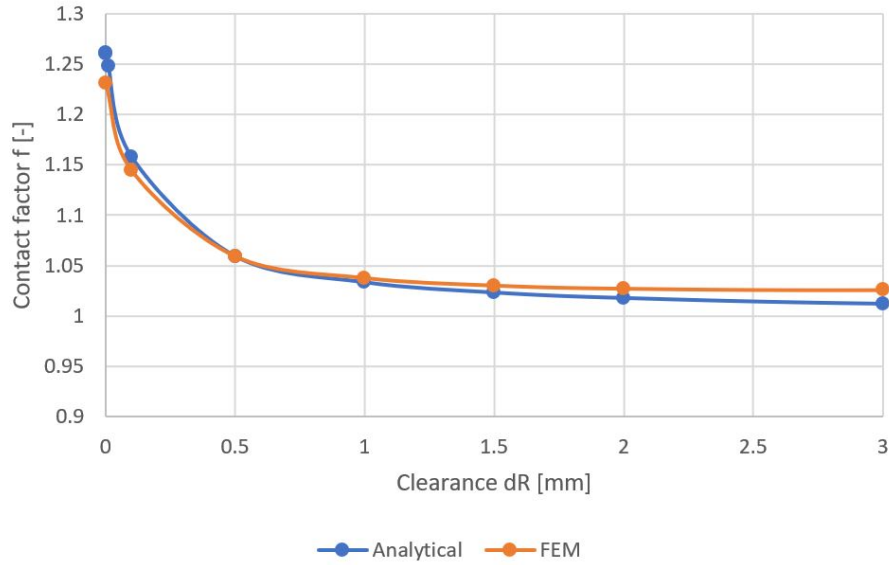


Figure 7.4: Contact factor for different clearances

The clearance significantly affects the contact stresses magnitude and distribution. However, it is assumed that the bearing ensures conforming contact between the concave and convex parts of the connection. This assumption is not validated during the laboratory tests. The method to derive contact stresses is depicted in fig. 7.5. The possibility to include clearances with the Persson theory is added for a complete overview but is not implemented in the mechanism describing the connection in motion.

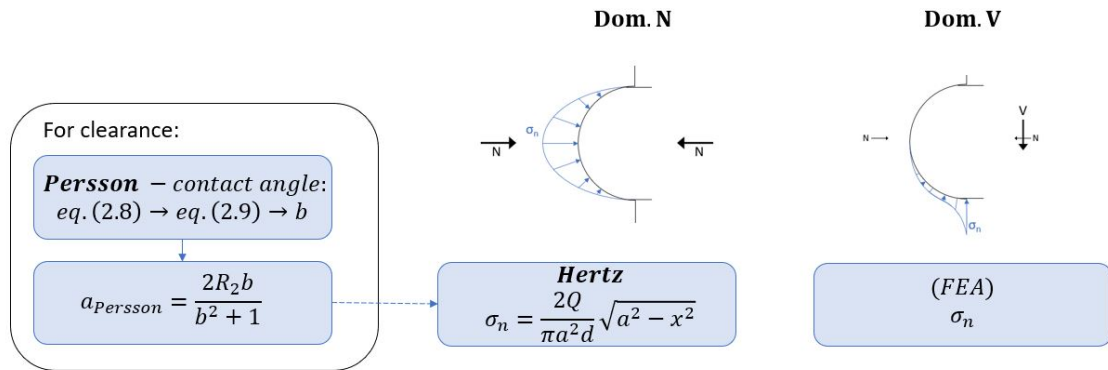


Figure 7.5: Derivation of stresses for a connection at rest

7.1.2 Stresses in motion

The assumed stress distribution in the connection, as described in chapter 3, is observed in the finite element analysis. The normal stress distribution follows the Hertzian theory for a hinge loaded dominantly in normal force. When the dominant force is the shear component a more localised normal stress reaction is created. When a rotational load is applied to the connection a shear stress distribution is created. With the use of a Coulomb friction relation and sufficient rotations, to achieve the limit friction angle, the shear stress is dependent on the normal stress by the friction ratio. A bending moment in the hinge can be described by integrating the shear stresses over the contact area. The parabolic stress distribution described by the Hertz theory results in a specific contact factor connecting the applied load to the force representing the shear stresses integrated over the contact

area. This contact factor is determined to be $4/\pi \approx 1.25$ for connection loaded by solely a normal force. For the extreme case of a full shear load this contact factor is assumed to be 1.0. This is easy to comprehend when the resulting shear stresses form a distribution of a peak load without any substantial spread influencing the bending moment formulation. An overview of the derivation of stresses for a connection in motion is provided in fig. 7.6.

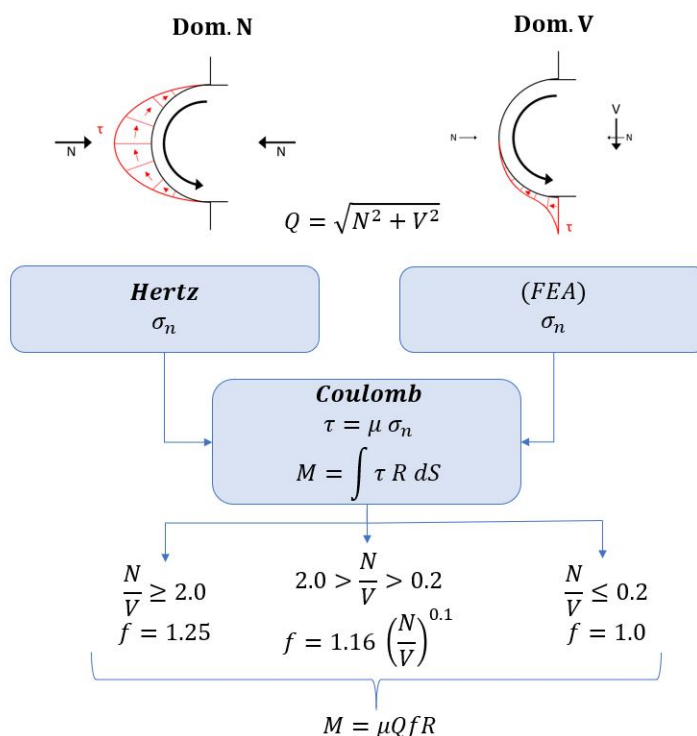


Figure 7.6: Derivation of stresses for a connection in motion

The cases for different normal force – shear force combinations are investigated in section 5.1.4. For N/V ratio's below 0.2 a contact factor of 1.0 is valid. When N/V ratio's higher than 2.0 are present the calculated contact factor of 1.25 is valid. The load combinations within these limits a specific distribution is observed. This can be described by a power series of ax^b with $a = 1.16$ and $b = 0.1$. Conditions to the applicability of this are the absence of clearance and a sufficient normal stiffness to obtain the expected contact area.

7.2 Connection performance

The aim of the application of the concrete sliding connection is to achieve hinge like behaviour. A fixed connection subjected to rotation would give rise to a large internal bending moment. The imposed deformation governs the bending moment due to the significant stiffness of the father element, as can be observed from fig. 7.7. In this simplified model no rotational stiffness is attributed to the mother (wall) elements. This is in contrary to a realistic floor to wall connection where the complete structure ensures a certain rotational stiffness to the connection. The bending moment in the connection can be obtained by solving the ordinary differential equations with the classical displacement method, resulting in eq. (7.2). A bending moment of 43 MNm is expected for a heave of 30 mm, irrespective of the vertical loading situation. Even when a very small deformation of 1 mm is elaborated a bending moment of 1.3 MNm is obtained. Comparing this with the bending

moment calculated from testing as in fig. 6.6: 4-100 kNm, the hinge-like behaviour of the connection is demonstrated.

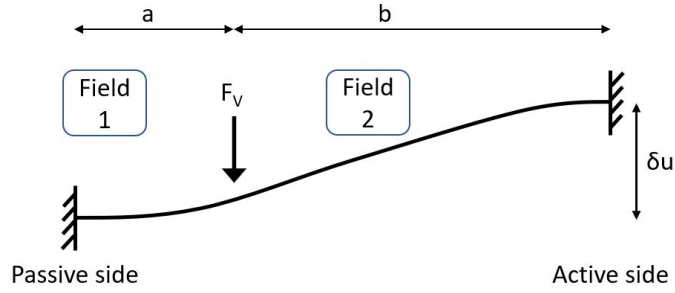


Figure 7.7: Monolithic/fixed loading situation

$$M_{p, fixed} = \frac{6\delta u EI - F_v a b^2}{(a + b)^2} \quad (7.2)$$

Where δu is the heave load and EI is the stiffness of the father element, taken as $EI = E_c \frac{1}{12} b h^3 \approx 1000 \text{ MNm}^2$ with properties and dimensions similar to the laboratory test. The bending moment capacity of the concrete hinge is governed by the weakest cross-section in the design. From fig. 7.8 it is clear that the transition between the father and mother element has a limited lever arm, available within the height of 2 times the radius.

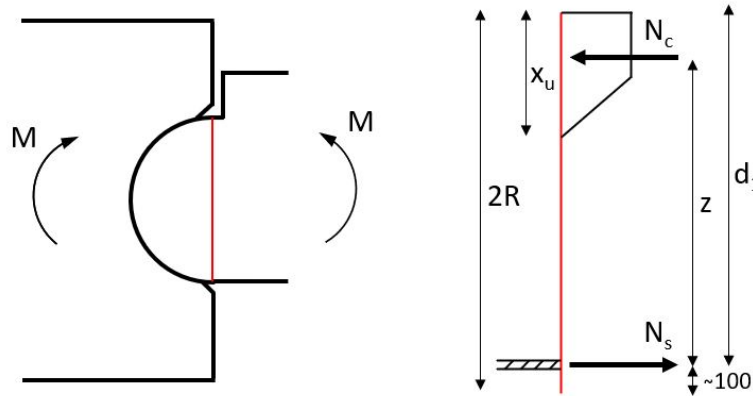


Figure 7.8: Bending moment capacity of critical section

The bending moment capacity of the critical section M_{Rd} can be calculated with the simplified formula based on equilibrium with:

$$M_{Rd} = N_s z \approx (A_s f_{yd})(0.9d_1) 10^{-6} = 232 \text{ kNm} \quad (7.3)$$

Where the amount of reinforcement steel in the tension zone is $A_s = 800 \text{ mm}^2$ (4d16), the rebar design yield strength f_{yd} is 435 MPa for B500 reinforcement steel and dimension $d_1 \approx 2R - 100$ with $R = 400 \text{ mm}$.

The bending moment capacity of the cross-section can also be optimised by increasing the amount of reinforcement steel. The concrete compressive zone is limited to allow for the rebar to yield and prevent brittle failure:

$$M_{Rd,max} = N_c z = (\alpha f_{cd} d x_{u,max})(d_1 - \beta x_{u,max})10^{-6} = 1812 \text{ kNm} \quad (7.4)$$

Where for using concrete class C35/45 the compressive design strength $f_{cd} = 23.3 \text{ MPa}$, $\alpha = 0.75$ and $\beta = 0.39$. The maximum compression zone height $x_{u,max} = (500d_1)/(500f_{yd})$ according to NEN-EN 1992-1-1. This method increases the reinforcement steel amount significantly. Often the concrete class is increased to reduce the reinforcement steel content. From the obtained capacity it is clear that the bending moment for a fixed connection $M_{p,fixed}$, with significant rotations, is impossible to be applied to the connection. However, the maximum observed bending moment during testing of 100 kNm is well below the capacity of the connection.

The test results are analysed in the previous chapter for every test separately. In this section the performance of the connection is discussed for the different loading situations followed by the specific interfaces applied in the tests.

7.2.1 Different loading situations

The concrete hinges are subjected to a variety of loads during testing. The cylindrical interface loaded with a larger normal force is a loading situation often described in the available literature. On the other hand, large shear loads tests on cylindrical interfaces are uncommon due to the fact that a certain normal force must be present to keep the element together.

Dominant normal force load

Forces of 6500 kN/m (LC: a - ULS) are well within the limits for the considered wall to floor connection. Application of this force by means of prestressing the external tendons created relatively small cracks concentrated centrally into a single crack radiating from the interface. There is no sign that these cracks influenced the performance of the hinge in the rotational loading. The non-linear finite element analysis showed a normal force capacity of 28000 kN/m, indicating that this type of connection is well suited for large normal forces.

Dominant shear force load

Large shear force capacity of the concrete hinge is relevant when large vertical loads are considered. From testing it became apparent during the application of the shear load cracks originated at the contact line of the resultant contact force. This occurred for all tests at around 1000 kN/m of shear force (LC: b - SLS). Multiple cracks radiate out from the interface of the support with significant crack widths (up to 1 mm). The rotational load was applied successfully, with the exception of the Eshastick interface tests. However, high shear stresses became apparent by the substantial crack formation/growth during rotation. No clear differences became apparent for the different interface materials applied in the tests. For tests on the specimens equipped with a PTFE-SST interface, the maximum shear capacity is investigated by loading the specimen till failure. The setup capacity of 3000 kN/m of shear force was reached without a sign of shear failure of the bottom "corbel" of the passive mother element. This failure mode was observed in the non-linear finite element analysis, where a shear capacity of 3400 kN/m was obtained with significant loss of stiffness at 2200 kN/m. The connection is more susceptible for shear failure compared to the dominant normal force, as observed from the crack widths and the non-linear finite element analysis.

Table 7.1: Crack behaviour overview

	Eshastick interface		PTFE-SST interface	
	Test 2	Test 4	Test 3	Test 5
Normal force load				
Crack initiation at N [kN]	-	2600	2150	1500
w_{max} [mm] (at N=3250 kN)	-	0.05	0.1	0.1
Shear force load				
Crack initiation at V_p [kN]	400	500	660	550
w_{max} [mm] (at $V_p=900$ kN)	0.9	0.2	0.4	0.6
Heave load				
w_{max} Increase / Decrease	Increase	Increase	Increase	Increase

7.2.2 Bearing interface performance

Two different interface materials are applied as a bearing between the concrete elements: 1) a low stiffness stress absorbing membrane interface (SAMI) material called Eshastick and 2) a more stiff PTFE sheet to stainless steel sheet interface with proven low frictional behaviour.

Eshastick interface

Interfaces based on the Eshastick material showed to be less prone to cracking during the large normal force loads and hinge rotation. Only in one of the two tests a crack of 0.05 mm was observed for the ULS normal force of 6500 kN/m. The derived friction ratio of 0.5 - 1.0 % coincide with the expected low friction as observed in small scale testing. The outliers up to 6 % are observed in tests where the boundary conditions could not be maintained and excessive in-plane displacement was observed possibly affecting the results.

Several mechanisms are known to affect the material properties of a bituminous material significantly but are not elaborated in this research: temperature, adhesion, fatigue and ageing. It is assumed that all testing (including small-scale material testing) is performed at a comparable temperature of around 20 degrees Celsius. Temperatures deviating from this are expected to drastically change the material properties [44]. The adhesion between the two interfaces in contact does not comply with the assumed no-tension model. However, this mechanism is not implemented in the contact model. Fatigue is not of interest for a single load cycle, as is often the case for a structure settlement. Small variations in load may results in sliding and thus fatigue degradation of the material. The testing procedure does include multiple load cycles (at least 4), possibly influencing properties such as the sliding stiffness and the friction coefficient. Aging of bituminous materials has a significant impact on the mechanical properties as described in section 2.2.

PTFE-SST interface

The tests where a PTFE-SST interface was equipped to the mother element showed larger uplift forces to initiate rotations. A certain shear stress is built up before relative rotation is observed in the interface. More uniform friction parameters are derived. For test 3 the friction ratio is between 6 and 7 % and for test 5 between 3 and 4 %. This would suggest that this interface follows the Coulomb friction model. However, a loss of friction is observed after reaching the maximum bending moment during the heave load. This may be due to the creation of a PTFE film when sufficient rotation has been applied to the

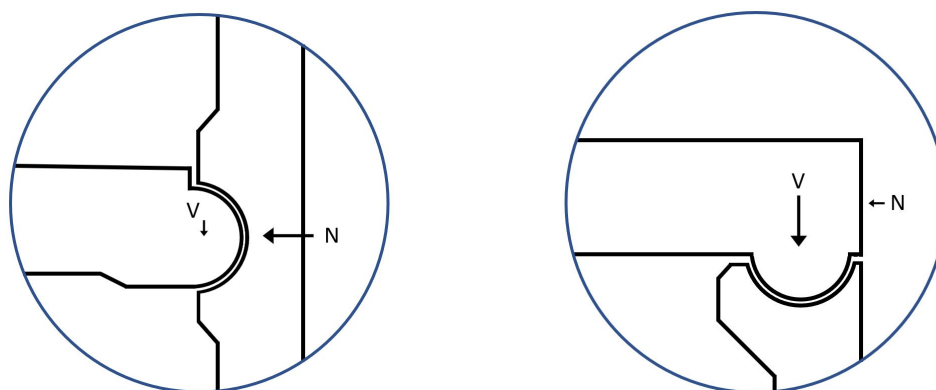
hinge. The crack behaviour is less favourable for the PTFE-SST interface compared to the Eshastick interface. During the increase of the normal force cracking is observed from 4300 kN/m and onwards. The interface is not able to spread the stresses to the extend as the Eshastick interface. Additionally, cracks are formed during rotation of the hinge. These are however small and do not affect the performance of the hinge.

7.3 Critical dimensions and details

The concrete hinge design of the tested connection demonstrated a certain capacity for the considered load combinations. Dimensions of the design govern the contact stress distribution and the overall forces. The relevant dimensions are obtained from the analytical formulations based on different contact theories. Improvements to the design of the connection are attributed based on the critical dimensions and details.

7.3.1 Dimensions

From the performance of the connection, as described in the previous section, a recommendation can be made to load the connection dominantly in normal direction to optimise the capacity and reduce the sensitivity to shear failure. In the case of a floor to wall connection a design can be made where the connection is lined out against the most governing contact force direction. This is depicted for a floor and roof situation in fig. 7.9. When the contact force is acting in a inclined direction relative to the wall a rotated orientation can be implemented. The downside of this design would be the complexity in the construction and probably the additional costs.



(a) Floor design option - dominant hor. load (b) Roof design option - dominant ver. load

Figure 7.9

The case of dominant normal direction is elaborated below. Because shear forces are always present, due to for example the self weight or load variations, the critical dimensions for the dominant shear force load case are also presented.

Case of loading in dominant normal orientation

A dimension with significant importance in the design is the radius of the cylindrical concrete hinge. The size cannot be much larger than the connected element representing the father element (e.g. floor thickness) because of the created section area transition. From the obtained and extended analytical formulations the effect of changing the radius size is investigated. Several aspects are investigated for the case of a concrete hinge loaded dominantly by a normal force. The formulation for the contact stresses are obtained from section 2.3 where the maximum is obtained by evaluating the formulas at the apex of the interface ($x=0$ & $z=0$).

Table 7.2: Aspects influenced by the radius size - LC: a

Internal or external aspects	Formulation	Radius size influence
Maximum normal stress	$\sigma_{n;max} = (2F)/(\pi dR)$	R^{-1}
Maximum tangential stress	$\sigma_{t;max} = (4\nu F)/(\pi dR)$	R^{-1}
Bending moment in connection	$M = \mu Q f R$	R^1

Increasing the radius would have a linear relation to the increase of the bending moment in the mother element of the hinge. Resulting stress distributions in the mother element must be taken into account when designing the reinforced concrete structure. It must be noted that for increasing the radius, not only the internal bending moment increases, but also the bending moment capacity of the critical section, as can be seen from the bending moment capacity calculation in the internal lever arm expression (eq. (7.3)). The influence of the radius size to the interface stresses can be visualised. Stresses are normalised with respect to the applied normal force and the thickness. Just as the described formulations the assumption is made that the contact width matches the radius (no clearance) and the interface has substantial stiffness to allow for the full spread of stresses. The maximum normalised stresses are evaluated from a radius of 100 mm and onwards to disregard the initial stress results for a radius approaching 0 mm resulting in infinite stresses.

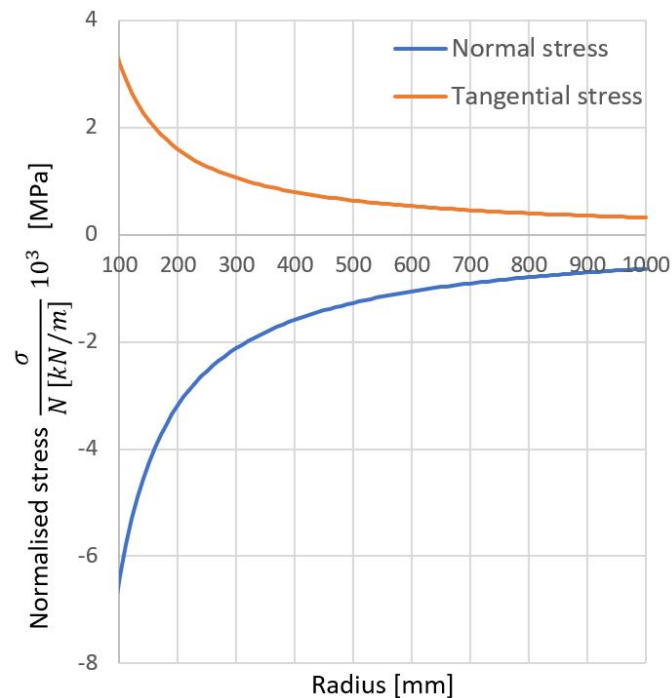


Figure 7.10: Normalised stress for different radius sizes

The method to obtain the contact stress in, for example the tangential direction, with a set radius is as follows: For a radius of 400 mm the normalised tangential tensile stress is $0.64 \cdot 10^3$. Multiplying this by the normal force per meter results in the maximum tensile contact stress. A variation to this is dividing a tensile stress capacity by the normalised tangential stress to obtain the maximum normal force per meter before reaching the tensile capacity. For the case of a tensile capacity limit of 3.7 MPa a normal force of 4650 kN/m is acceptable without any safety factors.

From fig. 7.10 a substantial decrease in the stresses is visible when a radius of 500 mm is applied. Further increase in the radius size would not be as effective due to the increase in cost for the interface. The more spread splitting behaviour is based on the transition in area between the father and mother element. This can be modelled with a strut-and-tie model, as in fig. 7.11. A reinforcement design can be based on the magnitude of the tensile force T . eq. (7.5) and eq. (7.6) show that the radius size is also a contributor to this tensile force through the parameter c . The size of c is obtained by calculating the resultant normal force of half of the interface.

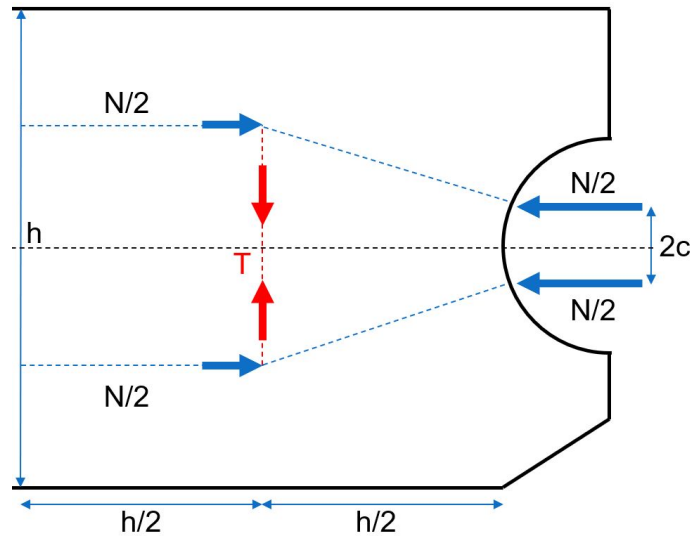


Figure 7.11: Strut-and-tie model splitting behaviour

$$T = \frac{h/4 - c}{h/2} \frac{N}{2} \quad (7.5)$$

Where for a full cylindrical contact without clearance:

$$c = \frac{4R}{3\pi} \quad (7.6)$$

The concrete hinge performed adequate for loads dominantly in the normal direction. The radius size chosen in the tested design of 400 mm is sufficient to prevent excessive tensile stresses in the concrete surrounding the hinge. An interface with a minimum friction and an ability to redistribute stresses would be preferable. These properties can be found in the tested Eshastick interface.

Case of loading in dominant shear orientation

When the results for the concrete hinge loaded in dominant shear force are investigated different design consideration come into play. Stresses are more localised where the resultant contact force is transferred to the mother element. The principle stresses of the concrete surrounding this area are presented in fig. 7.12. This shows the resulting stresses for the hinge loaded with forces matching load case b at ULS level with a stiff interface (IF-2).

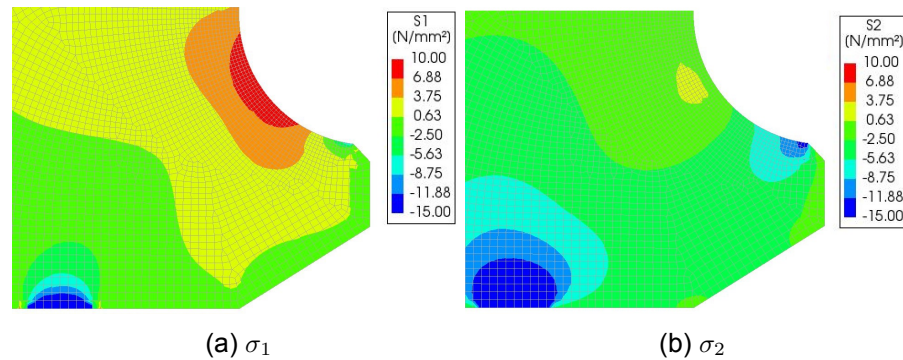


Figure 7.12: Principle stresses - FEM LC:b, IF-2

A small contact area is visible from fig. 7.12b as a concentrated compression zone. This creates a tensile zone further up the interface (see fig. 7.12a) due to the elastic deformation of the cylindrical shape of the interface. The bottom part of the mother element below the interface can be seen as a console. The shear force creates a bending moment because of the lever arm present between the contact point and the vertical support (see chapter 5 for the complete setup). This effect increases the tensile stresses at the interface giving concern to the structure's sensibility to local cracks.

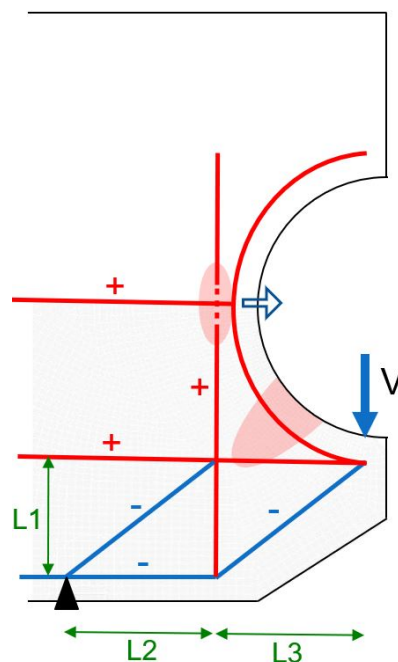


Figure 7.13: Strut-and-tie model shear behaviour

A strut-and-tie model is presented in fig. 7.13 for the connection loaded in shear. Tensile ties are displayed in red and compression struts in blue. The console transferring the shear force to the support is connected to the top part of the connection by means of vertical rebars and the cylindrical rebar along the interface. The latter has a tendency to straighten with the subjected shear loads. Areas sensitive to cracking are identified and marked in red where cracks are expected perpendicular to the tensile ties. The dimensions L1, L2 and L3 govern the extend of the forces in the strut-and-tie model. Increasing the length of L1 would increase the internal lever arm between the main tensile tie and compression strut of the console and thus the capacity. The dimensions L2 and L3 should be minimised to reduce the lever arm between the shear force contact area and the support to minimise undesirable tensile forces in the ties. However, the L3 dimension is directly related to the radius of the cylindrical connection.

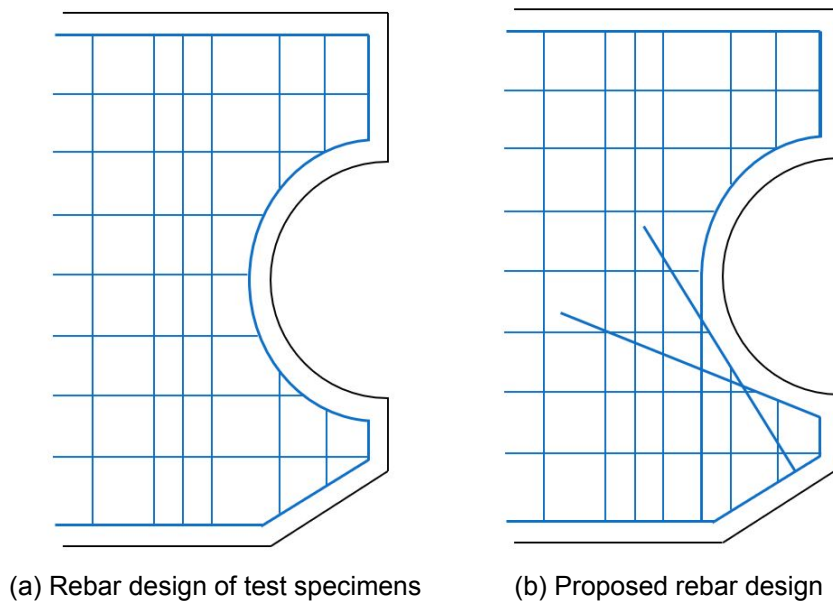


Figure 7.14

For loads in the shear direction several improvements to the design can be made. Decreasing the radius would result in a smaller internal lever arm between the contact force and the area sensitive to tensile stresses. However, a limitation is set to the minimum radius size as it is directly linked to the shear capacity of the father element. The described internal stress distributions for dominant shear loading are less clear than the dominant normal force load case and need to be analysed for every design choice separately. The reinforcement design must be sufficient to distribute and limit the cracks in size. Cracks are observed during the dominant shear force test at the apex of the cylindrical interface along the concrete cover. This mechanism is indicated in fig. 7.14a. This behaviour can be recreated with the finite element analysis (see fig. 5.28) and can be contributed to the tendency of the outer cylindrical rebar to straighten under large shear forces. This can be prevented by avoiding cylindrical rebar along the interface edge subjected to shear forces. In fig. 7.14b a proposed rebar layout is displayed, avoiding the cylindrical rebar at the bottom of the connection. Inclined rebars replace the considered curved rebar without sacrificing the favourable bar orientation. The complexity of the use of cylindrical rebars needs to be assessed for the specific application. Radius size and the reinforcement cage density differs for each design influencing the applicability.

8 Conclusion

Concrete sliding hinges have been around for more than a century. After the extensive use of these connections in arch structures no other application for them have been found. Mid 20th century some promising testing has been performed on the different concrete hinge types. This study shows the applicability of the hinge for different loading combinations. The limit of the concrete hinge must be known before this connection should be implemented in any structure. First this is investigated by gaining an understanding in how the concrete hinge works with respect to the theory of contact mechanics. A mechanical model is created based on this theory to explain the obtained results from laboratory tests. In this study the test results are discussed for a limited number of full scale tests. The ability to accurately model the connection in a non-linear finite element software is important to give insight in internal stresses. The following conclusions can be drawn from this thesis:

- The bending moment capacity of the connection is most critical for the father element at the transition between the mother and father element. Here a limited lever arm is available, dependent and the diameter of the cylindrical connection.
- The internal bending moments in the connection can be calculated by multiplying the contact force with the friction ratio and the radius. This holds when large rotations are expected resulting in the condition where the friction limit of the bearing is reached. The contact force is scaled by the contact factor f . This contact factor depends on the normal stress distribution.
- The internal stress distributions of a cylindrical connection can be described accurately by analytical formulations from the theory of contact mechanics. The Hertzian theory is applicable to quantify the contact stresses, even for small clearances, when the contact area input is calculated according to the Persson formulation.
- The presence of clearance as small as 0.1 % of the radius (0.5 mm for a hinge radius of 400 mm) drastically change the contact stresses. According to the contact theory, contact stresses increase significantly due to the reduction in effective contact area along the interface.
- A Coulomb friction model is able to give an adequate description of the stresses for the connection under sliding action. Interface materials must behave according to this model for a correct description of the stresses in motion. The tested bearing designs, Eshastick-based and PTFE to stainless steel-based, showed results indicating compliance to the applied friction model. Accurate sliding stiffness and friction coefficient properties of the interface must be known before implementing it in the design.
- Eshastick bituminous fiber fabric is suitable to be used as a bearing to aid the sliding of the connection. The low sliding stiffness combined with the low friction ratio of approximately 1 % is beneficial for obtaining a connection with minimal rotational resistance. The connection equipped with this interface has shown a reduced sensitivity to cracking under large normal force loads. This may indicate the ability of spreading the contact stresses along the bearing.

- A connection equipped with a PTFE to stainless steel bearing is well suited to aid the sliding of the connection. Low frictional behaviour was observed with friction ratios of 3 - 4 % and 6 - 7 % closely grouped suggesting good accordance with the assumed contact theory. The larger initial sliding stiffness of this interface increases the risk of early cracking when rotational loads are applied. The interface showed no signs of damage after extensive testing. A perfect circular stainless steel counter surface plate is costly which should be considered for the design.
- The normal force capacity of the connection is significant for the given reinforcement design. Small splitting cracks (<0.1 mm) are observed during testing under the maximum applied normal force load of 6.5 MN/m. Non-linear finite element analysis shows significant cracking from 16 MN/m followed by ductile opening of the connection with a capacity of approximately 28 MN/m. The splitting cracks radiate out from the apex of the interfaced. To optimise the capacity of the connection, it is advised to rotate the connection to match the governing contact force angle to the normal orientation of the connection.
- Dominant loading in the shear direction of the connection should be avoided when possible. The tested connection is sensitive to shear cracks radiating out from the quadrant of the cylindrical interface subjected to the shear load. Crack initiation during testing was observed at 1.0 MN/m of shear, irrespective of the applied bearing. Cracks up to 1 mm are obtained for shear loads of 1.8 MN/m. A maximum capacity of 3.4 MN/m was obtained from a non-linear finite element analysis where a significant loss of stiffness was observed at 2.2 MN/m. Large shear forces create a deformed hinge where a substantial part of the interface is ineffective to transfer stresses.
- An interface for a finite element model with a non-linear normal stiffness to model clearances with a no-tension requirement can accurately show contact stresses. Implementing a Coulomb friction model is sufficient to correctly present the frictional behaviour present in the interface under sliding action.
- The radius of the cylindrical interface dominates the design. Changing the size has both advantageous and adverse effect to the capacity of the hinge under different loading combinations. The maximum bending moment in the hinge can be lowered by reducing the radius size. For a connection, loaded mainly in the normal direction, a maximum radius is desired to limit the stresses in the mother element along the interface. On the other hand, an increased radius adversely effects the shear capacity of the hinge due to the console-like behaviour of the mother element limited by the shear capacity of the father element.

These conclusions support the answering of the main question: What determines the limit state of a concrete sliding hinge connection? The limit state of the connection must be identified for purely static loads and rotational loads separately. For static loads, the connection limits are determined based predominantly on the loading direction and the hinge radius, as the most important connection geometry. The normal force capacity of the connection is significant and is identified as the favourable loading direction. The capacity to shear force, in combination with low levels of normal force, is limited and must be designed for. A sufficient reinforcement layout and more favourable support conditions are required for a connection capable to take significant shear forces. For a rotational load, the interface friction dominates the limit state. For an interface material with a significant low friction coefficient (below 0.1) no sizable bending moment is formed.

9 Recommendations

The obtained knowledge in this report shows promising potential for the implementation of concrete sliding hinges in concrete structures. However, multiple topics need to be elaborated to justify the obtained results in a broader range of applications. A number of recommendations are set out below:

- The applied finite element interface model can be improved by incorporating a non-linear stiffness-relative displacement relation. This would result in the ability of modelling clearance and include nonlinear (e.g. parabolic) response to loads.
- For more extensive research in the applicability of bituminous interface materials an extended formulation of the contact behaviour with more material properties are required. The effect of mechanisms, such as adhesion and aging, might significantly affect the sliding properties.
- Tests up to failure are desired to obtain the true limit state of the connection under different loading conditions. The testing setup should be improved when full scale specimens are preferred. For a failure test considering a maximum normal load, a more uniform prestressing setup is advised over the height to avoid failure due to the tendon setup.
- Additional tests on concrete cylindrical connections is advised for the considered bearing types to validate the assumed stress distributions. Digital image correlation measuring technique can be of good use when this is applied under conditioned circumstances recommended by the software developer. The assumption of conforming contact (no clearance) for the different interface variations in the laboratory test can also be validated with a known contact stress distribution.
- The improved mechanical model, as described in section 5.2.2, is highly dependent on the assumed sliding stiffness of the interface. Therefore, more knowledge about this parameter is key to obtain accurate hinge behaviour. The finding that the interface at the passive side, under dominant normal load, reached 30 - 70 % of the maximum hinge resistance due to the friction angle limit is highly dependent on the significant sliding stiffness. Lower sliding stiffness would significantly reduce this factor and different load combinations as well. Additionally, for every interface material different sliding speeds need to be investigated because this parameter is expected to influence the friction for each material differently.

Bibliography

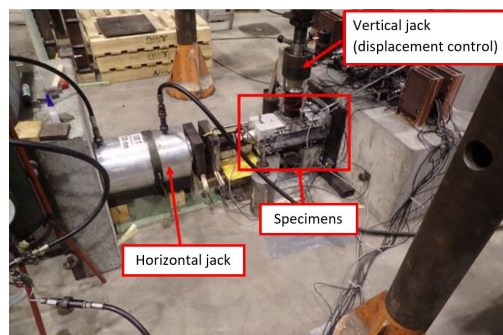
- [1] Gregor Schacht and Steffen Marx. "Concrete hinges in bridge engineering". In: *Proceedings of the ICE - Engineering History and Heritage* 168.2 (2015), pp. 64–74. ISSN: 17579449. DOI: 10.1680/ehah.14.00020.
- [2] Z. Huang and W.L.Nobel. *Full scale test concrete "sliding hinge" for iso-static structural design of hinged double decked tunnels*. Tech. rep. ROTS, 2019.
- [3] Stefan M. Holzer and Karen Veihelmann. "Hinges in historic concrete and masonry arches". In: *Proceedings of the ICE - Engineering History and Heritage* 168.2 (Apr. 2015), pp. 54–63. ISSN: 17579449. DOI: 10.1680/ehah.14.00019.
- [4] Jules Dupuit. *Traité de l'Equilibre des Voûtes et de la Construction des Ponts en Macçonnerie*. Paris, 1870, pp. 194–197. URL: <https://play.google.com/books/reader?id=k7RXAAAAYAAJ%7B%5C&%7Dhl=nl%7B%5C&%7Dpg=GBS.PA194>.
- [5] G. D. Base. *Tests on four prototype reinforced concrete hinges*. Tech. rep. Cement and Concrete Association, 1965.
- [6] Gregor Schacht and Steffen Marx. "Concrete Hinges – Historical development and contemporary Use CONCRETE HINGES – HISTORICAL DEVELOPMENT AND". In: *3rd fib International Congress International Congress*. May. 2010.
- [7] Ralph W. Kluge. "Tests of structural hinges of reinforced concrete". In: *University of Illinois Bulletin* 37.29 (1940).
- [8] W. Brian Rowe. "Application". In: *Hydrostatic, Aerostatic and Hybrid Bearing Design*. Elsevier, 2012. Chap. 1, pp. 1–23. ISBN: 9780123969941.
- [9] J.C. Tarbell. *LM76 Linear bearings*. East Longmeadow, Massachusetts.
- [10] Volker Wetzck. "Brückenlager. 1850-1950". Doctoral thesis. Brandenburgischen Technischen Universität Cottbus, 2010. URL: <https://www.baufachinformation.de/brueckenlager-1850-1950/dis/2011019005465>.
- [11] Madeh Izat Hamakareem. *Cylindrical bridge bearing*. 2020. URL: <https://theconstructor.org/structures/bridge-bearings-types-details/18062/> (visited on 06/04/2020).
- [12] *Beproeivingsverlag Oosterweel*. Tech. rep. Gent, Belgium: Laboratorium Magnel voor betononderzoek, vakgroep bouwkundige constructies, 2018.
- [13] Ehsan Behzadfar and Savvas G. Hatzikiriakos. "Viscoelastic properties and constitutive modelling of bitumen". In: *Fuel* 108 (2013), pp. 391–399.
- [14] Valentin L Popov. *Contact Mechanics and Friction*. Second. Berlin: Springer Nature, 2017.
- [15] *Eshastick G product sheet*. Hoendiep, 2017.
- [16] Ruxin Jing et al. "Rheological, fatigue and relaxation properties of aged bitumen". In: *International Journal of Pavement Engineering* (2019).
- [17] Félix E. Pérez-Jiménez et al. "Analysis of the thixotropic behavior and the deterioration process of bitumen in fatigue tests". In: *Construction and Building Materials* 101 (2015), pp. 277–286. ISSN: 09500618.
- [18] DuPont. *DuPont Fluoropolymers*. 2011.
- [19] Josef Taylor and John Stanton. *Friction coefficients for stainless steel/PTFE (teflon) bearings*. Tech. rep. Washington, USA: Department of Civil Engineering University of Washington, 2010.
- [20] M E Taylor. *low friction sliding surfaces for bridge bearings*. Tech. rep. Crowthorne, UK: Road Research Laboratory, 1967.
- [21] P. Wriggers. *Computational contact mechanics*. Springer, 2006. ISBN: 9783540326083.

- [22] Sattar Dorafshan et al. "Friction Coefficients for Slide-In Bridge Construction Using PTFE and Steel Sliding Bearings". In: *Journal of Bridge Engineering* 24.6 (2019), pp. 1–16. ISSN: 10840702. DOI: 10.1061/(ASCE)BE.1943-5592.0001417.
- [23] Kyuichiro Tanaka and Satoshi Kawakami. "Effects of Various Fillers on the Friction and Wear of PTFE-Based Composites". In: *Wear* 79.2 (1982), pp. 221–234.
- [24] Ian Hutchings and Philip Shipway. *Tribology*. Matthew Deans, 2017, p. 352. ISBN: 9780081009109.
- [25] Zhangang Sun and Caizhe Hao. "Conformal Contact Problems of Ball-socket and Ball". In: *Physics Procedia* 25 (2012), pp. 209–214. URL: <http://dx.doi.org/10.1016/j.phpro.2012.03.073>.
- [26] M. J. Fagan and J. McConnachie. "A review and detailed examination of non-layered conformal contact by finite element analysis". In: *Journal of Strain Analysis for Engineering Design* 36.2 (2001), pp. 177–195.
- [27] Nicholas Lecain. *Tutorial of Hertzian Contact Stress Analysis*. Tuscon, USA, 2011.
- [28] Allan Persson. "On the stress distribution of cylindrical elastic bodies in contact". Doctoral thesis. Göteborg, Sweden: Chalmers University of Technology, 1964, p. 147.
- [29] Michele Ciavarella and Paolo Decuzzi. "The state of stress induced by the plane frictionless cylindrical contact. I. The case of elastic similarity". In: *International Journal of Solids and Structures* 38.26-27 (2001), pp. 4507–4523.
- [30] Michele Ciavarella and Paolo Decuzzi. "The state of stress induced by the plane frictionless cylindrical contact. II. The general case (elastic dissimilarity)". In: *International Journal of Solids and Structures* 38.26-27 (2001), pp. 4525–4533. ISSN: 00207683.
- [31] K.L. Johnson, Kevin Kendall, and A.D. Roberts. "Surface energy and the contact of elastic solids". In: *Proceedings of the Royal Society of London. A. Mathematical and Physical Sciences* 324.1558 (1971), pp. 301–313. ISSN: 2053-9169.
- [32] Joseph F. Labuz and Arno Zang. "Mohr-Coulomb failure criterion". In: *Rock Mechanics and Rock Engineering* 45.6 (2012), pp. 975–979.
- [33] MIT. *Mohr-Coulomb model*. URL: <https://abaqus-docs.mit.edu/2017/English/SIMACAETHERefMap/simathe-c-mohrcoulomb.htm> (visited on 04/02/2020).
- [34] K. L. Johnson. *Contact Mechanics*. First. Press Syndicate of the University of Cambridge, 1985, p. 428.
- [35] 3M. *How Does Adhesion Work?* URL: https://www.3m.com/3M/en%7B%5C_%7DUS/bonding-and-assembly-us/resources/how-does-adhesion-work/ (visited on 04/03/2020).
- [36] *DIANA Documentation* 10.3. 2019. URL: <https://dianafea.com>.
- [37] P J G Schreurs. *Material Models - course 4A330*. 2012.
- [38] K. Anupam. *Visco-elasticity lecture CIE4353 TUD*. 2019.
- [39] M. Sadeq et al. "Assessment of linear and nonlinear viscoelastic responses of warm-mix asphalt binders". In: *6th International conference bituminous mixtures and pavements*. July. Thessaloniki, Greece: Taylor & Francis Group, 2015, pp. 27–32. ISBN: 9781138028661. DOI: 10.1201/b18538-6.
- [40] Max A N Hendriks, Jan G Rots, and Modeling Steel. *Computational Modeling of Structures - Discrete cracking*. 2015.
- [41] Prefaco. *Compressive strength raw data*. Lommel, Belgium, 2020.
- [42] CEN. *NEN-EN 1992-1-1 EC2: Design of concrete structures, General rules and rules for buildings*. Tech. rep. NEN, 2011, p. 107.
- [43] W.L. Nobel. *Results and interpretation testing campaign concrete hinge*. Tech. rep. ROTS, 2020, p. 97.
- [44] Kumar Anupam. *Lecture Continuum Mechanics - Visco-elasticity*. 2019.

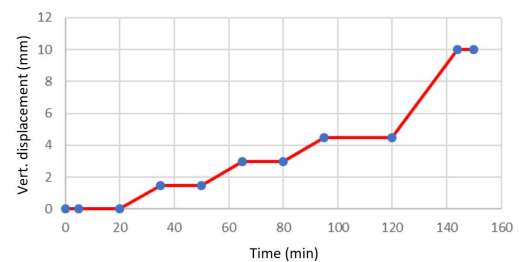
A Interface test data

Test setup

Magnel laboratory for concrete research of the Gent University performed material tests specifically for this research project. Nine interface materials are selected by their low friction behaviour. The interface plates (150 x 150 mm) are attached to concrete cubes. Three cubes are placed in the test setup confined by a horizontal jack at one end and an end support at the other end. The middle of the three cubes is subjected to vertical loading by a jack as can be seen from fig. A.1a.

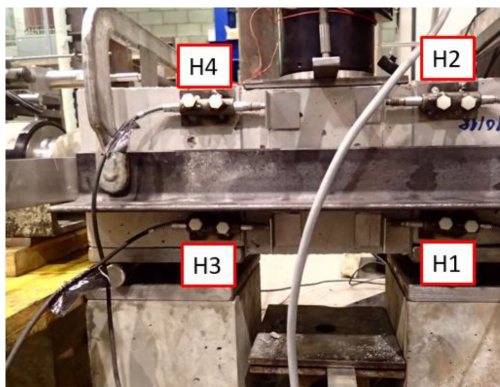


(a) Test setup

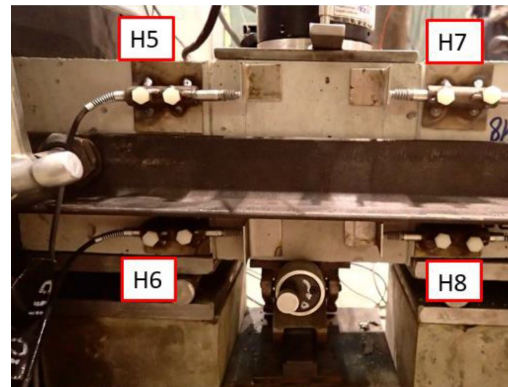


(b) Loading scheme

Figure A.1: Interface friction test [12]



(a)

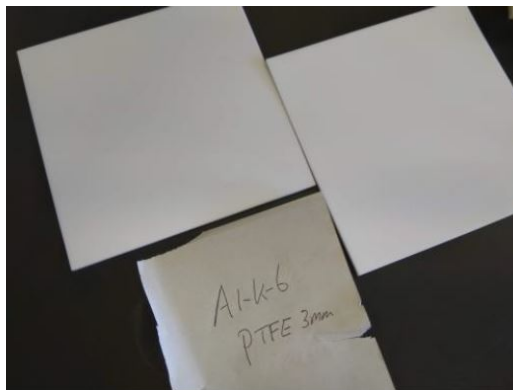


(b)

Figure A.2: Horizontal LVDT locations [12]

The specimens are loaded horizontally with a force of 250 kN provided by a hydraulic jack. The vertical load is applied according to the loading scheme as in fig. A.1b. The horizontal force is applied while measuring the horizontal displacement with the measurement setup from fig. A.2. This force is kept constant during the experiment. The vertical displacement is measured at the application point of the vertical jack.

This annex focuses on two of the tested interface materials: PTFE (fig. A.3a) and Eshastick (fig. A.3b).



(a) PTFE



(b) Eshastick

Figure A.3: Considered interfaces [12]

Test results PTFE

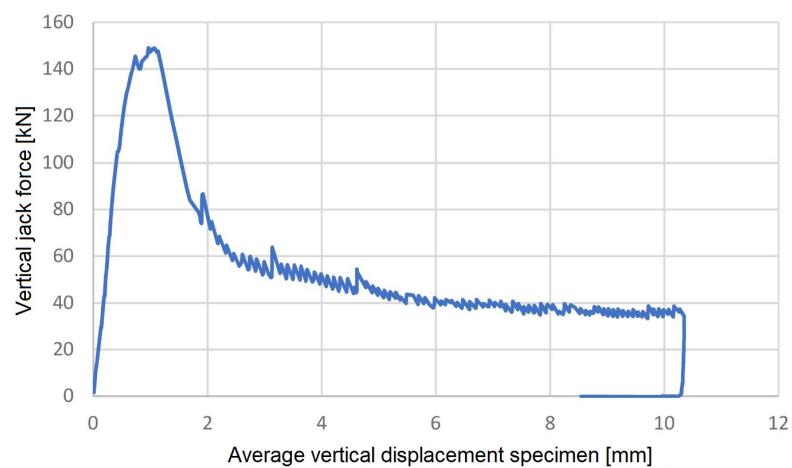


Figure A.4: PTFE: Vertical jack force vs average vertical displacement of specimen

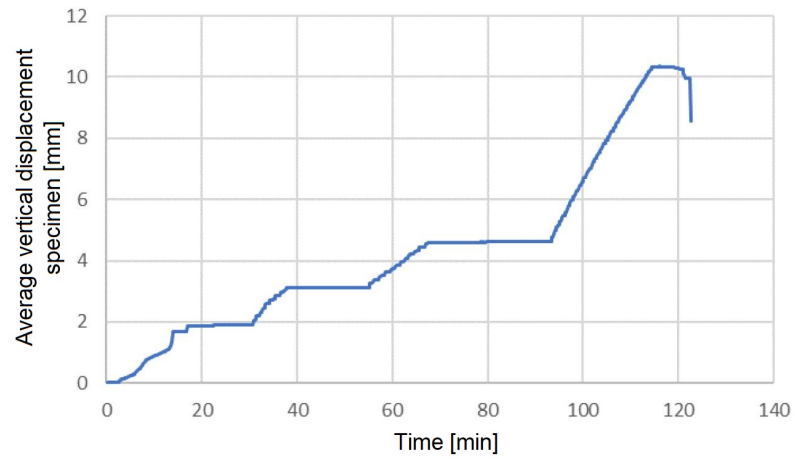


Figure A.5: PTFE: Average vertical displacement of specimen vs test time

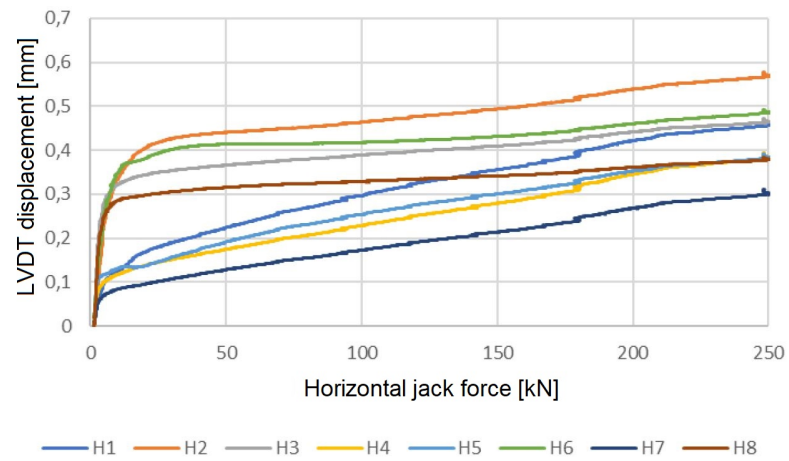


Figure A.6: PTFE: Horizontal displacements vs application of horizontal jack force

Test results Eshastick

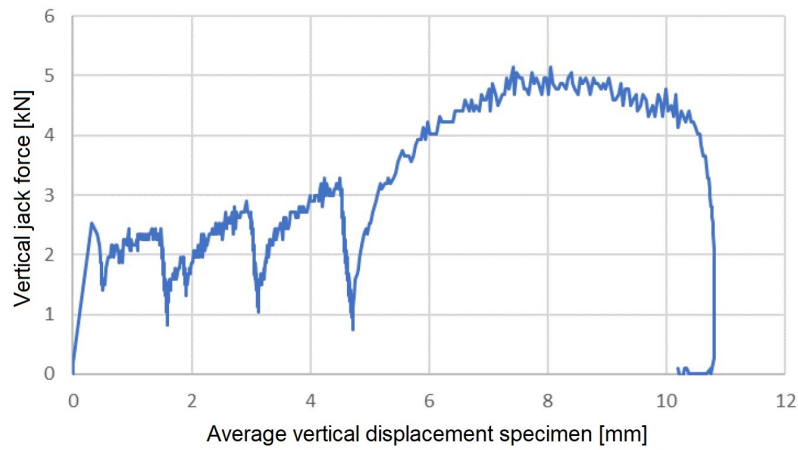


Figure A.7: Eshastick: Vertical jack force vs average vertical displacement of specimen

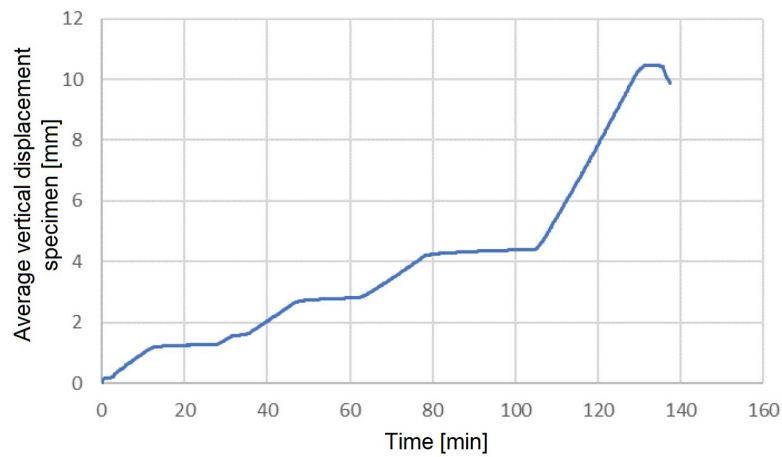


Figure A.8: Eshastick: Average vertical displacement of specimen vs test time

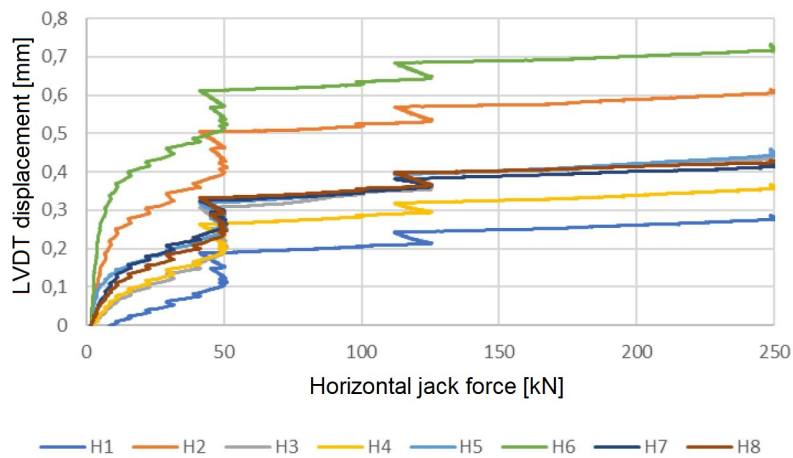


Figure A.9: Eshastick: Horizontal displacements vs application of horizontal jack force

B Crack analysis

Crack patterns and crack widths are presented for loads at SLS level. The crack width data is obtained from local displacement measurements (LVDT) on the north side of the specimens and by means of digital image correlation (DIC) on the south side. See next page for crack analysis of test 2 - 5.

Test 2a - dominant normal force

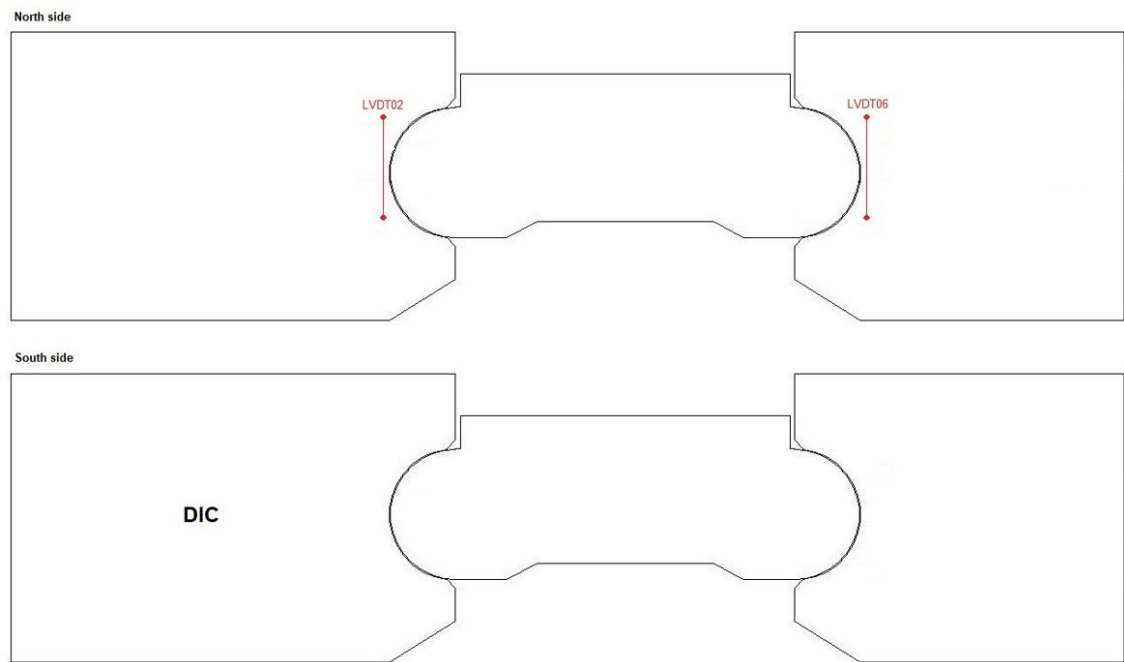


Figure B.1: Crack overview

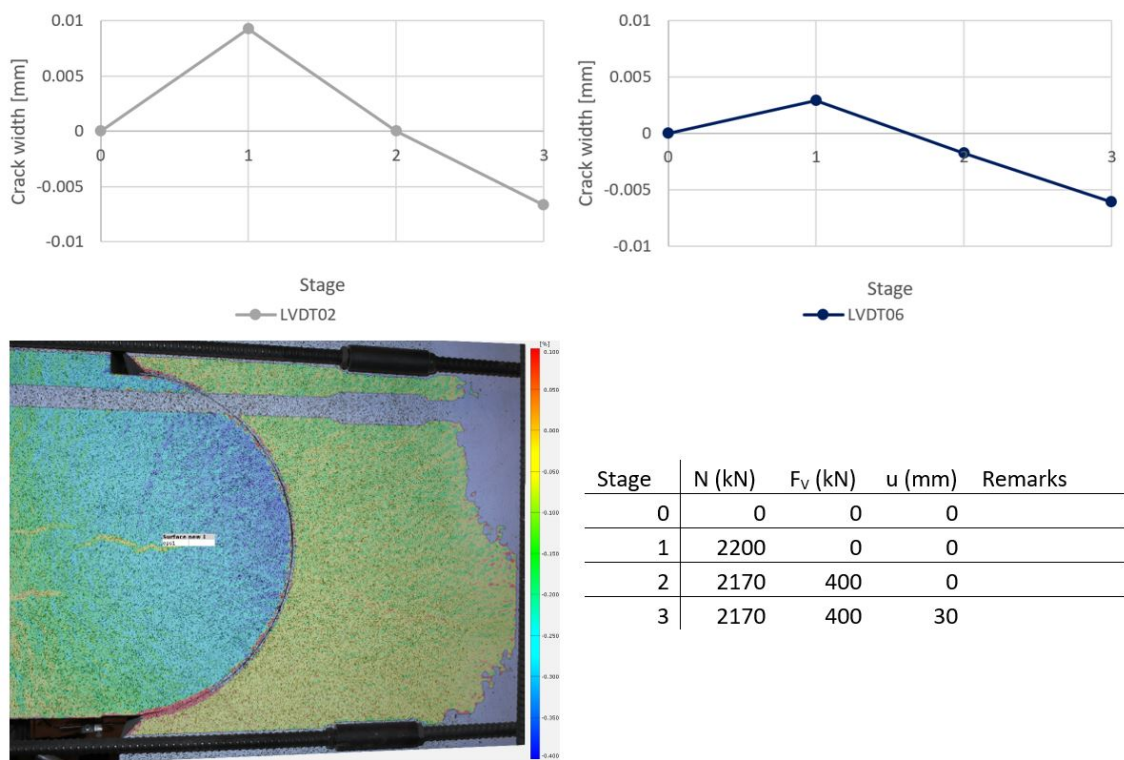


Figure B.2: Crack observations

Test 2b - dominant shear force

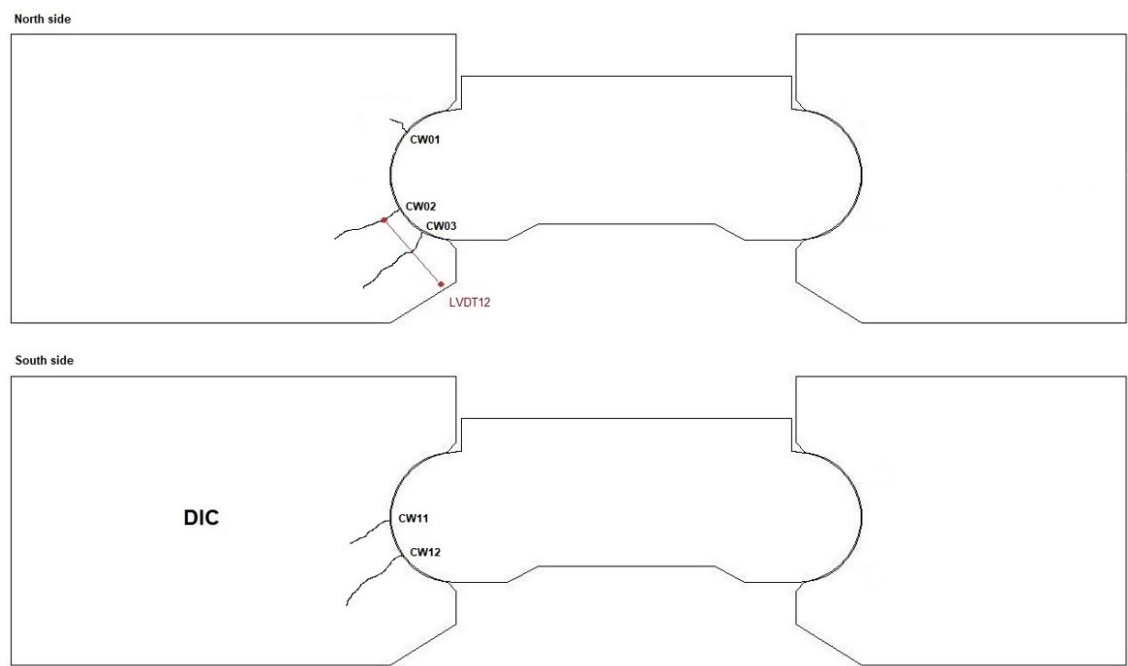


Figure B.3: Crack overview

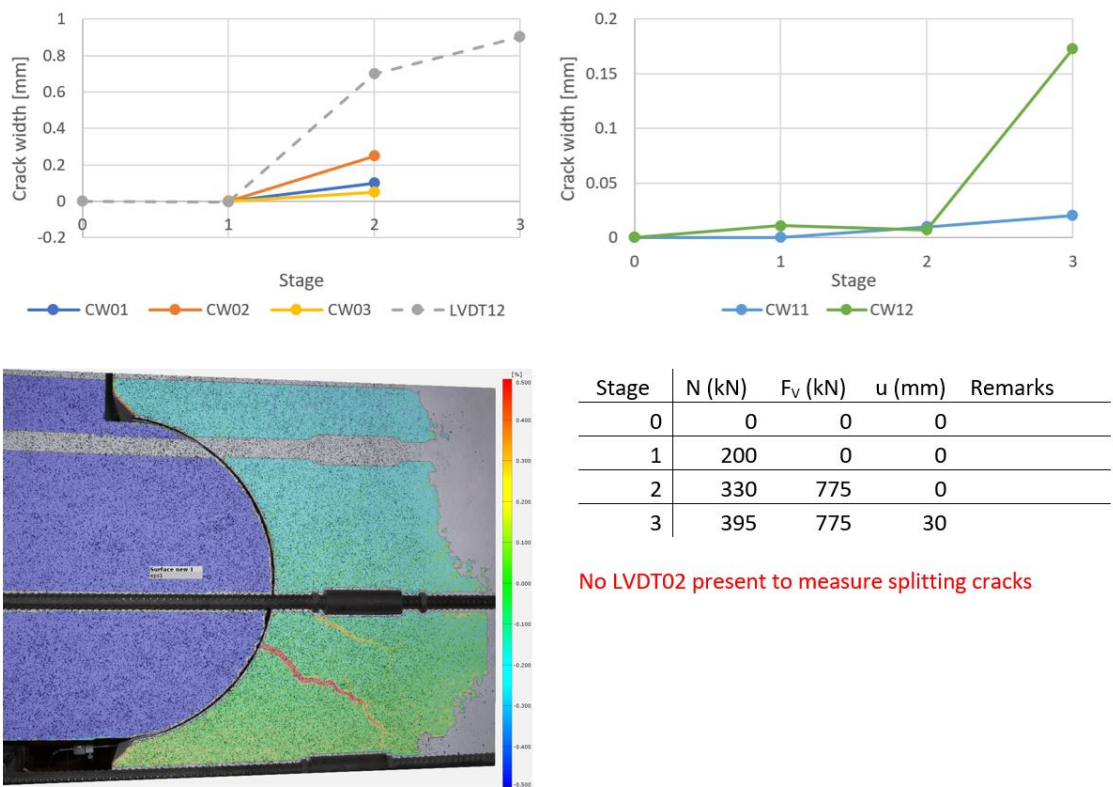


Figure B.4: Crack observations

Test 3a - dominant normal force

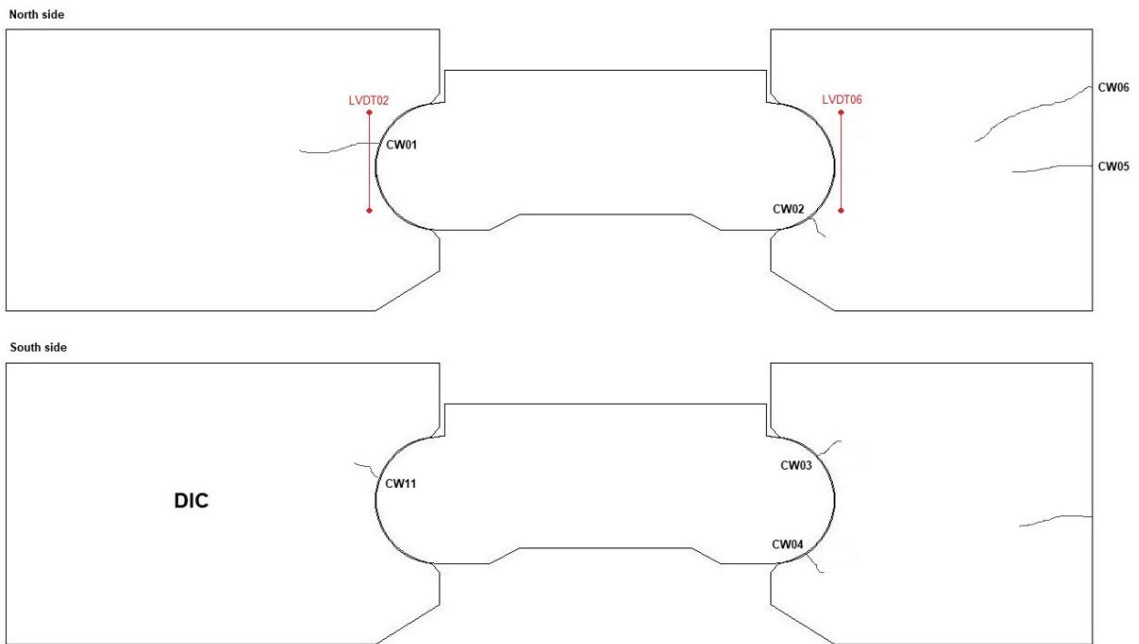


Figure B.5: Crack overview

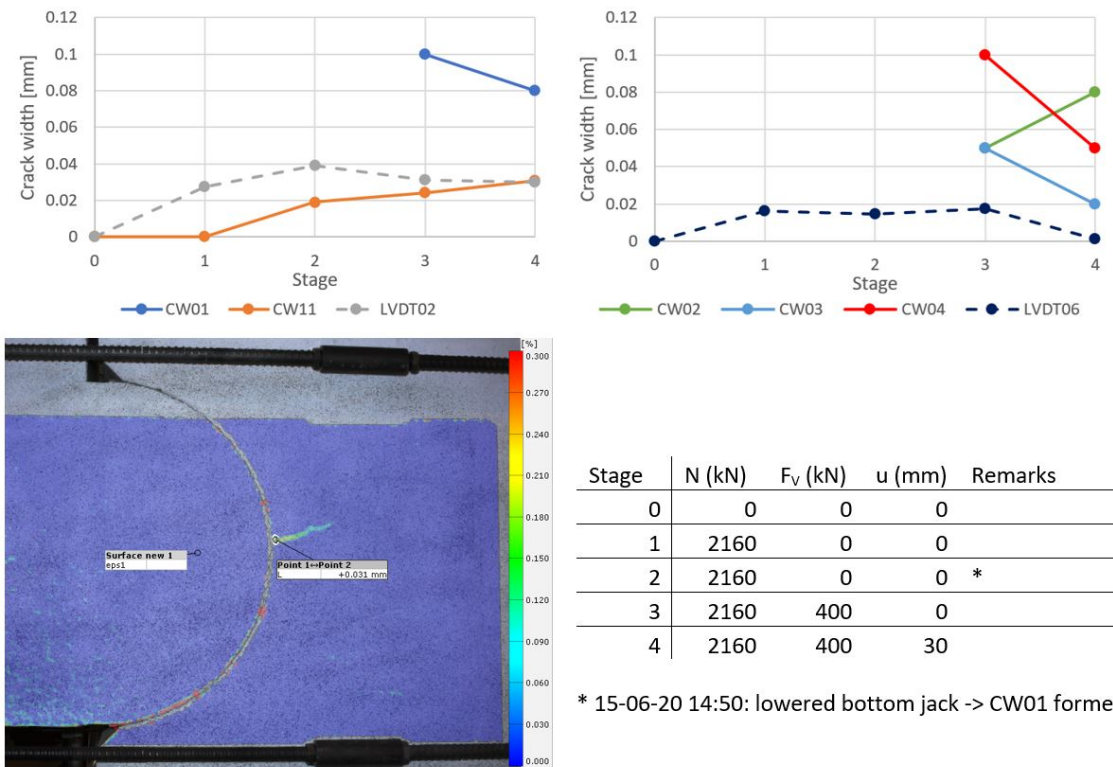


Figure B.6: Crack observations

Test 3b - dominant shear force

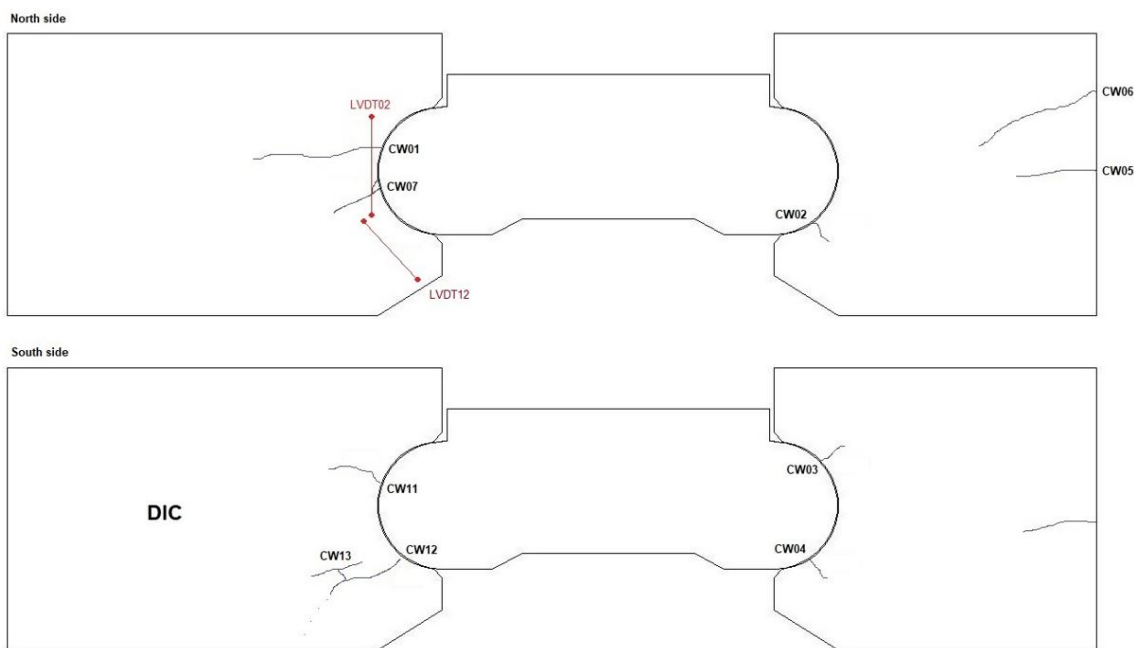


Figure B.7: Crack overview

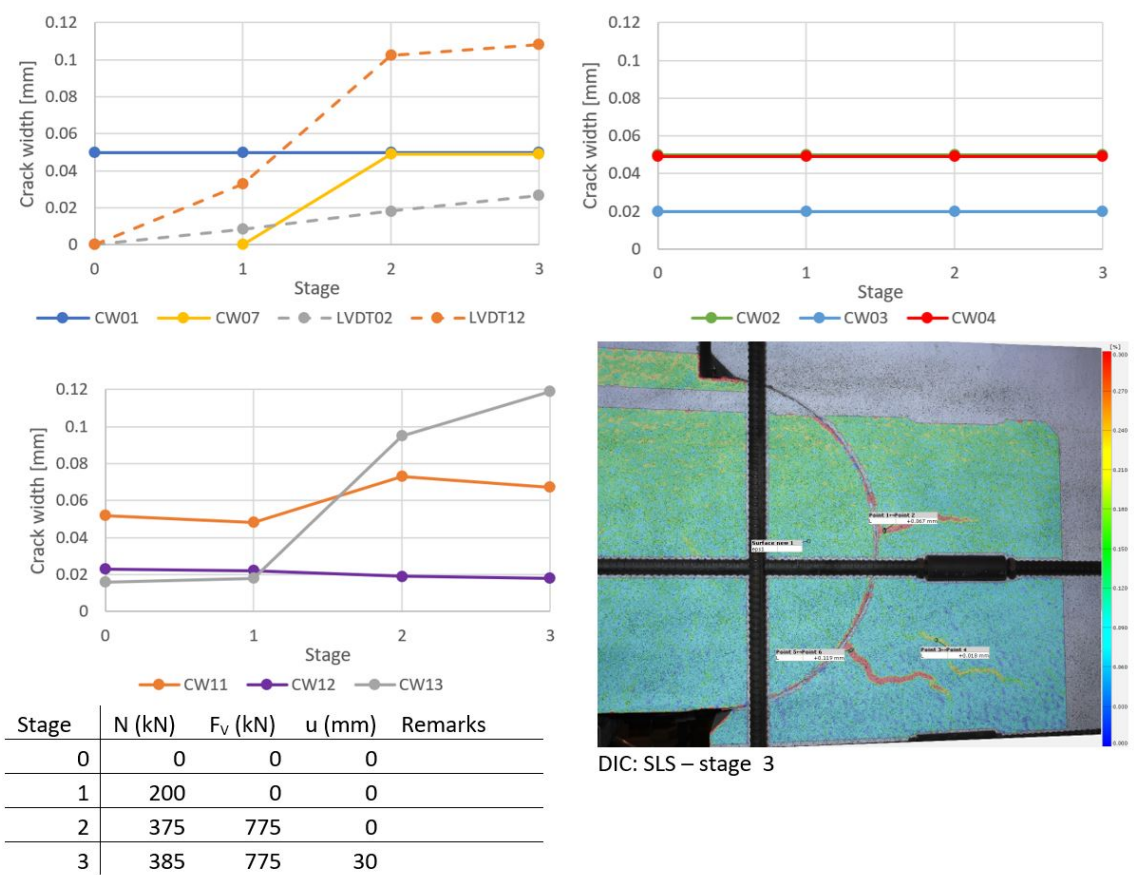


Figure B.8: Crack observations

Test 4a - dominant normal force

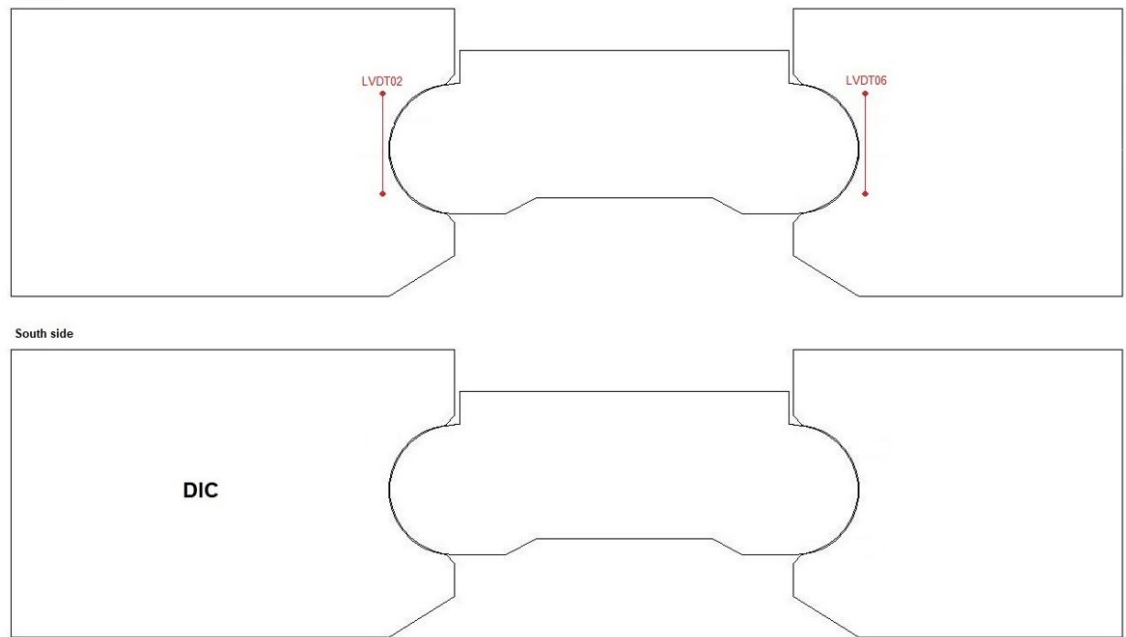


Figure B.9: Crack overview

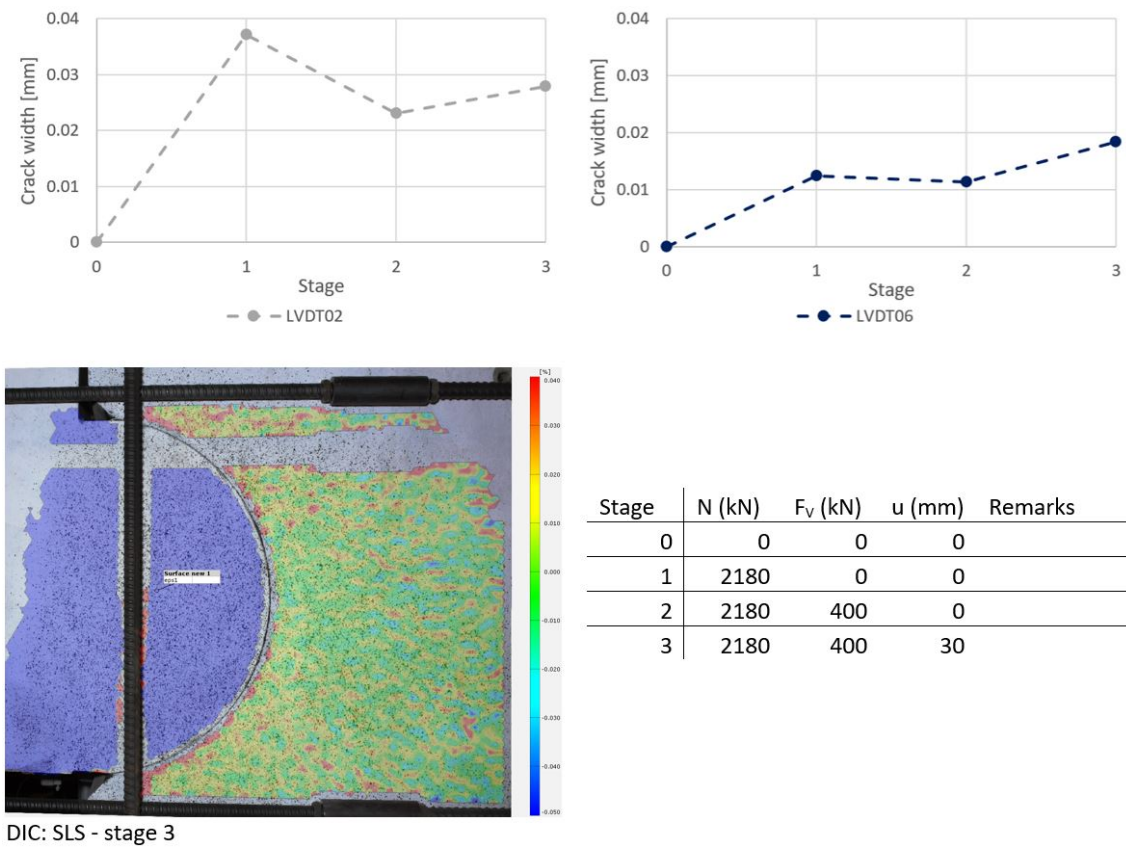


Figure B.10: Crack observations

Test 4b - dominant shear force

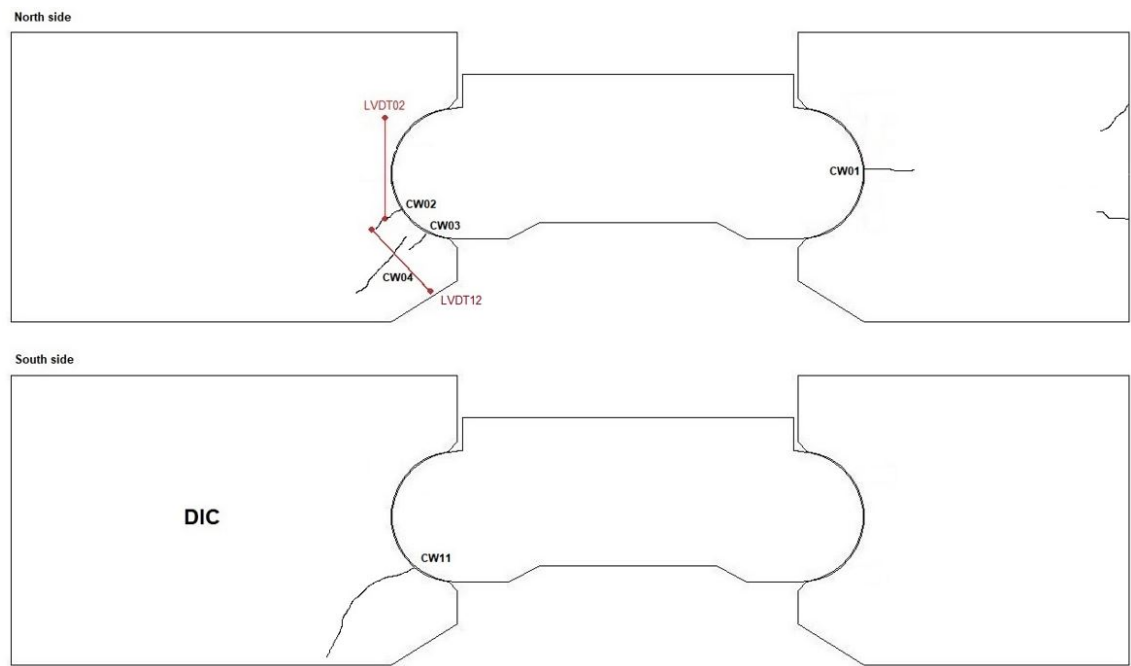


Figure B.11: Crack overview

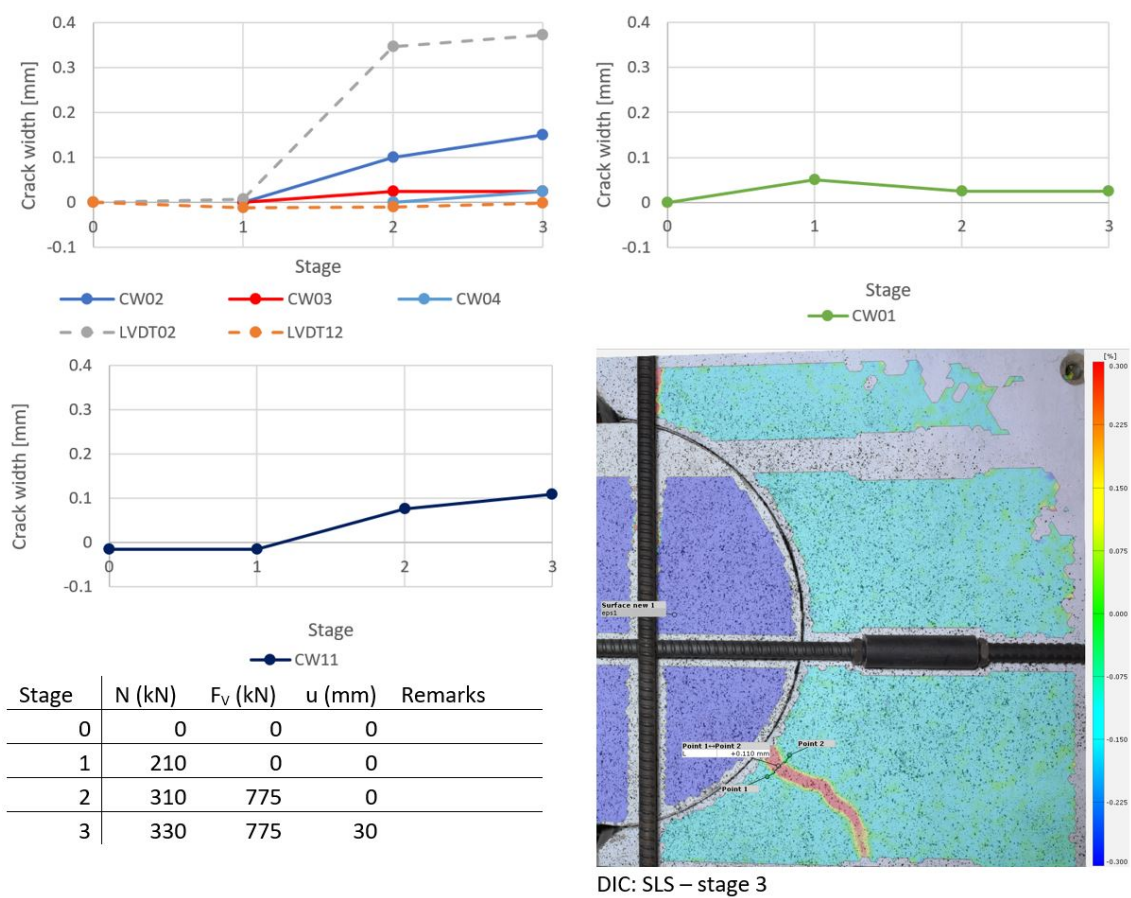


Figure B.12: Crack observations

Test 5a - dominant normal force

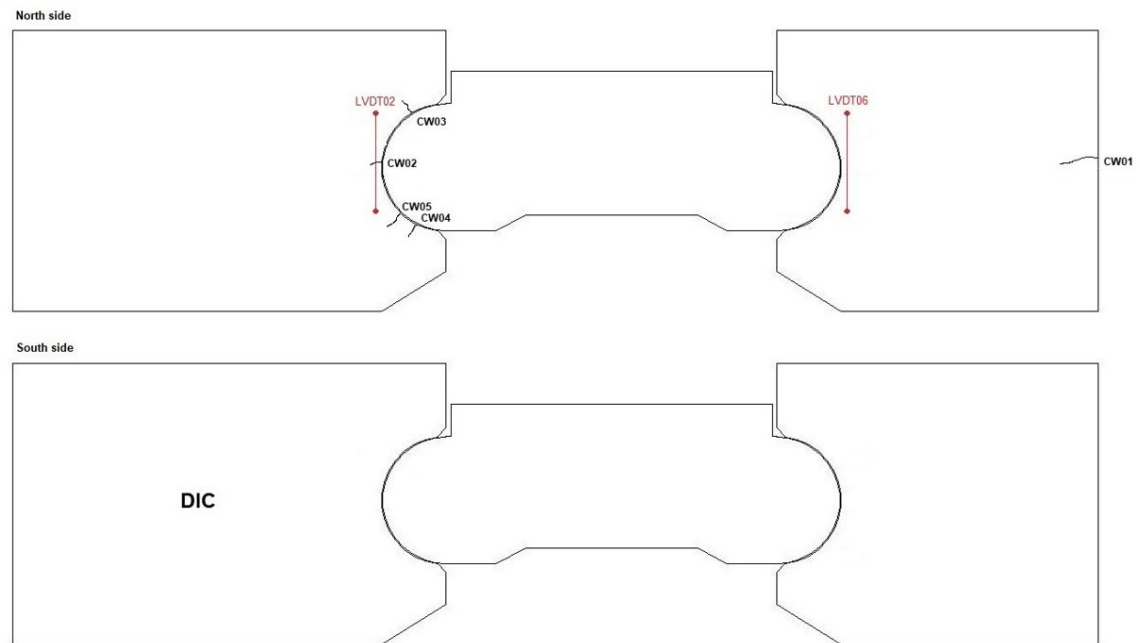
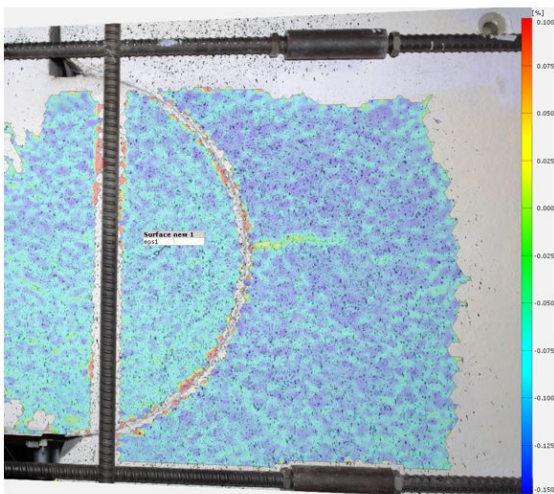
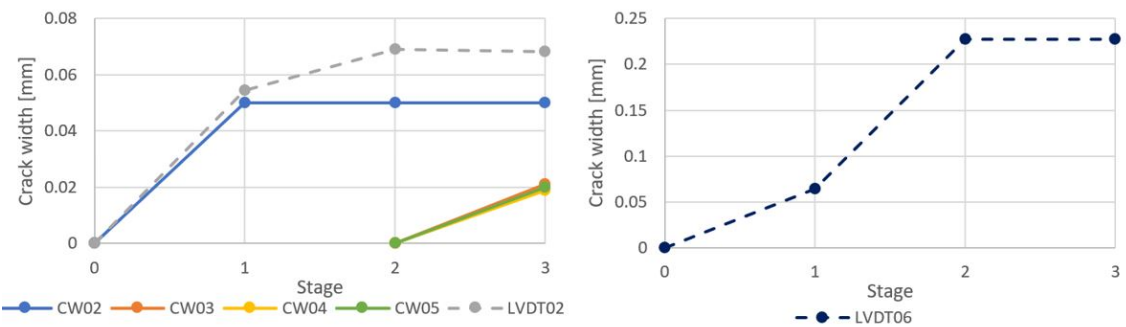


Figure B.13: Crack overview



DIC: SLS - stage 3

Stage	N (kN)	F _v (kN)	u (mm)	Remarks
0	0	0	0	
1	2330	0	0	
2	2200	400	0	*
3	2170	400	30	

* Increase of LVDT06 over weekend without noticeable crack

Figure B.14: Crack observations

Test 5b - dominant shear force

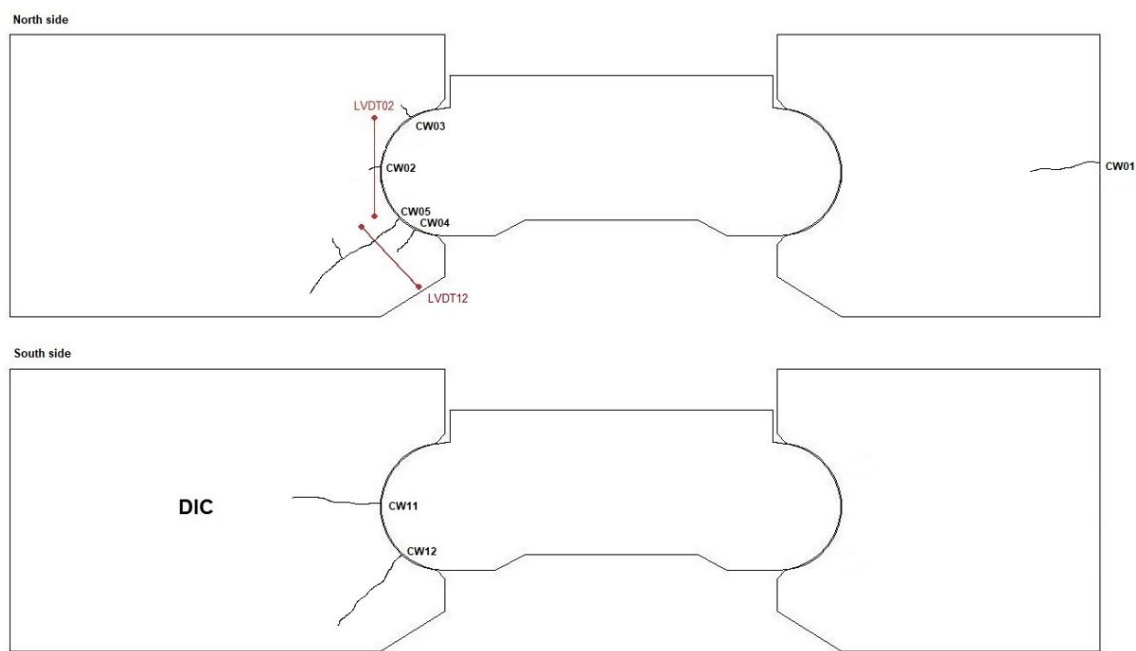


Figure B.15: Crack overview

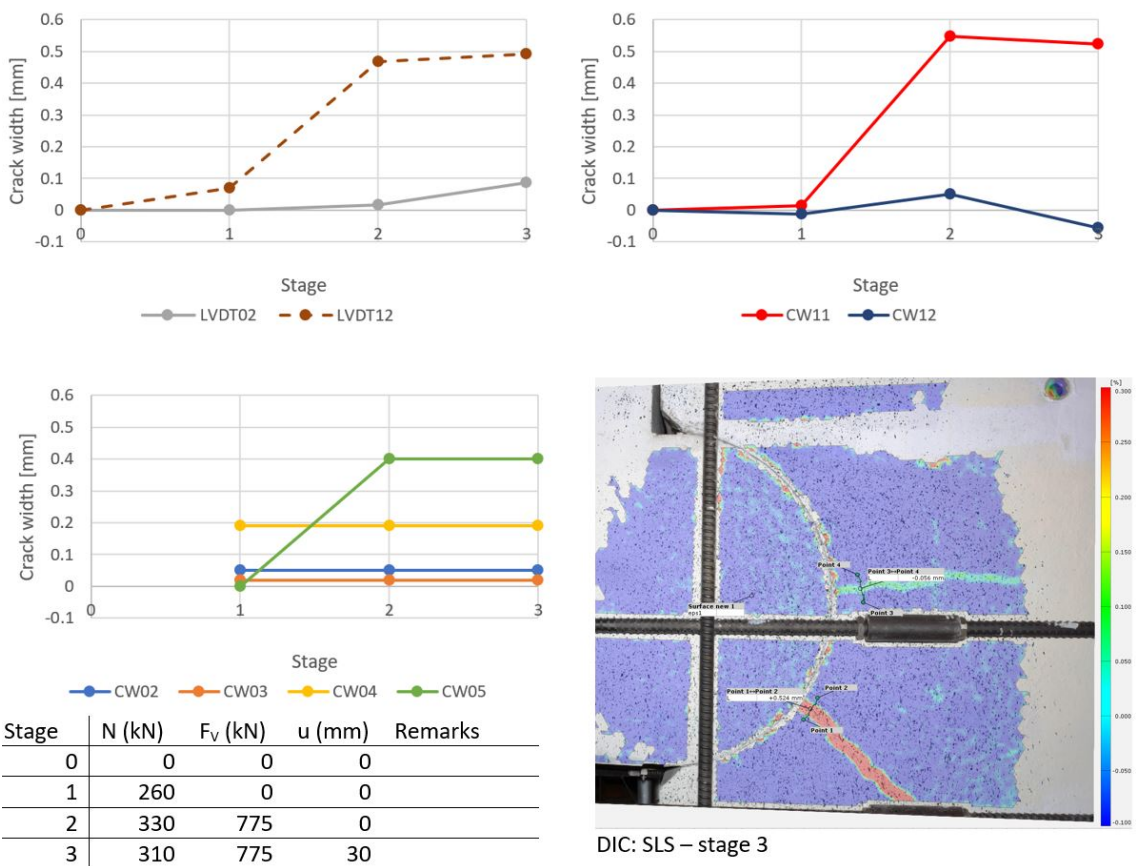


Figure B.16: Crack observations

Delft
University of
Technology

Delft, Building 23
2628 CN, Stevinweg 1

www.tudelft.nl/en/ceg/about-faculty/departments/engineering-structures/sections-labs/concrete-structures/